Optimization of 3T MRI Image Acquisition for Stereotactic Radiosurgery Treatment Planning

Bernardo Maria Bastos Rebelo Sarmento Campilho

Masters in Medical Physics

Department of Physics and Astronomy

2022/2023

Orientador

Prof. Dra. Sofia Silva, Instituto Português de Oncologia de Coimbra F.G., E.P.E.

Coorientador

Prof. Dr. João Santos, Faculdade de Ciências da Universidade do Porto


U.PORTO
FACULDADE DE CIÊNCIAS
UNIVERSIDADE DO PORTO

"Não sou nada. Nunca serei nada. Não posso querer ser nada. Àparte isso, tenho em mim todos os sonhos do mundo.
I am nothing. I will never be anything. I cannot want to be anything. Apart from that, I have in me all the dreams of the world. "

Fernando Pessoa, writing as *Álvaro de Campos* (1928 original version and translation)

Acknowledgements

I feel grateful to many people who have, directly or indirectly, contributed to the existence of this dissertation. I will try to mention as many as possible within this page.

Firstly, I want to express my boundless gratitude to Dra. Sofia Silva, Dr. João Santos and Dra. Sara Pinto, whose constant help, sympathy and patience made this work possible, and who always found the time to answer my tsunami of questions and updates. I am also grateful for the detailed feedback I was given throughout the whole process.

Next, I would like to thank Dr. Bruno Mendes for kindly providing the code that served as the blueprint for the software detection, and the FCUP workshop staff for turning our phantom design into reality. I would like to extend my sincere gratitude to Radiology technicians Joel Sousa and Emanuel Machado, as well as Radiotherapy technician Pedro Conde, for their invaluable assistance in obtaining the MRI and CT images. Special thanks to Dr. Joana Lencart for her contribution in registering the MRI of the geometric phantom with the CT.

I also want to thank my friends for, well, being my friends. João Araújo, João Silva and Rodrigo Pereira, who have named me in their own dissertations and hence I feel the urgent need to name as well. You have made many Mondays bearable, especially in weeks where every day felt like Monday. I also want to thank my high school friend group, some of whom I have known for over 10 years. Seriously, I may never have said this out loud, but I feel lucky to have had you alongside me, and do my utmost to be worthy of your friendship. Finally, Catarina and Rita, my study colleagues during the Masters, thank you for having had the patience to answer my endless questions during exam seasons!

And this may be unusual, but I have to acknowledge the boy I used to be, so hopeful and full of dreams, who loved to speak about dinosaurs and far-away galaxies. After all, he is the reason I keep running.

Last, but definitely not least, I want to thank my family for believing in me even when I did not. My mother, who did so much to allow me to be here. My father, whose help was essential. To my sister, thank you for being my rock during stormy times. And a huge thank you to my great-aunt, who is the purest person I have ever known. I hope I can grow to have 1% of your kindness, Tivovó.

UNIVERSIDADE DO PORTO

Abstract

Faculty of Sciences of the University of Porto
Department of Physics and Astronomy

MSc. Medical Physics

Optimization of 3T MRI Image Acquisition for Stereotactic Radiosurgery Treatment Planning

by Bernardo CAMPILHO

Magnetic Resonance Imaging (MRI) provides a higher soft-tissue contrast than Computed Tomography (CT), which has led to an increased interest in the use of MRI in radiotherapy. However, the presence of geometric distortions in MRI is still a significant limitation of this imaging modality, particularly when strict accuracy requirements are present, such as in Stereotactic Radiosurgery (SRS) treatment planning, whose distortion threshold is 1 mm. Geometric distortion may be system or patient-dependent and has multiple causes, such as magnetic field inhomogeneity or gradient nonlinearity.

Furthermore, the recent direction of MRI imaging is to use higher magnetic field strength scanners, with 3 T scanners rising in clinical use due to their higher signal-to-noise (SNR) ratio and faster imaging times. On the other hand, higher field strengths also imply higher distortion values. The Porto branch of the Portuguese Institute of Oncology (IPO-Porto) routinely uses a 3 T GE Signa MRI scanner for SRS treatment planning for brain tumours and metastases. Thus, it is essential to optimize the MRI sequence parameters, as well as quantify the distortion values in the scanner's field of view (FOV).

In this work, a customized geometric grid phantom was designed and built to quantify the geometric distortion in the scanner and to test different parameters and optimization techniques of the SRS sequence. An anthropomorphic phantom was used to determine the optimal geometric phantom filling, and a gadolinium-based solution was chosen.

Moreover, to quantify the distortion, SNR and contrast-to-noise ratio (CNR) of each sequence, a software was developed to automatically detect and match the phantom inserts in MRI and CT scans, for the corresponding slices. The comparison of their coordinates

after co-registration allowed the calculation of the distortion value at each detected insert point.

The SRS protocol sequence currently used in the IPO showed the highest average distortion values (1.301 mm), above the desired 1 mm threshold. Changing the phase acquisition direction to anterior-posterior (AP) yielded the best average results (0.725 mm). Weighting factors were defined taking into account other factors important in clinical practice, such as the acquisition time, specific absorption ratio (SAR), signal-to-noise ratio (SNR) and contrast-to-noise ratio (CNR). The AP Phase sequence emerged as a clear improvement over the protocol sequence. It is similar in the acquisition time, SAR, SNR, CNR and detected inserts, while significantly lowering the mean and maximum distortion (by 44.27% and 15.65%, respectively). Increasing the flip angle from 12° to 18° also improved the results. The differences between the average geometric distortion results were deemed statistically significant. Various correlations between different acquisition parameters were also found and analysed, using a significance level of $\alpha = 0.05$. In particular, a positive correlation was found between the echo time (TE) and the mean distortion, with p-value = 0.074, which reinforces the importance of minimizing the TE in order to optimize the resulting geometric distortion.

UNIVERSIDADE DO PORTO

Resumo

Faculty of Sciences of the University of Porto
Department of Physics and Astronomy

Mestrado em Física Médica

Otimização da Aquisição de Imagem MRI para Planeamento de Tratamento por Radiocirurgia Estereotáxica

por Bernardo CAMPILHO

A Ressonância Magnética (RM) proporciona um maior contraste dos tecidos moles do que a Tomografia Computorizada (TC), o que tem levado a um interesse crescente na utilização da RM em radioterapia. No entanto, a presença de distorções geométricas na RM continua a ser uma limitação significativa desta modalidade de imagem, particularmente quando existem requisitos de precisão rigorosos, como no planeamento do tratamento por radiocirurgia estereotáxica (SRS), cujo limiar de distorção é de 1 mm. A distorção geométrica pode ser dependente do sistema ou do doente e tem várias causas, como a não homogeneidade do campo magnético ou a não linearidade do gradiente.

Além disso, a direção recente da imagiologia por RM é a utilização de scanners com maior intensidade de campo magnético, com os scanners de 3 T a aumentarem a sua utilização clínica devido a razão de sinal-ruído (SNR) mais elevada e a tempos de imagiologia mais rápidos. Por outro lado, intensidades de campo mais elevadas implicam também valores de distorção mais elevados. O Instituto Português de Oncologia do Porto (IPO-Porto) utiliza rotineiramente um scanner GE Signa MRI de 3 T para o planeamento do tratamento por SRS de tumores cerebrais e metástases. Assim, é essencial otimizar os parâmetros da sequência de RM, bem como quantificar os valores de distorção no campo de visão do scanner.

Neste trabalho, foi desenhado e construído um fantoma geométrico para quantificar a distorção geométrica no scanner e testar diferentes parâmetros e técnicas de otimização de sequências propostas. Foi utilizado um fantoma antropomórfico para determinar a melhor opção para enchimento do fantoma, tendo sido escolhida uma solução à base de gadolínio.

Além disso, para quantificar a distorção, a SNR e o contraste de cada sequência, foi desenvolvido um software para detetar e fazer corresponder automaticamente as inserções do fantoma em exames de RM e TC, para os cortes correspondentes. A comparação das suas coordenadas após o co-registo permitiu o cálculo do valor da distorção em cada ponto de inserção detetado.

A sequência de protocolo atualmente utilizada no IPO apresentou os valores médios de distorção mais elevados (1.301 mm), acima do limiar de 1 mm desejado. A alteração da direção de aquisição da fase para anterior-posterior (AP) produziu os melhores resultados médios (0.725 mm). Foram definidos factores de ponderação para ter em conta outros factores importantes para a prática clínica, como o tempo de aquisição, razão de absorção específica (SAR), a razão sinal-ruído (SNR) e a razão contraste-ruído (CNR). A sequência de fase AP surgiu como uma clara melhoria em relação à sequência de protocolo. É semelhante em termos de tempo de aquisição, SAR, SNR, CNR e inserções detectadas, ao mesmo tempo que reduz significativamente a distorção média e máxima (em 44.27% e 15.65%, respetivamente). O aumento do flip angle de 12° para 18° também melhorou os resultados. As diferenças entre os resultados médios da distorção geométrica foram consideradas estatisticamente significativas. Foram também encontradas e analisadas várias correlações entre diferentes parâmetros de aquisição, utilizando um nível de significância de $\alpha = 0.05$. Em particular, foi encontrada uma correlação positiva entre o tempo de eco (TE) e a distorção média, com p-value = 0,074, o que reforça a importância de minimizar o TE para otimizar a distorção geométrica resultante.

Contents

List of Figures

Glossary

CA	Contrast Agent
CNR	Contrast-to-Noise Ratio
CSF	Cerebrospinal Fluid
CT	Computed Tomography
CTV	Clinical Tumour Volume
EMA	European Medicines Agency
FID	Free Induction Decay
FLAIR	Fluid Attenuated Inversion Recovery
FSPGR	Fast Spoiled Gradient Echo
FOV	Field Of View
FT	Fourier Transform
GD	Geometric Distortion
GRE	Gradient Echo
GNL	Gradient Non-Linearity
GTV	Gross Tumour Volume
HU	Hounsfield Units
IPO	Portuguese Institute of Oncology
MR	Magnetic Resonance
MRI	Magnetic Resonance Imaging
MRMI	Magnetic Resonance Molecular Imaging
NEMA	National Electrical Manufacturers Association

OAR	Organs At Risk
ppm	Parts per million
PET	Positron Emission Tomography
RF	Radio-Frequency
RT	Radiotherapy
RTTP	Radiation Therapy Treatment Planning
SAR	Specific Absorption Rate
SE	Spin Echo
SNR	Signal-to-noise ratio
SPGR	Spoiled Gradient Echo
SPECT	Single-Photon Emission Computed Tomography
SRS	Stereotactic Radiosurgery
T	Tesla
T_1	Longitudinal relaxation time
T_2	Transverse relaxation time
TE	Echo time
TR	Repetition time

Chapter 1

Contextualization

1.1 Research Objectives

Magnetic Resonance Imaging (MRI) has gained significant attention in radiotherapy due to its superior soft-tissue contrast compared to Computed Tomography (CT). However, the presence of geometric distortions in MRI remains a considerable challenge, particularly in scenarios where stringent accuracy requirements, such as Stereotactic Radiosurgery (SRS) treatment planning, which requires distortion thresholds of no more than 1 mm. Geometric distortion can stem from system or patient-dependent factors and is influenced by various causes, including B_0 field inhomogeneity and gradient nonlinearity. Furthermore, the trend towards higher magnetic field strength scanners, such as 3 T scanners, poses increased distortion concerns. This work focuses on addressing these concerns by optimizing MRI sequence parameters and quantifying distortion values within the field of view (FOV) of a 3 T GE Signa MRI scanner used for SRS treatment planning at the Porto branch of the Portuguese Institute of Oncology (IPO-Porto).

The primary objectives of this research are the following:

1. **Design and construction of a customized geometric phantom**, to accurately assess geometric distortion. Its filling solution should be determined by testing different options on an anthropomorphic phantom.

2. **Development of distortion quantification software**. This tool should automate the detection and matching of phantom inserts between MRI and CT scans. By co-registering the corresponding slices and comparing the coordinates of the inserts, distortion values at each detected point can be accurately calculated.

3. **Optimization of MRI Image Acquisition**: By systematically exploring different acquisition parameters, the aim is to identify the most effective sequence optimization techniques to reduce geometric distortion in the MRI scans. This optimization process should take into account crucial factors, such as acquisition time, specific absorption ratio (SAR), signal-to-noise ratio (SNR), and contrast-to-noise ratio (CNR), while maintaining distortion levels within acceptable clinical thresholds.

1.2 Overall Thesis Structure

In Chapter 2, an introduction to the theme of the thesis is presented. It covers the fundamental concepts of Magnetic Resonance Imaging (MRI) and explores its physical principles, including nuclear magnetic moments, signal detection, contrast agents, pulse sequences, scanner components, artifacts, geometric distortion, and image registration.

Next, in Chapter 3, the state of the art in MRI is discussed. This chapter examines various aspects, such as contrast agents used in MRI, methods employed to address the limitations of 3T MRI, advantages and disadvantages of the FSPGR technique, the GE Signa Scanner, phantoms used to measure distortion, and distortion correction methods.

In Chapter 4, the materials and methods utilized in the research are described. This chapter outlines the design of a new phantom specifically created to measure distortion, the tests conducted using different phantom filling solutions, the algorithm developed for automatic distortion calculation, and the optimization of 3T MRI for SRS treatment planning.

In Chapter 5, the results and their analysis are presented. It covers the findings obtained from the phantom filling tests, evaluation of the distortion calculation algorithm, and optimization of 3T MRI for SRS treatment planning.

Chapter 6 serves as the conclusion of the thesis. It summarizes the main findings and contributions of the research, explores the implications of the findings, suggests potential areas for future research, and acknowledges any limitations or challenges encountered throughout the study.

Chapter 2

Introduction

The primary goal of this Chapter is to present an overview of the theoretical background concepts that are most relevant to this thesis.

2.1 Overview of Magnetic Resonance Imaging

Magnetic Resonance Imaging (MRI) is a non-invasive medical imaging technique that uses a combination of a strong magnetic field, radio waves, and computer processing to produce detailed images of internal structures of the body. Unlike X-ray and computed tomography (CT) scans, MRI does not use ionizing radiation.

Throughout this Section, the principles behind the MRI technique are presented. However, a simplified overview is provided here. MRI is a radiological imaging technique that uses nuclear magnetic resonance (NMR). The term ”magnetic” refers to the application of various magnetic fields, whereas ”resonance” refers to the requirement to match the (radio)frequency of an oscillating magnetic field with the precessional frequency of the spin of some nucleus (hence the ”nuclear”) in a tissue molecule. The process commences with the patient being positioned upon a sliding table that enters a large cylindrical apparatus - the scanner - which houses a powerful magnetic field. The magnetic field orients the hydrogen atoms present in the body, followed by the application of radio waves that induce a departure from their natural alignment. As the atoms return to their initial orientation, a signal is produced, which the scanner detects and uses to form an image of the internal structures.

MRI is a very useful tool in contemporary diagnostic medicine. It is capable of producing detailed images of internal structures such as brain, spine, blood vessels, and other

tissues or organs. Notably, MRI proves to be especially useful in imaging soft tissues like muscles and the brain, which are difficult to visualize on radiographs or CT scans. Furthermore, MRI possesses an added advantage - functional imaging - in which metabolic and brain activity in organs and tissues may be observed [1].

MRI provides a higher soft-tissue contrast than CT, which has led to an increased interest in the use of MRI in radiotherapy (RT) [e.g., 2, 3]. MRI is commonly used in RT to identify the tumour and/or organ at risk (OAR) volumes, which are subsequently registered to CT for dose calculation [4]. Recently, promising results have arrived from studies on synthetic CT [5], which is the synthetic calculation of CT images from one or more magnetic resonance (MR) sequences. If it proves to be, indeed, a feasible option, it could eliminate the requirement for an additional planning CT and hence any uncertainties with MR-CT registration.

In numerous papers, the necessity of MR data for radiation procedures has been discussed. There have been reports of modified tumour volume definitions using MR data in comparison to CT for lesions in the brain, head, and neck [e.g., 6, 7], as well as the prostate [8]. At additional tumour sites, discrepancies between MR and CT have also been described [9]. Although many kinds of tumours can be distinguished from surrounding normal tissue using the intrinsic properties of magnetic resonance imaging, the potential for employing MR information in the treatment design is still not extensively explored. There are two main causes for this fact: first, it is well known that MR images have geometric distortions (GD); second, the lack of effective methods to convert the MR image signal into tissue-specific electron density information [10]. Such tissue information is necessary to determine the tissue's absorbed dose distribution after being exposed to photons or charged particles (calibrated from CT Hounsfield units in CT-based planning).

The need for effective methods to include MR image data in radiotherapy treatment planning is unquestionably rising [11]. However, the aforementioned presence of geometric distortions in MRI is one of the main deterrents to its widespread incorporation. Therefore, many strategies have been proposed to minimize its effect, even if it can't be completely eliminated. Geometric distortions in MRI can be divided into two categories: system-related distortions, which are caused by hardware performance, and object-related distortions, which are caused by the magnetic properties of the object being imaged. These two types of distortion have different effects depending on the magnetic field strength and specific imaging protocol parameters, in addition to hardware

performance [10]. In Section 2.7, both system related and object-induced distortions are discussed, as well as the effect that parameters such as the magnetic field strength have on them. As for the different distortion correction techniques proposed throughout the years, they are presented and discussed in Section 3.5.

Finally, it is worth noting that MRI uses radiofrequency (RF) waves rather than ionizing radiation, which means that it does not have the associated risks. Ionising radiation, such as gamma or ultraviolet radiation, is a form of energy that can remove electrons from atoms or molecules. Although there are no strict energy definitions of electromagnetic spectrum bands, ionising radiation has been historically defined as starting at around 10 eV [12], which corresponds to approximately 2418 THz, compared to the 20 kHz-300 GHz interval of RF radiation [13].

2.2 Physical Principles of MRI

The basis of MRI is the interaction of a nuclear spin with an external magnetic field, B_0. The proton in hydrogen, which is the main nucleus in MRI, interacts with the external field to cause the proton's spin to precess around the field direction [14], originating a bulk magnetization. The capacity to control and detect the bulk magnetization of hydrogen spins is the foundation for MR imaging. Hydrogen spins are the most commonly chosen ones due to their abundance in biological tissue, mainly in water and fat, and also because its nucleus is highly magnetic, having only one proton. Moreover, its binding characteristics with other elements depend on the biological tissue, which is beneficial for medical imaging and tissue differentiation [15].

It is a fundamental fact of nuclei that those with odd atomic weights and/or odd atomic numbers, such as the nucleus of the hydrogen atom, possess an angular momentum $\vec{J}$, commonly referred to as *spin*. While nuclear spin is a quantum mechanical property, it is often represented in classical vector models as a physical rotation similar to a top spinning around its axis. A crucial feature of nuclear spin is its ability to produce a *nuclear magnetism* when subjected to an external magnetic field, making it a key feature in MRI. In the following subsection, we will delve deeper into the physical foundation of MRI, which is based on this magnetism.

2.2.1 Nuclear Magnetic Moments

Nucleons, the particles that make up atomic nuclei, originate nuclear magnetic moments, which are the basis of MRI. Normally, as an atom's nuclear layers are filled, each pair of particles is aligned antiparallel to one another. Thus, the magnetic moment of each nucleon is nullified, resulting in atoms that have no bulk magnetic properties [15, 16]. However, when an atom has an odd mass number, such as in a ^{1}H atom, its magnetic moment differs from zero, giving the atom its spin or magnetic moment [17, 18].

When the spin of an atom is not zero, the atom behaves as a tiny magnet that wobbles eternally, a motion referred to as precession. When exposed to an external magnetic field, the atom can align itself either in a parallel or antiparallel direction with the external field, the parallel one being the lower energy state [15]. This allows the two types of alignment to be treated as energy levels instead of physical orientations. Both are stable energy states, and atoms can swap their energy state if excited with energy equal or higher than the difference between the two energy states [19].

In hydrogen nuclei, only two populations of spins with symmetrical precession directions can exist. These spin values are s = $\pm 1/2$, in units of $\hbar$, given the maximum value n/2 (n=1 for hydrogen) and the half-integer nature of the proton spin. More formally, these are solutions of the Schrödinger-Pauli equation, and the magnitude of the spin angular momentum for a spin 1/2 particle is

$$||s|| = \hbar\sqrt{s(s+1)} = \frac{\sqrt{3}}{2}\hbar \tag{2.1}$$

Through the analysis of the hydrogen's spectrum fine structure, it is possible to observe a doublet that corresponds to two potential outcomes for the z-component of the angular momentum, where for any given direction z, $s_z = \pm\frac{1}{2}\hbar$. These spins are quantized due to the quantization of spin angular momentum, which is a quantum property first formally proposed in 1925 by George Uhlenbeck and Samuel Goudsmit [20]. This leads to two energy states (parallel and antiparallel) that have different populations due to the thermal energy present in the system [16, 18]. The number of protons in each state, $N_{parallel}$ and $N_{antiparallel}$, is given by the Boltzmann distribution. The number of excess protons in a parallel state can be written as:

$$N_{excess} = N_{parallel} - N_{antiparallel} = \frac{N_{total}}{2}\frac{\gamma\hbar B_0}{k_B T} \tag{2.2}$$

where γ is a physical constant ($\gamma = \frac{q}{2m}$) known as the *gyromagnetic ratio*, N_{total} is the total number of protons in the considered system, T is the temperature and k_B is the Boltzmann constant. There are more parallel protons, since it is the lowest energy state. For example, in a human body at 37°C and B_0 equal to 1.5T, the difference in the number of protons in both energy states is only four per million of atoms in each energy state. As can be observed in Equation 2.2, this difference increases in higher magnetic fields, and the energy difference between the two states increases with the increase of B_0, which is the reason behind the increase in the intrinsic signal observed at higher magnetic fields [21].

A nonzero spin nucleus produces a magnetic field around it, much like any other spinning charged object. The resulting magnetic moment, also known as the nuclear magnetic dipole moment, is physically represented by the vector quantity $\vec{\mu}$. There is a fundamental equation relating the spin angular momentum and magnetic moment vectors:

$$\vec{\mu} = \gamma \vec{J} \tag{2.3}$$

Assuming, without loss of generality, that the external field B_0 is applied in the z-direction of the laboratory frame, such that $\vec{B_0} = B_0 \vec{k}$, the motion of $\vec{\mu}$ can be described using a classical mechanics analysis of the torque:

$$\frac{d\vec{J}}{dt} = \vec{\mu} \times B_0 \vec{k} \tag{2.4}$$

Which, using Eq. 2.3, is equivalent to

$$\frac{d\vec{\mu}}{dt} = \gamma \vec{\mu} \times B_0 \vec{k} \tag{2.5}$$

The solutions to Eq. 2.5, whose full derivation can be consulted in [22] are:

$$\begin{cases} \mu_{xy}(t) = \mu_{xy}(0) e^{-i\gamma B_0 t} \\ \mu_z(t) = \mu_z(0) \end{cases} . \tag{2.6}$$

The motion of $\vec{\mu}$ described in equation 2.6 is known as *nuclear precession*, which involves precession around the direction of the B_0 field. An important characteristic of nuclear precession is its angular frequency ω_0, also known as the Larmor frequency, which can be expressed as:

$$\omega_0 = \gamma B_0 \tag{2.7}$$

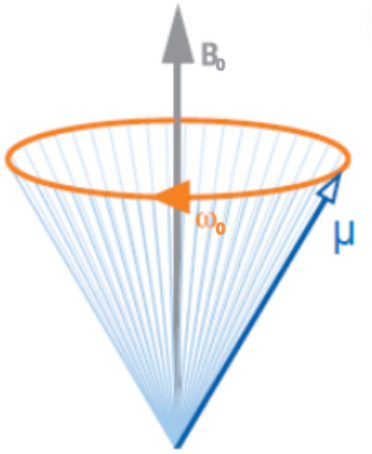

FIGURE 2.1: Nuclear precession of $\vec{\mu}$ around the direction of the magnetic field (adapted from [23]).

To effectively characterize the behaviour of a spin system, it is necessary to introduce a macroscopic magnetization vector $\vec{M}$. This vector reflects the vector sum of all the microscopic magnetic moments existing in the object [22]. If we define $\vec{\mu_n}$ as the magnetic moment of the nth nuclear spin, and N_S as the total number of spins in the imaged object, then $\vec{M}$ can be written as:

$$\vec{M} = \sum_{n=1}^{N_S} \mu_n \tag{2.8}$$

2.2.2 Bloch Equation and Relaxation

The Bloch equation provides a quantitative description of the time-dependent behaviour of $\vec{M}$, in the presence of an applied radiofrequency (RF) pulse magnetic field $\vec{B}_1$(t) and a static magnetic field $\vec{B}_0$, whose sum defines the total magnetic field $\vec{B}$. In the context of MRI, the Bloch equation has the following general form:

$$\frac{d\vec{M}}{dt} = \gamma\vec{M} \times \vec{B} - \frac{M_x\vec{i} + M_y\vec{j}}{T_2} - \frac{(M_z - M_z^0)\vec{k}}{T_1} \tag{2.9}$$

where M_z^0 is the thermal equilibrium value for $\vec{M}$ in the presence of $\vec{B}_0$ alone [22]. T_1 and T_2 are time constants that characterize the relaxation process of a spin system following disturbance from thermal equilibrium, and a brief explanation of their origin and significance is presented later in this Section.

Even if a group of particles has an excess of spin, as is the case for hydrogen atoms, that doesn't necessarily guarantee a detectable signal by itself. In fact, even in a macroscopic body, it's important that the magnetization vector is tipped away from the direction of the external field in order to initiate precession. This is due to the fact that the magnetization must produce a changing magnetic flux ϕ in a nearby coil as it precesses around the external magnetic field [14, 22], thus inducing an electromotive force in the coil (Section 2.2.3), as determined by Faraday's law of induction:

$$emf = -\frac{d\phi}{dt} \tag{2.10}$$

To accomplish this, a radiofrequency magnetic field must be applied for a short period of time (RF pulses). This will rotate the magnetization away from its longitudinal direction along the $\vec{B_0}$ axis. The RF pulse is produced by another nearby coil which can also serve as the receiver coil if its radiofrequency is tuned to the Larmor frequency [21], a condition known as *resonance condition*. This resonance condition in MRI ensures that the precessing spins resonate, meaning they absorb energy and enter into a state of phase coherence, resulting in the precession of the bulk magnetization vector $\vec{M}$ which, as explained before, is necessary for the coils to detect the signal. Therefore, the process of rotating the magnetization away from the $\vec{B_0}$ axis and then synchronizing the precessing spin to the external magnetic field is vital in generating a detectable MRI signal [14].

Now the relaxation constants T_1 and T_2 can be explained. First, we focus on the constant T_1. It represents the "spin-lattice" decay or relaxation of the signal, as a result of the interactions between the spins and their surroundings. The magnetization will tend to grow back in the direction of the static field B_0, previously chosen to be $\vec{z}$, after being rotated into the transverse plane by the RF pulses [14]. This fact may not be obvious upon first inspection of the Eq. 2.9, but it should be noted that the longitudinal term is positive, that is, $M_z \geq 0$. It then tends towards the initial total magnetization value, although it never surpasses it ($M_z/M_0 \leq 1$), as shown in Figure 2.2. This is made clear by writing the solution for the longitudinal magnetization after the end of the $\vec{B_1}$ RF pulse, that is, in the case where $\vec{B} = B_0\hat{z}$ and M_0 is the equilibrium value:

$$M_z(t) = M_z(0)e^{-\frac{t}{T_1}} + M_0(1 - e^{-\frac{t}{T_1}}) \tag{2.11}$$

This longitudinal relaxation time, or T_1, is a time constant that describes the recovery rate of longitudinal magnetization, as a result of the interaction between the spins and the

nearby atoms. This recovery behaviour is shown in Figure 2.2. It should be noted that this recovery process is not exclusively attributable to the decay of transverse magnetization (M_{xy}), which decays more rapidly due to phase loss between spins. Instead, the recovery of longitudinal magnetization is mainly due to the relaxation of individual spins that shift from the transverse plane (x-y) to the longitudinal axis (z) over time.

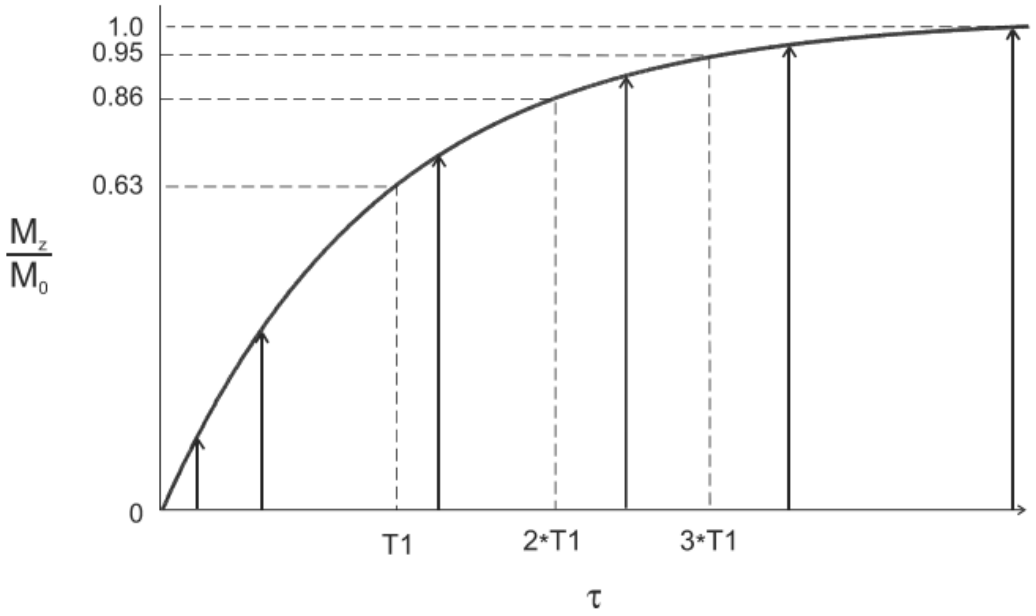

FIGURE 2.2: T_1 relaxation curve [14]. The longitudinal magnetization M_z is null after a 90° RF pulse (point t = 0 in the figure), but it will increase as the protons release their energy through T_1 relaxation. Eventually, the initial value M_0 will be completely restored, as described by Equation 2.11. T_1, the spin-lattice relaxation time, is the time when M_z has recovered to 63% of its initial value in this process.

The constant T_2, however, is connected to a distinct decay mechanism that arises from dephasing between different spins. This dephasing results from local non-uniformities in the magnetic field that stem from variations in the electronic and geometrical configurations of hydrogen atoms bound to different molecules, including water, fat, or proteins. These variations give rise to distinct Larmor frequencies, or chemical shifts, between the atoms. As time elapses, the phase differences caused by these very small frequency variations lead to the dephasing of transverse spins and to the loss of coherence of transverse magnetization, which is also referred as "spin-spin" decay. The decay can be measured by solving Bloch's equation (Eq. 2.9) in the rotating frame, from which we get the following expression for the transverse component:

$$M_{\perp}(t) = M_{\perp}(0_{+})e^{-\frac{t}{T_2}} \tag{2.12}$$

Analysing Eq. 2.9, it can be seen that, since the derivatives of the transversal components of $\vec{M}$ are proportional to themselves, this decay, or relaxation, will also be exponential. However, unlike the longitudinal term, the transverse magnetization will diminish until it returns to a null value, as expressed by Eq. 2.12.

Dephasing due to external field inhomogeneities would generally result in more signal suppression (T_2 would be replaced by a shorter relaxation time $T_2^* < T_2$; see Section 2.2.3), which would result in greater signal loss. However, in Eq. 2.9 it was assumed that this source of dispersion is "rephased" or "echoed," thereby avoiding the need for further suppression [14]. An additional RF pulse can be used to accomplish this; its main idea is to rotate all spins 180 degrees in the transverse plane. The two relaxation constants presented here (T_1 and T_2) are essential to the principle behind how contrast agents work in MRI, which is explored in the next subsection.

2.2.3 MRI Signal Detection

MRI signals are detected by measuring the changing magnetic flux caused by the precessing spins. As the spins precess around the external magnetic field, they produce a changing magnetic flux that induces an electrical current in a nearby coil or antenna (detailed in Section 2.4.3), according to Faraday's Law of Induction (Eq. 2.10). This electrical current is then amplified and processed to produce an image. In practice, this processing stage is mostly automatic and complex, especially if field inhomogeneities are taken into account. Liang & Lauterbur [22] or Kuperman [17], for example, provide comprehensive explanations on image pre-processing and processing stages, which are beyond the scope of this thesis.

The most basic signal detected by RF coils after a pulse excitation is known as *free induction decay* (FID). The term "free" refers to the fact that the signal is produced by the free precession of the bulk magnetization vector about the $\vec{B_0}$ field; "induction" denotes that the signal was produced using Faraday's Law of Electromagnetic Induction; and "decay" implies the characteristic decrease in signal amplitude with time [22]. The FID signal is related to transverse relaxation, which is a process that occurs, in part, simultaneously with longitudinal relaxation, although they are independent processes. Moreover, transverse relaxation (also known as T_2 relaxation) occurs long before the longitudinal relaxation process is complete [24, 25].

The T_2 relaxation process begins immediately after RF excitation, when part of the spins have synchronous precession, in a state called *phase coherence* given that the spins are in phase. However, over time, this phase coherence is lost, in a process called *dephasing*. This loss of coherence is due to two factors: energy transfer between spins as a result of local magnetic field fluctuations (due to thermodynamic stochastic processes) and intrinsic B_0 field inhomogeneities, which can be caused by the system itself or the imaged object, as detailed in Sections 2.6 and 2.7. The latter factor introduces a new decay time T_2^*, which is shorter than T_2 (Figure 2.3) and takes into account the fact that the B_0 field inhomogeneities, whatever their origin, will shorten the transverse relaxation time T_2 [25, 14]. Thus, the FID signal reflects the attenuation of MR signal over time, after RF excitation, due to T_2^* effects.

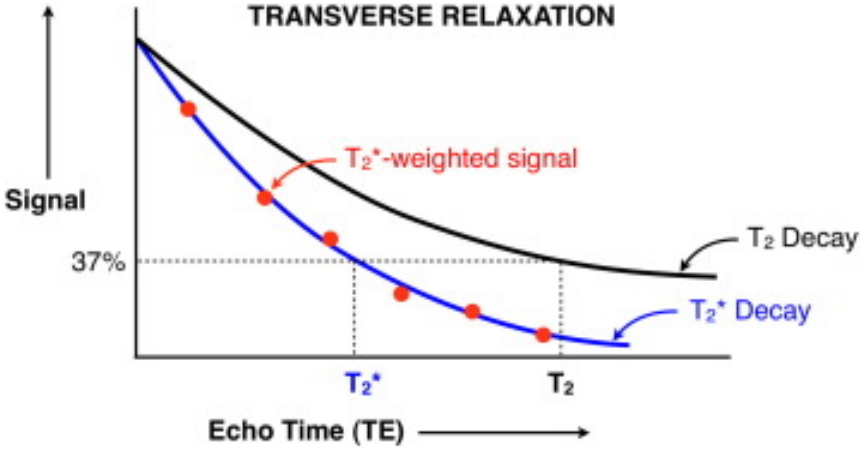

FIGURE 2.3: T_2 and T_2^* decay comparison [26]. The faster decay in the T_2^* curve has to do with loss of coherence introduced by B_0 field inhomogeneities.

2.2.4 Contrast Agents in MRI

The use of contrast agents in MRI can increase the visibility of certain structures or tissues within the body. They work by changing the longitudinal relaxation time (T_1) and/or transverse relaxation time (T_2) of the observed tissues, or by changing their proton density [25]. Even though MRI has a considerable amount of intrinsic contrast between tissues, pathological tissue may or may not have significant differences in T_1 or T_2 from the surrounding normal tissue. This can result in little signal difference between normal and pathological tissue, making it difficult to detect abnormalities [14, 27]. By administering a contrast agent, the signal difference can be increased and the diagnosis can be improved.

There are two types of contrast agents utilized in MRI: paramagnetic and superparamagnetic. Paramagnetic contrast agents are characterized by unpaired electrons, whose permanent magnetic moment is associated with a local magnetic field [14]. The inclusion of a small quantity of paramagnetic contrast agents can significantly reduce the relaxation times of water-rich materials [22]. Superparamagnetic contrast agents comprise small particles of iron oxide that generate a local magnetic field that enhances the main magnetic field, thereby increasing image contrast.

The most commonly used paramagnetic contrast agent in MRI is Gadolinium, which is administered intravenously. The lanthanide Gd^{3+} has seven unpaired electrons, and works by shortening the T_1 and T_2 of water protons in the targeted tissue [27, 28]. This results in an increase in signal intensity on T_1-weighted images, making the tissue appear brighter. Gadolinium can enhance the visibility of blood vessels, tumours, and inflammation. Superparamagnetic contrast agents, such as iron oxide particles, are used to enhance the visibility of blood vessels, hemorrhages and calcifications [29], by shortening the T_2 of the protons in the targeted tissue. This results in a decrease in signal intensity on T_2-weighted images, making the tissue appear darker.

Contrast agents can enhance diagnostic accuracy in certain conditions, such as cancer, inflammation, and vascular diseases. Nevertheless, they can also lead to adverse reactions, such as allergic reactions and kidney problems. Therefore, the use of contrast agents is cautiously evaluated and considered on a case-by-case basis. A more detailed exposition of some of the most commonly employed contrast agents, along with the tests performed to study their impact on geometric distortion, is provided in Sections 4.1 and 4.1.1, respectively.

The development of new and improved CA has been an active area of research in MRI, with the goal of increasing the specificity and sensitivity of the imaging methods [30, 31]. In this field, the current state of the art can be broadly classified into two categories: blood pool agents and targeted molecular agents. The former, exemplified by gadolinium chelates, are the most commonly employed contrast agents in MRI. These agents work via their accumulation in blood vessels and tissues, thereby reducing the T_1 relaxation time of their protons, which translates into an increase in the signal intensity. These agents have a larger size that prevents easy passage out of capillaries, resulting in longer vascular retention times [32].

Recently, according to the European Medicines Agency (EMA), certain gadolinium

contrast agents used in MRI body scans have an unfavourable benefit-risk ratio and are no longer recommended for use, with the authorizations of some suspended. The affected agents include intravenous drugs containing gadobenic acid (except for liver imaging), gadodiamide, gadopentetic acid, and gadoversetamide. The EMA's review of gadolinium contrast agents has confirmed the need to restrict the use of certain linear gadolinium agents, aligning with their previous recommendations. Hence, in 2018, these recommendations were implemented in Portugal [33]. Gadolinium CA, such as the macrocyclic agents gadoteridol, gadobutrol and gadoteric acid are still allowed and commonly used intravenously in patients, as they are more stable and less likely to release gadolinium in tissues, thereby preventing dangerous levels of accumulation.

Nanoparticle CA are a particularly promising new area of research in the field of contrast agents in MRI. These targeted molecular agents are designed to target specific tissues or pathologies and provide a more specific enhancement. Other biomedical applications for magnetic nanoparticles, such as magneto-mechanically induced cellular damage, as well as cell manipulation and separation, have been successfully demonstrated [31].

These nanoparticle CA can be conjugated to a variety of targeting molecules, such as antibodies or peptides, to increase specificity. Examples of targeted molecular agents include iron oxide nanoparticles, gold nanoparticles, and superparamagnetic iron oxide particles. The potential of these CA for brain metastases detection is still undetermined, but recent phase I and II trials using theranostic nanoparticles have shown promising results in terms of contrast improvement and therapeutic outcome [34, 35].

For brain imaging, gadolinium-based CA are the most commonly used, particularly in radiosurgery. Manganese has been suggested as an alternative recently, but its efficacy is still being studied [36, 37]. Superparamagnetic iron oxide nanoparticles have advantages in more specific imaging contexts, such as atherosclerosis or inflammation imaging. While recent studies such as Chen et al. [38] propose the use of these nanoparticles for tumour imaging, they also acknowledge that there are still some significant challenges to overcome before its clinical implementation, such as the lack of rigorous biosafety protocols.

Contrast agents play a crucial role in MRI, and the development of new and improved CA is an active area of research. The pursuit of researchers in this field has been directed by two fundamental objectives: enhancing the contrast agent's potency (increasing its

relaxivity) and ensuring greater patient well-being (minimizing toxicity) [32]. The continued development of CA in MRI is expected to provide new insights into various diseases and pathologies and improve the clinical utility of MRI. In Section 4.1.1, the CA chosen for geometric distortion impact studies and the final choice for the phantom filling are explained.

2.3 Pulse Sequences

Pulse sequences in MRI are a set of instructions that dictate the specific order and timing of RF pulses and magnetic field gradients applied to the patient during the imaging process. These pulse sequences are designed to manipulate the behavior of hydrogen nuclei (protons) in the body in order to generate images with specific contrast and information. Pulse sequences can be classified based on the contrast mechanism used, with the most common being T_1-weighted, T_2-weighted, and proton density-weighted.

Before differentiating these types of pulse sequences, there are two important pulse sequence parameters, mentioned in the last Section, that must be defined: the repetition time (TR) and the echo time (TE). TR specifies the time delay between successive excitations of the same slice, while TE refers to the time interval between the application of the excitation pulse and the acquisition of the MR signal [25]. These two parameters are inherently linked to the contrast and resolution of the MR images, as will be explained in this Section.

T_1-weighted sequences in MRI are designed to produce images with high contrast between tissues based on differences in their T_1 relaxation times, and typically involve the use of specialized pulse sequences that manipulate the relaxation times of protons in different tissues using specific RF pulses, gradients, and delays. The selection and optimization of these parameters are critical to achieve the desired image contrast, and may involve the use of Spin Echo (SE) or Gradient Echo (GRE) sequences, depending on the specific application and imaging goals. SE sequences involve a 180-degree refocusing pulse to reverse the dephasing of proton spins, producing an echo that provides valuable anatomical information, while GRE sequences use variations in the magnetic field gradients to create an echo signal (Section 2.3.1). T_1-weighted sequences are often employed to image tissues with higher water content, such as blood and tumours, which have shorter T_1 relaxation times [22]. In Section 2.3.1, T_1-weighted images will be analysed in the particular context of gradient echo sequences.

Alternatively, T_2-weighted imaging utilizes a series of RF pulses to create images with heightened contrast between materials that exhibit distinct T_2 relaxation times. Such sequences are usually employed to visualize substances with limited water content such as fat or fluid-filled structures with longer T_2 relaxation intervals. The degree of T_2 weighting can be controlled by TE selection. If a short TE (< 30 ms) is used, there will be a low degree of T_2 weighting, while longer echo times (> 60 ms) are associated with strongly T_2-weighted images [25].

Lastly, proton density-weighted imaging focuses on creating images that exhibit a marked contrast between materials with different proton densities. This type of imaging is obtained using a single RF pulse without any intervals, and is commonly utilized to visualize bones, tendons, ligaments, and cartilages.

Indeed, the selection of pulse sequences in MRI is a crucial component in generating images with particular contrast and information. Specialized pulse sequences such as Fluid Attenuated Inversion Recovery (FLAIR), Saturation-Recovery and Inversion-Recovery are available to produce images with specific contrasts or provide additional information. The choice of pulse sequences also depends on the specific imaging application and the desired balance between image quality and contrast.

At the Portuguese Institute of Oncology of Porto (IPO-Porto), where the present work was conducted, the selected pulse sequence for stereotactic radiosurgery (SRS) treatment planning (Section 2.8) is the Fast Spoiled Gradient Echo (FSPGR) sequence. Therefore, the next Section is dedicated to explaining this pulse sequence and justifying its general use.

2.3.1 T_1-weighted images using a Gradient Echo Sequence

Normal tissue T_1 values differ significantly from each other, making T_1-weighted contrast an effective technique for between different tissues. Typical T_1 values for different body parts, at 3 T, are presented in Table 2.1. Gradient echo sequences are used to generate T_1-weighted images because they can produce images with high T_1 contrast in relatively short scan times. MRI scanners have gradient systems, which are necessary to encode spatial information into the signal (Section 2.4.2). This gradient system allows the use of GRE sequences, whose working mechanism will now be explained.

In GRE sequences, after the emission of the first FID, the polarity of the gradient magnetic field G(t) is reversed. This allows for the refocusing of the spins and, consequently, the emission of a second (echo) signal. Figure 2.4 shows a possible GRE pulse sequence,

TABLE 2.1: Typical T_1 values of different body parts at 3 T, for 3D SPGR sequences.

Body Part	**T1 Value (ms)**	**Reference**
Brain - gray matter	1380 ± 59	Preibisch and Deichmann [39]
Brain - white matter	933 ± 15	Preibisch and Deichmann [39]
Myocardium	1341 ± 42	Clique et al. [40]
Prostate	1530 ± 498	Fennessy et al. [41]
Spine (cervical)	1848 ± 143	Samson et al. [42]
Muscle	1100 ± 59	Chen et al. [43]

along with the phase evolution of the spins in the imaged object. In this example, the z and y-direction gradients are used for slice and phase encoding, respectively, and the x-gradient is used for frequency encoding and for the formation of the gradient echo via its bi-phasic inversion.

The pulse sequence is repeated M times with different phase-encoding gradient values. The overall scan time (T_{scan}) is determined by M x TR, where TR is the time interval between consecutive excitations. GRE sequences offer much faster imaging compared to other sequences, as TR is a major determinant of scan time. Therefore, they are less frequently affected by motion artifacts and are preferred whenever a short scan time is desirable [17, 29].

However, a short TR may have its drawbacks. The time available for T_1 relaxation is also short, which can cause saturation and reduced signal-to-noise ratio (SNR) when a large flip angle (Section 2.9) is used. The maximum signal occurs when the initial and reversed gradients are balanced, with equal amplitude and duration. GRE sequences are susceptible to B_0 inhomogeneity and may have decreased performance in low-field applications [25]. Nonetheless, GRE sequences are widely employed in various MRI applications, such as brain imaging, due to their unique advantages.

In order to achieve the desired T_1 weighting in GRE sequence images, the effects of T_2^* must be minimized. For example, using the gradient echo technique with a very short TE can reduce T_2^* (or T_2) contrast. Therefore, it is possible to achieve high-quality T_1-weighted images by carefully selecting the repetition time and minimizing T_2^* effects [14, 17].

2.3.2 Fast Spoiled Gradient Echo (FSPGR)

The FSPGR pulse sequence is a T_1-weighted MRI sequence that is commonly employed for high-resolution anatomic imaging. This sequence offers several advantages that make

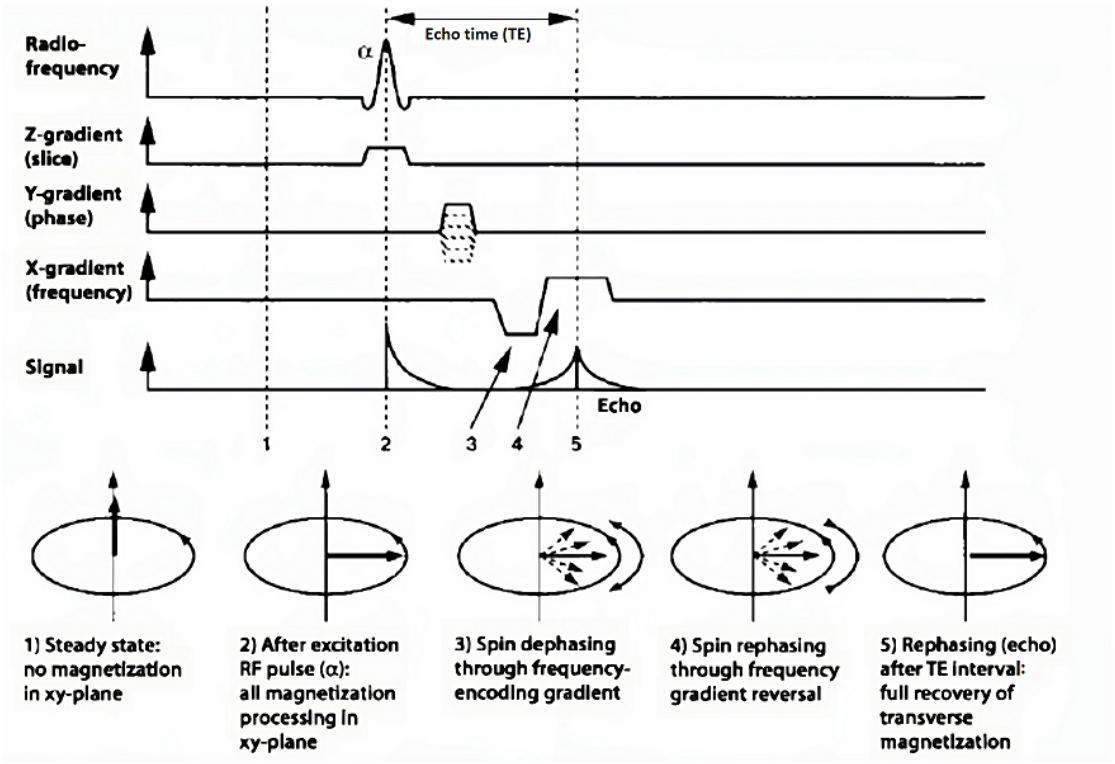

FIGURE 2.4: GRE sequence. A flip angle $\alpha = 90°$ was assumed for simplicity (adapted from [25]).

it useful for specific applications, such as brain imaging and, more particularly, SRS treatment planning (Section 2.8).

Although there are many FSPGR pulse sequence variations (a more detailed discussion of these variations can be found in [44], for example), the 2D FLASH sequence, which is the standard name for the FSPGR, is shown in Figure 2.5. Both frequency and phase-encoding gradients are applied in the transverse direction. However, the key concept of this image sequence, and the one that differentiates it from other gradient echo sequences, is the introduction of a spoiler gradient applied along the slice-selection direction (z, in the case of Figure 2.5). The purpose of this gradient is to destroy any residual transverse magnetization components after data collection. In order to avoid build-up of transverse coherence, the amplitude of the spoiler gradient is varied from one excitation to another [22]. Mathematically, the goal of this gradient is to introduce the *perfect spoiling condition*, which can be represented, for the n-th excitation, as $M_{\perp}^{(n)} = 0$.

Spoiled-GRE sequences such as FSPGR are designed to specifically target transverse (T_2) coherences, making them highly advantageous for producing T_1-weighted images. It should be noted that spoiled-GRE sequences can be obtained in 2D or 3D. The 3D spoiled

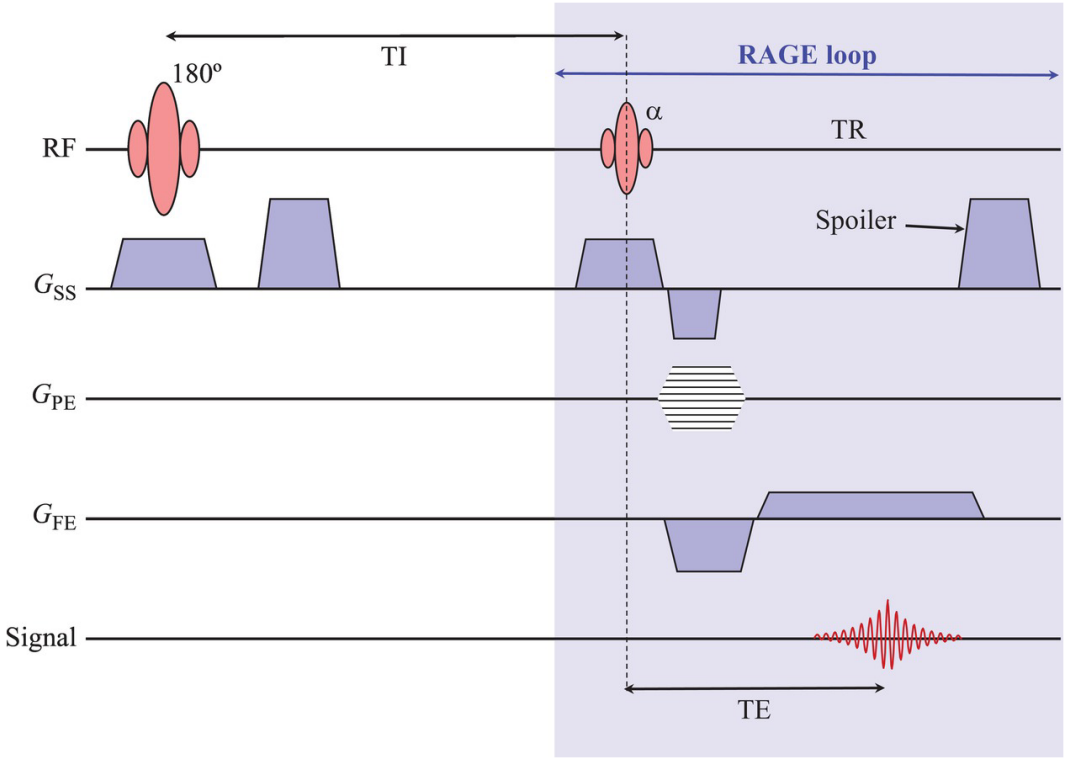

FIGURE 2.5: Pulse sequence for 2D SPGR sequence. For image formation, an inverting prepulse and spoiler gradient are used before the rapid acquired gradient echo (RAGE) loop [21]. This sequence could be used to form a 3D image by using, for example, an additional phase-encoding gradient in z, applied between the two RF pulses. Indeed, IPO-Porto uses the 3D-FSPGR sequence for many imaging applications, including brain imaging.

GRE approach allows the acquisition of thin-slice volumetric images without interslice gaps and multiplanar reformatting [45, 25].

The main limitations of short TR FSPGR imaging are its poor T_1 contrast (if low flip angles are used) and its low SNR compared to longer sequences [21]. However, an inversion pre-pulse followed by a delay can be used to generate T_1 weighting, as shown in Figure 2.5. Moreover, a short TR results in a reduced SNR due to saturation and an inability to compensate for static field inhomogeneities, which leads to decay with T_2^* [17, 29].

On the other hand, the FSPGR sequence has many advantages. The most important one is that, as there is no need to use a 180° refocusing pulse, very short TR times can be used, which makes FSPGR imaging much faster than SE sequences, and result in reduced motion artifacts compared to those of SE sequences, thus making routine 3D acquisitions clinically practical. Moreover, the absence of the refocusing pulse results in lower RF power deposition in patients.[29, 25].

Another advantage of the FSPGR sequence is its superior spatial resolution, which

permits highly detailed anatomical images [46, 47]. This resolution is especially crucial for identifying small structures, such as tumours, with unparalleled accuracy. Compared to T_1-weighted SE sequences, the FSPGR sequence allows us to have a higher contrast for thin-slices images which, together with its high spatial resolution, proves to be particularly beneficial in SRS for precise targeting and monitoring of lesions [48]. Moreover, GRE sequences generally have higher contrast than SE sequences at 3T [45].

Finally, because TE is determined by the distance between the negative and positive gradient lobes or the reduced amplitude of one of the gradients, significantly lower TE periods can be achieved by controlling these parameters. Given that TE controls the degree of T_2^* weighting, different types of contrast mechanisms are possible with this sequence [29].

It should also be noted that the short acquisition time of the FSPGR sequence makes it particularly useful for imaging patients who may have difficulty remaining still during the imaging process, which is especially important in pediatric cases [49]. This is also important in SRS pre-treatment MRI, where patients may be sedated or under general anesthesia, which can make it difficult to obtain high-quality images using sequences with longer acquisition times. This advantage is twofold: not only can sedated patients move involuntarily, but longer acquisition times imply heavier sedation. This can have particularly negative effects in pediatric cases, as recent studies show that sedation and general anesthesia in children might have long-term neurocognitive side effects, in addition to short-term procedure-related risks [50].

2.4 Main Components of MR Scanners

A typical MRI scanner comprises three primary hardware components: a main magnet, a magnetic field gradient system, and an RF system (Figure 2.6). This section briefly describes each of these components.

2.4.1 Main Magnet

The main magnet can be either a resistive, a permanent, or a superconducting magnet. Its primary function is to generate a strong uniform static magnetic field, referred to as B_0 field, which polarizes the nuclear spins of the object placed inside the magnet. Resistive magnets are generally used at low field (< 0.15 T); permanent magnets can operate at field

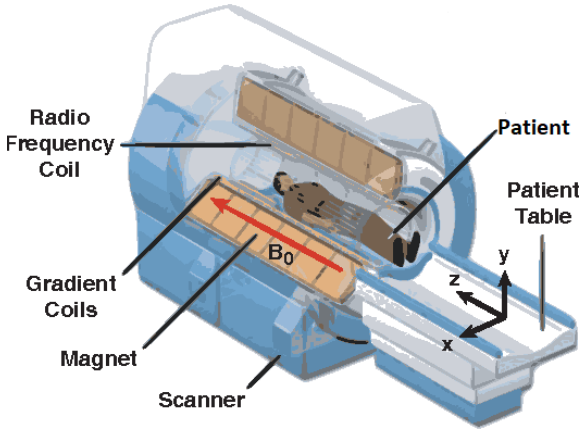

FIGURE 2.6: Common MRI scanner system design. The main magnetic field $\vec{B_0}$ is directed along the scanner bore, as a consequence of Faraday's Law for a magnetic field in a coil (adapted from [51]).

strengths up to 0.3 T; superconducting magnets are normally used to generate higher field strengths [22]. Thus, the latter are the most commonly used type of magnets. In fact, the other magnets have significant disadvantages - resistive magnets need enormous amounts of electricity to operate and permanent magnets are very heavy and hard to build. The very low resistance of the superconducting magnets (due to helium cooling) greatly reduces the system's electricity requirements, making it the preferred and most widely used choice for MRI systems today.

In a clinical whole-body MRI system, the typical field strength ranges from 0.5 to 3 T. The principles and effects of magnetic field strength are analysed in more detail in Section 2.5.

The largest deviation of the field over a specified volume within the region of interest is used to define the main spatial homogeneity of the magnetic field, measured in parts per million (ppm):

$$Homogeneity = \frac{B_{0,max} - B_{0,min}}{B_{0,mean}} \tag{2.13}$$

where $B_{0,max}$, $B_{0,min}$ and $B_{0,mean}$ are the maximum, minimum and mean values of the B_0 field within the region of interest. To provide high quality images, a magnet needs to be moderately homogeneous over a considerable volume. A 3.0 T magnet, for example, can guarantee a homogeneity of 1 ppm in a spherical volume with a diameter of 40 cm. This means that no two points within $\pm$ 20 cm of the isocenter of the magnet have a difference in magnetic field strengths greater than one part in a million, or 3.0 T x $1/10^6 = 3\times10^{-6}$ T

[52]. Failure to generate a homogeneous B_0 field is one of the sources of geometric distortion (Section 2.7). In reality, a field with this level of homogeneity cannot be produced by the main magnet alone. This problem is typically solved by using a secondary compensating magnetic field produced by a set of so-called shimming coils to increase the overall homogeneity of the field to the desired level.

2.4.2 Gradient System

Three orthogonal gradient coils make up the magnetic field gradient system (Figure 2.7). Gradient coils are intended to generate controlled spatial non-uniform magnetic fields, that is, magnetic field whose strength varies linearly along each axis (X,Y,Z). Since Gradient Non-Linearity (GNL) is one of the main sources of geometric distortion (Section 2.7.1), the working principle of the gradient system is presented in this Section.

These gradients allow spatial localization of the signal via frequency and phase encoding. Frequency encoding involves applying a magnetic field gradient to differentiate signal contributions from different locations along the frequency axis (usually defined as being the x-direction). This spatial encoding allows the reconstruction of a one-dimensional projection of the image. On the other hand, phase encoding complements frequency encoding by applying a magnetic field gradient in a different direction (usually defined as being the y-axis) to assign unique phase values to different points within the imaged volume. The combination of frequency and phase encoding enables the formation of detailed two-dimensional images [25, 17].

The Larmor equation (Eq. 2.7) serves as the foundation for encoding spatial information in MRI, since it makes the Larmor frequency of the imaged nuclei spatially dependent during the signal acquisition period [17]. This encoding is done by these three linear magnetic field gradients, which are added to the primary static field during image acquisition. The frequency and phase contents of the MR signals are converted into spatial positions during image reconstruction. Therefore, errors in the position of imaged organs, for example, will arise if the gradient system is not working correctly [10].

The z-gradient (G_z) can be generated by a circular loop coil pair with opposing currents known as a Maxwell pair [53], as shown in Figure 2.7. When the coils are spaced by $\sqrt{3}\,r$, where r is the coil radius, the gradient linearity is optimal, since unwanted spherical harmonic terms that introduce z^3 field variations are eliminated [54]. Other designs, such as spiral windings with variable pitch along the z axis, can generate z gradients with

superior radial linearity [21]. G_y can be generated by the Golay configuration depicted in Figure 2.7, and an identical set of Golay coils rotated through 90° can be used to generate the G_x gradient. The Golay pair can be improved by adding extra coils with different axial placements and opening angles [21, 14]. Some examples of such coil optimization design are proposed in Siebold [55] and Frenkiel et al. [56].

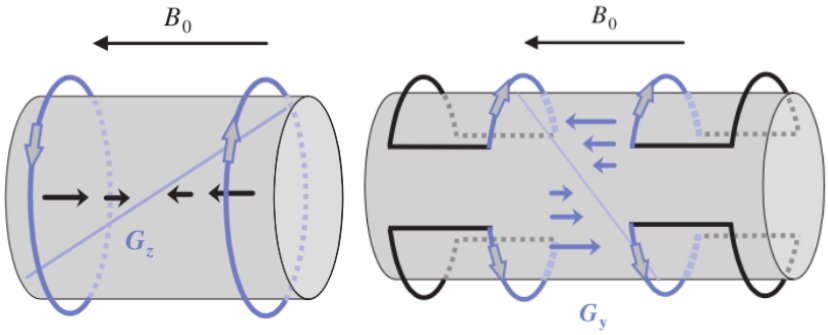

FIGURE 2.7: Maxwell pair configuration for a longitudinal gradient field (left) and Golay coil configuration for transverse gradient fields (right) [21].

A gradient system must meet certain requirements, among them the maximum gradient strength and the speed at which this strength can be attained. In general, the greater the gradient strength, the better the system, since the spatial resolution is improved and the imaging time is shorter. Gradient strength is typically expressed in millitesla per metre (mT/m) units. The criterion that the gradient field must be stronger than the main field inhomogeneity sets the lower bound for the necessary gradient strength [22].

2.4.3 RF System

The RF system includes a receiver coil that converts precessing magnetization into an electrical signal and a transmitter coil that generates the rotating magnetic field B_1, for the excitation of a spin system.

Transceiver coils are so named because they can serve as both transmitter and receiver coil. Because spin excitation and signal detection require resonance at a radio frequency, both the transmitter and receiver coils are commonly referred to as RF coils. The RF component requires a uniform B_1 field and high detection sensitivity, and as a result, MR systems are often equipped with RF coils of various sizes and shapes for a variety of applications [22]. Deciding the optimal RF coil design for MRI demands a careful evaluation of the merits and demerits of each option, while keeping in mind the specific usage situation and the inherent trade-offs involved.

Rigid diagnostic head coils are commonly used in MRI centers. These coils are meticulously designed with optimized coil geometry and sensitivity profiles, often resulting in superior image quality compared to that achieved with flexible extremity coils [57]. Nonetheless, rigid diagnostic head coils are incompatible with most immobilization devices, which limits their utilization in scenarios where immobilization is deemed essential. Regarding the SRS technique, an increasing number of institutions use immobilization devices of various types [58, 59, 60].

On the other hand, the use of flexible extremity coils (Figure 2.8) presents compelling advantages. These coils, usually made of flexible materials such as rubber or silicone, are designed to be more adaptable to the shape of the head, improving patient comfort [61]. They also offer compatibility with immobilization devices and can be seamlessly integrated with radiosurgery headframes, facilitating targeted treatments. However, it is worth noting that while flexible extremity coils may improve image quality, due to their closer proximity to the head, they may exhibit some limitations in this regard due to restrictions imposed by coil geometry and sensitivity profiles [62, 57].

FIGURE 2.8: Rigid head (left) and flexible extremity coil (right). Adapted from [57].

2.5 Magnetic Field Strength

In this Section, the impact of the magnetic field strength is presented. A particular focus will be given to the advantages and disadvantages of using 3T MRI scanners, compared to the more common 1.5T scanners.

The role of 3T MRI scanners is becoming increasingly significant due to its unique advantageous characteristics:

- The main advantage of 3T scanning, compared to 1.5T, is the **signal-to-noise ratio (SNR)**, which is double that obtained at 1.5T [63]. This increase leads to a reduced

acquisition time and an enhanced spatial resolution. This can be particularly useful in certain applications, such as imaging small structures or investigating areas with high structural complexity [64]. In particular, the improved SNR at 3T allows for better detection of small blood vessels [65, 66] and brain metastases [67].

- MRI contrast agents (CAs), such as gadolinium, are essential to create the necessary contrast between tissues in MRI scans. The **contrast between tissues and CAs is better at 3T**, which allows for smaller doses of CAs to be injected, reducing the risk of adverse reactions [63, 68]. This is particularly important in pediatrics, where the use of CAs should be minimized [69].

- The implementation of high-field MRI technology also allows for **shorter acquisition times** [63], reducing scan-related discomfort, anxiety, and compliance issues in patients. Notably, shorter scan times may have beneficial implications for elderly, pediatric, or critically ill individuals.

- Finally, high-field MRI systems originate superior chemical shifts, **improving the spectral resolution** [63], which makes them particularly suitable for spectroscopy applications. Moreover, these systems outperform lower-field scanners in localizing focal regions of tissue calcification, iron accumulation, or hemorrhage, rendering them a valuable tool in a wide range of clinical settings. Using a higher field strength is also important for brain imaging, especially regarding brain metastases detection [67].

However, there are also some downsides to using 3T scanners, which are listed below:

- The aforementioned increase in chemical shift results not only in greater susceptibility effects (such as signal loss at air/tissue interfaces and distortion) but also in an **increase in magnetic susceptibility artifacts** [68, 63], especially for T_2 sequences (Section 2.6). This can be explained by the fact that increasing the magnetic field will result in spin dephasing playing a more significant role. Although bigger susceptibility artifacts are a disadvantage of 3T scanners, they can actually be useful in some cases, such as microbleeding or cavernoma detection [45]. However, it should be noted that gradient echo sequences, such as the FSPGR sequence used in IPO-Porto for brain imaging for SRS treatment planning, are particularly affected by susceptibility [68]. This is due to the fact that they do not have 180° refocusing pulses to counteract spin dephasing (Section 2.3.2).

- Using a stronger magnetic field will **increase the acoustic noise** produced by the currents passing through the gradient coils. While this doesn't directly affect image quality in brain imaging, it can affect patient comfort and anxiety levels, which in turn may cause motion problems [70]. However, nowadays institutions provide auditory protection during scans, so this is mostly a problem in functional MRI, particularly in auditory pathway studies [71].

- Despite the previously stated improvement in contrast between CA and tissues, there is **a decrease in T_1 contrast between tissues** [72], which can be problematic for radiologists who have become familiar with differentiating tissues using 1.5T scanners. This decrease of T_1 contrast at 3T compared to 1.5T is attributed to T_1 lengthening. In brain imaging, it leads to a convergence of white and grey matter relaxation times. This loss in contrast is also present when comparing healthy and pathological tissue. In order to overcome this issue, the repetition time (TR) can be increased to match the T_1 increase, or inversion recovery (IR) methods can be used [68].

- At 3T, the Specific Absorption Rate (SAR) is significantly higher than at lower field strengths, which can lead to an **increase in the patient's body temperature**. This heating is caused by resistive (also referred to as Ohmic or Joules) heating due to induced electric currents. SAR is the amount of energy dissipated in the body, per unit of time, and is measured in Watts per kilogram (W/kg).

  The absorbed RF power per patient mass unit should be carefully controlled to prevent excessive heating, which could cause tissue damage or discomfort during the scan. Thus, institutions that use 3T scanners must optimize their sequence parameters in order to comply with existing guidelines [57]. Spin-echo sequences are the ones most affected by SAR limitations at 3T, so this aspect is usually not a problem in FSPGR brain imaging. Parameter adaptation methods, such as increasing the TR or decreasing the number of slices, can ameliorate this problem, although they all imply trade-offs in image quality or scanning time. Parallel imaging techniques can also reduce SAR [68].

- Finally, there is one additional artifact, the **B_1 artifact**, that can be observed at 3T but not at 1.5T. This issue arises from a much higher and more intense variance of the flip angles at 3T, resulting in a lack of contrast uniformity and possibly signal loss. The

differences in the B_1 (RF) field are not dependent on the manufacturer, but rather on the patients themselves and the body location under examination. As a result of considerable differences in flip angles, the excitation of spins varies, and they respond differently in terms of contrast and signal. At 3T, the wavelengths become the same size as, if not smaller than, the regions under study. The phenomenon is most noticeable in thicker body regions such as the abdomen and pelvis, as well as in skull examinations [63]. This can be a problem for brain imaging, although there are currently many solutions to minimize its effect, as will be seen in more detail in Section 3.1.5.

- 3T scanners are more likely to suffer from **B_0 inhomogeneity-related distortions** [73]. However, this problem is alleviated by the fact that, as previously stated, the SNR increases with the field strength, making it possible to sacrifice some SNR to get greater compensating readout bandwidths. This can be deemed necessary in applications where artifacts and distortion have to be strictly minimized, such as in SRS treatment planning. Furthermore, it should also be noted that modern 3T scanners generally have better shimming to minimize B_0 inhomogeneities than most older 1.5T scanners [74].

These disadvantages of 3T MRI scanning, along with solutions to resolve them, are explored in more detail in Section 3.1.

2.6 Artifacts in MRI

An MRI artifact can be defined as any irregularity noted on an MR image that is related to the imaging process rather than to an anatomical or physiological abnormality. They may be caused by the scanning hardware itself, or by its interaction with the patient, or due to physiological responses. There are nearly twenty types of artifacts; therefore, in this Section, a summary of the most important ones for this dissertation is presented.

In Section 2.5, two types of MRI artifacts have already been mentioned, since they depend on the magnetic field strength: magnetic susceptibility artifacts and the B_1 artifact. Discussion on chemical shift and its resulting image artifacts is reserved for Section 2.7.2.1. In addition to these, the other main types of artifacts in MRI are:

- **Truncation artifacts**, also known as the Gibbs phenomenon, occur near rigid high-contrast boundaries. They appear as a series of alternating light and dark lines - a phenomenon known as "ringing" [75].

- **Motion artifacts** caused by breathing, cardiac movement, blood flow or the movement of the patient, which creates ghost artifacts (Figure 2.9). Saliva production, requiring frequent clearing and swallowing, can also be a problem, particularly when imaging oropharyngeal or laryngeal tumours. Drugs that slow down intestinal peristalsis or cardiac/respiratory gating can all be used to lessen their effects. Gating is a technique that, although it may extend scan times by factors of 2 to 4, basically eliminates both of the problems introduced by motion - loss of resolution and phase-encoded noise [76].

  In brain imaging, subject movement is also problematic. In fact, not only can it create motion artifacts, it can also decrease B_0 homogeneity, further deteriorating the image quality. Currently, there are a number of techniques that can minimize the effect of subject motion, such as immobilizaion devices, neural networks for automatic correction, optical tracking or NMR probes [77]. Each implies a trade-off in either the accuracy, imaging time patient comfort or cost. Fast imaging techniques, such as the FSPGR sequence used in this work, also reduce motion artifacts, given that the probability of the patient moving during the imaging process is proportional to the imaging time.

- **Aliasing artifacts** occur when anatomical components situated outside the field of view are mapped at the opposite end of the image. They can be eliminated by increasing the FOV [75] (Figure 2.9). Aliasing artifacts in MRI are related to the Nyquist-Shannon theorem. This theorem states that in order to accurately reconstruct a continuous signal from its sampled version, the sampling rate must be at least twice the highest frequency component present in the signal. Increasing the FOV solves spatial aliasing problems, while increasing the sampling rate (i.e., receiver bandwidth or number of phase encoding steps) eliminates temporal aliasing [78].

- Metallic and other **foreign bodies** that may be encountered on and in patients' bodies frequently generate artifacts. Following the proposal of Krupa et al. [75], these can be grouped into three main groups:

- Group A - foreign bodies that are known and possible to remove: these are the most common and straightforward to identify and eliminate, frequently associated with clothing or body jewellery, hair ties and clothing labels, but also with medical equipment, such as hearing aids. Cosmetics can also cause substantial magnetic field distortion, making it difficult to examine the contents of orbits. The presence of iron oxide in the pigments used to create dark hues of make-up causes this distortion [79]. As for tattoos, the metallic components in their inks distort the magnetic field, making MR imaging impossible in some cases (Figure 2.9).
- Group B – foreign bodies that are known but impossible to eliminate, e.g., orthodontic implants or endoprostheses. Excessive artifacts can make nearly impossible to recognize important intracerebral pathologies. Such excessive artifacts are caused mainly by orthodontic braces, which are becoming increasingly popular among not only adolescents but also adults. These implants interfere not only with brain MRI but also with orofacial and neck imaging. Neurosurgical clips, ventricular shunt valves and disc protheses also induce significant artifacts in MRI.
- Group C - foreign bodies that are unknown to the MRI unit personnel because patients forget about them, are unaware of them, or fail to report them in the pre-examination questionnaire.

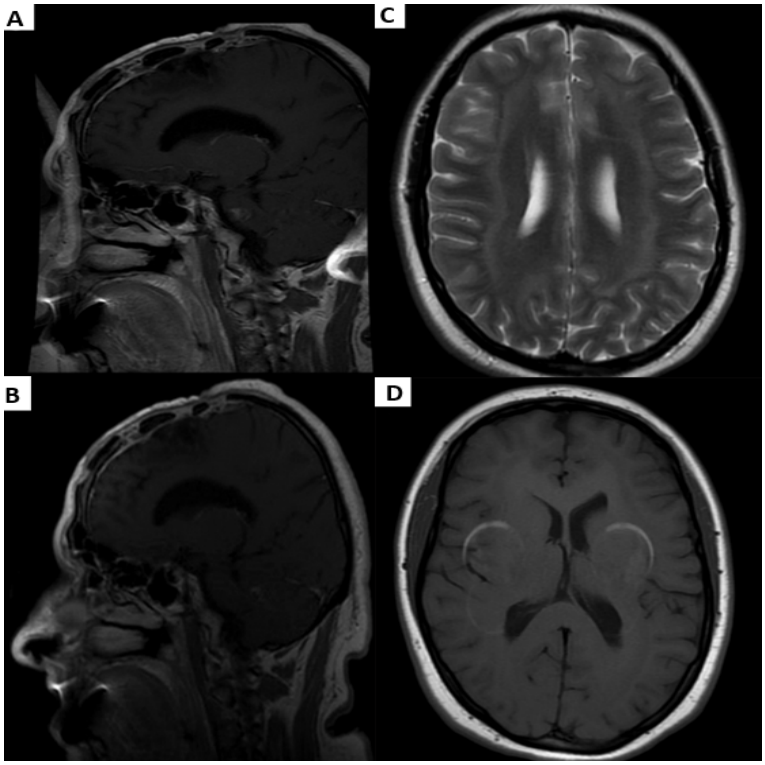

FIGURE 2.9: Aliasing artifact ("wrap around") on brain MRI with FOV=24×18 cm (**A**). For the same patient, changing the FOV to 24x24 cm (**B**) eliminates this problem. Metallic artifacts caused by orthodontic braces in T_1 and T_2-weighted images (**C, D**).

2.7 Geometric Distortion

While MRI has distinct advantages, it also has limitations, such as geometric distortions, signal dropout, and artifacts. When MRI images are used for radiation therapy treatment planning, geometric distortion is a significant factor [80], as it affects the original images, which in turn impacts the delineation of the clinical tumour volume (CTV) and planning treatment volume (PTV) [81]. Given the incorporation of MRI images in RT treatment planning, it is very important to try to minimize the effects of their geometric distortions.

Geometric distortion is still an MRI problem that needs to be corrected [10]. This correction is important, as uncorrected geometric distortions in RT planning can create target localization uncertainties, especially for scanners with higher magnetic field strengths, for the reasons explained in Section 2.5. This dependency varies with the acquisition parameters, but it is always significant in comparisons between 1.5T and 3T scanners [82]. The magnitude of the distortion can be affected by factors other than magnetic field strength, such as the patient's anatomy, receiver bandwidth and the presence of implants [4, 83]. Geometric distortion can also manifest quite differently in different sequences.

Geometric distortion can be classified into two categories: object-dependent and system-dependent [73, 76]. System-dependent distortions are attributed to MRI hardware, including the uniformity of the primary magnetic field and linearity of the magnetic field gradients. This type of distortions is more significant the further we are from the magnet isocenter, given the increased inhomogeneity and linearity of the aforementioned fields in these regions [10]. On the other hand, patient-dependent distortions are linked to magnetic properties such as chemical shift effects and magnetic susceptibility. Although the amplitude of the patient-dependent distortion is lower than that of the system-dependent distortion, it is more challenging to correct [84]. The following subsections will explore these two types of geometric distortion in greater detail.

2.7.1 System-dependent Distortion

Superconducting coils are the backbone of MRI scanners. By passing a large electrical current through them, these coils generate the magnetic field that makes MRI possible (Section 2.4). The shape and position of the coils, as well as the current flowing through them, determine the orientation of the magnetic field. Despite the best design efforts, small variations in the magnetic field inside the bore will still occur, which can result in geometric distortion of the MRI image. Therefore, optimizing coil design and positioning is crucial to produce a uniform and homogeneous magnetic field [22].

The homogeneity of the static magnetic field (B_0) generated by the imaging magnet is critical for the geometric properties of the MR data; it can be adjusted through active and/or passive shimming. Active shimming is achieved by inserting special shim coils into the magnet system, making the resultant B_0 magnetic field more homogeneous. Passive shimming is accomplished by wrapping pieces of ferromagnetic metal around the magnet bore (tunnel) to produce the same result.

The three linear gradient magnetic fields utilized to spatially encode the various structures producing MR signals are created by special gradient coils introduced into the magnet's bore (Figure 2.7), as explained in Section 2.4.2. It has been observed that in clinical MRI systems with superconducting magnets, the geometric distortion resulting from gradient field nonlinearity is much more prominent than that caused by static B_0 field inhomogeneity. This is particularly true in modern MRI systems, where smaller gradient coils are used to achieve greater gradient performance. The distortion caused by gradient field nonlinearity can reach a maximum of 10 mm for 1.5 T systems on the peripheral regions

of a 30 cm plane axial imaging sequence [85]. Thus, far from the center of the imaged region, this type of distortion can be ten times greater than that of the distortion caused by B_0 inhomogeneity. However, it should be noted that this is an extreme scenario in brain imaging, where the FOV is usually 24x24 cm and centered on the region of interest.

With cutting-edge shimming technologies incorporated in superconducting magnets, it is possible to achieve a remarkable uniformity of 1 ppm. At a magnetic field strength of 1.5 T, this translates to a negligible maximum field deviation of 1.5 µT. Consequently, the resulting geometric distortion, when subjected to the gradients commonly employed in modern MRI systems ($\sim$2 mT/m or 2 µT/mm), would be minimal, measuring less than 1 mm [85]. However, not only is this an optimistic estimate, because not all centers have access to cutting-edge shimming technologies, but the distortion at 3 T is greater than at 1.5 T. This is partly due to the fact that 3 T scanners are more likely to exhibit B_0 inhomogeneity-related distortions, as stated in Section 2.5. Thus, it becomes imperative to maximize B_0 uniformity and gradient field linearity, especially when using 3 T scanners. These "cutting-edge technologies" encompass recent developments such as the usage of a larger number of coils [86] or the incorporation of advanced hardware and software details that, while costly, may allow for accurate real-time distortion minimization [87, 88]. As for gradient nonlinearity (GNL) correction, there are techniques specifically tailored to correct it [89], while shimming methods usually correct for combined influence on image distortion by homogenizing the fields [90]. Thus, shimming systems can attenuate GNL, but they are not specifically designed for it.

It can be concluded, especially for system-dependent distortions in commercial MRI scanners, that their two main sources are GNL and a non-homogeneous static field. The former factor includes the effects of eddy currents [14, 90] generated by gradient switching during image acquisition, and tends to be more significant than the latter in modern MRI scanners [91]. These effects are reproducible for each scanner, but vary for different field strengths and vendors [92]. Therefore, they must be examined throughout the commissioning process.

2.7.1.1 Barrel Distortion

Barrel distortion is a type of distortion in MRI images that presents itself as a bulging or "barrel-shaped" appearance, mainly around their edges. Its occurrence is frequently

associated with system-dependent causes, such as the generation and shaping of the magnetic field within the scanner. This distortion can be corrected using post-processing techniques, as explained in Section 3.5, and the developed algorithm presented in Section 4.3 also takes this type of distortion into account.

2.7.2 Patient-dependent Distortion

The two main causes of patient-dependent distortions are chemical shift and magnetic susceptibility effects, which will be summarized in this Section. Patient-dependent distortions usually increase at higher magnetic fields [10]. It should be noted that while the hardware-related sources that cause system-dependent distortions can be measured and characterized for individual systems (by using active and/or passive shimming, for example), patient-dependent distortion depends on the imaged tissue and , as the name indicates, on the individual. Therefore, its assessment is more complex and usually requires special modeling.

2.7.2.1 Chemical Shift

Protons in adipose tissue bonded in carbon-hydrogen chains have a slightly different resonance frequency than protons in water. This discrepancy amounts to approximately 3.5 ppm, or 150 Hz at 1.0 T. The spatial encoding mechanism cannot discriminate between the water and fat signals, and when the water frequency is used as the reference frequency, the fat signal is mispositioned. It is important to note that the higher the magnetic field strength is, the more pronounced this effect will be. This is because the readout gradient's bandwidth is usually insufficient to compensate for the increase (in Hz) of the chemical shift observed at higher fields. The chemical shift difference between water and fat, for example, is 30 Hz at 0.2 T and 220 Hz at 1.5 T [10]. For a given magnetic field, the chemical shift, in pixels, can be obtained dividing the frequency difference by the readout gradient bandwidth.

Chemical shift distortions may impact SRS treatment planning due to misalignment of anatomical structures and potential inaccuracies in target delineation. In general, however, this source of distortion is not significant enough by itself to create significant anatomic or dose errors [93]. Chemical shift artifacts can be mitigated by increasing the bandwidth, which is usually enough for brain imaging, but fat-suppressed imaging protocols can be used for more severe cases [94].

2.7.2.2 Magnetic Susceptibility

The magnetic susceptibility χ of a material is a dimensionless proportionality constant that indicates its degree of magnetization in response to an applied magnetic field. Local field changes occur at the interface between tissues with differing susceptibilities as a result of their different magnetizations. This causes geometric distortions in MRI because the magnetic field at those locations will differ from the expected field intensity given by the main, static, and gradient fields at those coordinates. The presence of these distortions in MRI images, which are hard to predict, poses a significant challenge for standard post-processing correction algorithms [91]. It requires meticulous attention, particularly when these images are used as the sole source for SRS planning.

At tissue-air interfaces, such as the nasal cavities and the patient's outline, susceptibility effects are particularly noticeable *in vivo*. At these interfaces, susceptibility can cause field shifts of up to 9 ppm [95]. The assessment of susceptibility effects in MR images is difficult, since it depends on the form of the imaged object and its orientation in the magnetic field. Therefore, experiments conducted to evaluate the impacts of susceptibility on the geometric accuracy of MR image data have very strict setup requirements, since its conditions (shape, orientation and composition of the used phantoms) need to be closely reproduced [10]. An analysis of recent susceptibility quantification tests [96, 97] suggests that the anthropomorphic phantom used in this study (Section 4.1.1) could be used for susceptibility estimation. The translation to patient data would be better for this phantom than for the geometric phantom introduced in Section 4.2, given its anatomical accuracy.

Susceptibility-induced distortions, like chemical shift effects, are more pronounced at high fields and are directly related to the bandwidth of the readout gradient, G_{read}, which is the frequency encoding gradient turned on during signal acquisition in GRE sequences. A first approximation of the maximum position error due to magnetic susceptibility differences ($\Delta\chi$) is given in [95]:

$$\Delta x = \frac{\Delta\chi B_0}{G_{read}} \tag{2.14}$$

For standard values for these variables, Δx is approximately 0.8 pixels at 0.2 T, but this value can reach 6 pixels at 1.5 T (due to the increase in B_0). However, the susceptibility effects in vivo will frequently be smaller, since this estimate corresponds to the maximum

position error that can be expected to occur. They can be reduced by using stronger gradients, but given the lack of easily implementable post-processing correction methods for this type of distortion, it is still considered a major issue at 3 T and above [85]. In the context of head imaging, it is more problematic at tissue/air boundaries such as the near the meninges and skull than in the brain itself. Regarding phantoms, this distortion can be minimized by using materials that have susceptibilities within about $\pm$ 3 ppm from water [10], such as acrylic (which was used in the geometric phantom designed in this thesis).

Patients with any foreign metallic object (such as medical or cosmetic implants) in the body are, due to their susceptibility effects, particularly concerning in MRI. This is due to the increased susceptibility distortions that can arise in close proximity to such objects. In fact, in some cases, these foreign objects present MRI examination contraindications [98]. Metallic dental objects, such as implants, are also a source of artifacts for brain imaging (Figure 2.9 C, D). Its difficult to avoid the effects of metallic orthodontic implants, particularly when their removal is not possible [99]. These artifacts can be easily misinterpreted as focal lesions in FLAIR sequences, but on T_1-weighted sequences such as FSPGR they can be properly interpreted [75].

2.8 Stereotactic Radiosurgery (SRS)

In the field of radiation therapy, stereotactic radiosurgery (SRS) is an important technique, which can treat tumours that are not accessible surgically in a non-invasive way and without requiring the patient to stay hospitalized. It requires not only advanced imaging methods but also advanced computerized planning systems. By using them, a higher dose of radiation can be delivered with great precision to small targets that are precisely delineated within the head, including tumours or functional lesions in the brain. Thus, the main purpose of SRS is to deliver a substantial amount of radiation to the target area, while minimizing the exposure of surrounding healthy tissue through a highly accurate positioning and monitoring of the patient [100].

SRS typically utilizes a linear accelerator that produces high-energy photon beams. At present, 6 MeV and 6 MV FFF (flattening filter free*) photon beams are the preferred beam energy for SRS. These beams are carefully directed at the target area using a specialized

*The flattening filter in a linear accelerator is a component that helps to distribute the radiation beam more uniformly across the treatment field by reducing the intensity of the beam's central portion. Given the resulting higher dose rate, it is important for high dose treatments, such as SRS [101, 102].

collimator to shape and guide them. To maximize effectiveness, radiation is delivered from multiple angles using conformal dose delivery, which customizes the radiation to fit the target's shape. It is important to mention that linear accelerators can produce electron beams, but they are only used for targets near the skin due to their unique characteristics of electron beams, making them unsuitable for most SRS treatments.

SRS is generally used to treat small, well-defined tumours or other lesions located in hard-to-reach areas of the brain, or patients who are not candidates for surgery. It is also used for treating benign or functional lesions in the brain such as arteriovenous malformations, pituitary adenoma, and trigeminal neuralgia [103]. Moreover, SRS is acknowledged as an important technique in the treatment of brain metastases. While the SRS treatment plan primarily utilizes CT images, MRI images are integral to precisely identify metastases. This is due to the fact that most small brain lesions are not visible on CT, even with contrast agents, but are easily seen on MRI, although for SRS patients a contrast agent is usually used to get the best possible accuracy.

Indeed, although MR images offer good soft-tissue contrast, allowing for better delineation of GTV and OAR, geometrical distortion is one of the main barriers to their optimal use in SRS planning. Thus, CT is still widely employed to generate geometrically precise reference images. CT scans also contain electron density information and can be registered with MR images for geometrical distortion correction [104].

Image-guided radiosurgery is an example of an MR application whose full potential is still limited by the presence of geometric distortion [91]. This approach currently employs both MR and CT images. Because of the likelihood of geometric distortion in MR images, CT is used for spatial localization in treatment, while MRI is utilized to provide better tumour characterization previous to treatment planning [85]. This approach is inefficient, since it is time consuming.

Moreover, in recent years, the use of structural MRI for investigating various brain pathologies has risen significantly. Numerous studies have extensively documented cross-sectional and longitudinal MRI findings related to epilepsy, multiple sclerosis, Alzheimer's disease, and other brain disorders [e.g., 105, 106, 107]. The focus of these studies is to extract valuable structural data, primarily volumes and shapes, from MRI images [85, 17]. Such data is critical for improving our understanding of the pathological mechanisms underlying these disorders.

However, while the broad consensus among these studies appears to converge, there are discrepancies [85]. The diversified character of the disease or errors (both subjective and objective in nature) associated with the derivation of the volumes from structural MRI were assumed to be the cause of some of these disparities. Nonetheless, geometric distortion is a potential cause of errors that has received little attention. This is most likely owing to the lack of an adequate technique to provide a convenient and accurate measurement of geometric distortion in structural MRI. Putz et al.[74] suggests that the fact that MRI has traditionally been beyond the scope of the radio-oncologist may be another reason why some of the risks associated with MRI-based radiation treatment planning have not been totally eliminated.

In radiosurgery, spatial localization of tumours in the brain is often requires an accuracy of less than 1 mm. In Paulson et al. [108], for example, full consensus was reached that geometric distortions should be no greater than 1 mm for stereotactic brain treatments and 2 mm for non-stereotactic brain treatments. Despite the fact that MRI scanners are designed to have the most homogeneous static field and linear gradient fields around the isocentre, geometric distortion that falls within 1 mm inside a volume the size of a human head (180 mm in diameter) is still beyond the reach of most clinical MR scanners [85].

Thus, there have been many studies on geometric distortions in MRI scanners [e.g., 109, 110], with particular emphasis on the effect on spatial localization in the treatment of brain tumours. However, the majority of these investigations were conducted in two dimensions. In other words, geometric distortion was only explored within the imaging plane, while distortion along the imaging plane's normal was frequently ignored [74, 111]. If the results are not carefully used in treatment planning, these incomplete measurements may be detrimental. Thus, 3D distortion localization is also critical for radiosurgery planning. This is particularly true for peripheral locations [85] due to the fact that, in MR systems, geometric distortion can be considerably larger in regions that are farther from the isocentre [112].

2.9 MRI Acquisition Parameters

At the heart of MRI lie the image acquisition parameters, which determine the quality and characteristics of MRI images. These parameters include but are not limited to, magnetic

field strength, pulse sequence type, imaging plane, field of view, spatial resolution, repetition time (TR), echo time (TE), and flip angle. These parameters are carefully chosen to optimize the MRI acquisition process and obtain images that provide accurate and detailed information about the anatomy and pathology of the imaged region. Thus, optimizing MRI acquisition parameters is a challenging task that requires a deep understanding of the underlying physics of MRI and a keen sense of its clinical application.

One of the key parameters in MRI acquisition is the magnetic field strength, explored in Section 2.5. Another critical parameter is the type of pulse sequence used, which affects the contrast and spatial resolution of the images. There are various pulse sequences available, such as T_1-weighted, T_2-weighted, and proton density-weighted sequences, each with its own strengths and limitations, already detailed in Section 2.3. Scanning at the highest resolution possible is advised to increase measurement accuracy and allow the visualization of small structures [113]. In practice, the spatial resolution is mostly limited by the imaging time.

The imaging plane, which is the orientation of the image with respect to the body, is another important parameter. The choice of imaging plane depends on the anatomy of the region of interest and the specific clinical question addressed. For example, axial images are commonly used for brain imaging, while sagittal or coronal images may be more suitable for imaging the spine or joints. The field of view (FOV), which is the size of the imaged region, is another crucial parameter that needs to be optimized based on the specific clinical requirements.

The repetition time (TR), which is the time interval between successive pulse sequences, and the echo time (TE), the time at which the MRI signal is sampled, are critical parameters that affect the image contrast and signal characteristics, and were introduced in Section 2.3. In general, images with short TR and short TE generate T_1-weighted images, while those with long TR and long TE generate T_2-weighted images. Precise specifications of reference ranges are not commonly outlined; nevertheless, it is customary for "long" TR or TE to be in a range of 3-5 times the value of T_1 or T_2, respectively. Conversely, the term "short" implies TR or TE values significantly smaller than the respective T_1 or T_2 values [114]. Optimizing TR and TE depends on tissue properties and desired image contrast, and requires careful consideration to achieve the best results.

The flip angle, which is the angle at which the magnetic spins are tipped by the RF pulse, is another parameter that affects the image contrast and signal characteristics. For

spoiled sequences such as FSPGR, the MRI signal is maximized for the Ernst angle (α_E), given by $\alpha_E = arccos(e^{\frac{-T_R}{T_1}})$ [115]. Also, for this sequence, the flip angle should be lower than 20° in order to get T_1-weighted contrast [116].

Slice thickness in MRI represents the section of the anatomical volume that is captured in a single image or slice in the z-axis direction. Thinner slices provide higher spatial resolution and better image quality, but may require longer scan times. Thicker slices may be used in certain clinical situations where faster scan times or thicker tissue sections are needed, but at the expense of reduced spatial resolution. The choice of slice thickness in MRI is determined by the clinical indication and imaging protocol, aiming to balance the need for spatial resolution with other clinical factors. An incorrect choice of this parameter can lead to significant errors. It has been shown, for example, that the error in volumetric estimation can surpass a significant 10% when the GTV is visualized on fewer than 5 slices, particularly in the context of small brain metastases [117]. Additionally, partial volume effects often result in an overestimation of GTV volume when the slice thickness is excessively high. A moderate consensus of 3 mm slice thickness for MRI simulation imaging protocols was reached in Paulson et al. [108]. Another publication, by the National Electrical Manufacturers Association (NEMA), recommended a maximum slice thickness of 3 mm for 2D acquisitions and 1.5 mm for 3D acquisitions [113].

Optimizing MRI acquisition parameters is not a one-size-fits-all approach. It requires tailoring the parameters to the specific clinical question, the anatomical region being imaged, and the desired image characteristics. However, one must not only be mindful of wrong software settings that, since even seemingly insignificant objects like earrings or ear studs left inside the magnet can lead to significant unnoticed distortions [108]. This highlights the importance of regular quality assurance measures to ensure that the images obtained are optimal for brain stereotactic radiotherapy, alongside the optimization process. Furthermore, the field of MRI is constantly evolving with advancements in technology and research, presenting new possibilities as well as challenges.

2.10 Image Registration

Image registration, the process of aligning two or more images into a common coordinate system, plays a crucial role in medical imaging [118], enabling the fusion of complementary information from different imaging modalities. To attain the full potential of MR

images for target identification in radiotherapy, it is necessary to align them with the corresponding CT images through registration techniques [10].

MRI-CT registration is a delicate process, where differences in image contrast, resolution, and acquisition protocols between these two image types can pose significant challenges. The intrinsic differences in image intensity and tissue contrast in MRI and CT images demand sophisticated algorithms and techniques to achieve accurate alignment. This requires a deep understanding of the underlying image acquisition principles, mathematical transformations, and registration algorithms.

One of the key aspects of MRI-CT registration is the selection of appropriate similarity measures or cost functions that quantify the similarity between the two images. These measures can range from simple intensity-based measures such as mutual information, normalized mutual information, or correlation coefficient, to more complex measures that incorporate anatomical information or statistical models [119, 120]. The strengths and limitations of each similarity measure must be analysed, considering its suitability for the specific MRI-CT registration task at hand.

Another crucial factor in MRI-CT registration is the choice of transformation model that describes the spatial relationship between the two images. This can range from rigid or affine transformations for global alignment to deformable models to capture local anatomical differences [121, 122]. The selection of an appropriate transformation model requires careful consideration of the anatomical regions being registered, the expected deformations, and the desired accuracy of registration.

Typically, the registration methods employed assume that the scanned volume can be treated as a rigid entity. Then, a coordinate transformation using translation, rotation, and linear scaling of the datasets is used to correlate images from the two modalities. The registration steps and matrices used in this work are presented in Section 4.1.1. However, it should be noted that this rigid body assumption only holds true if we can disregard non-linear geometric distortion of the MR data and organ motion during the MR and CT scans [10].

To aid in the alignment process, a useful tool is to simultaneously display the CT and MR images in an overlaid view (image fusion). This synthetic image view allows for flexibility in varying the content of CT and MR information, ranging from 0 to 100% CT combined with 100 to 0% MR (known as ”gray scale fusion”), or by using pseudocoloring techniques to combine them.

Recently, there have been significant advancements in deep learning-based registration techniques [e.g., 123, 124]. Convolutional neural networks (CNNs) and other deep learning architectures have shown promising results in various medical image registration tasks, including MRI-CT registration. These techniques leverage the power of data-driven learning to capture complex image patterns and deformations, potentially overcoming some of the limitations of traditional registration approaches.

In the pursuit of accurate MRI-CT registration, one should also be mindful of the clinical applications and implications. The fused images obtained through MRI-CT registration can be used for a multitude of purposes, ranging from treatment planning and guidance to image-guided interventions and image analysis. Therefore, it is imperative to ensure that the registered images are not only geometrically accurate but also clinically meaningful, providing valuable information for diagnosis and treatment decisions.

Regarding clinical use of image registration in patients, the displacement of structures in MR images is most prominent along the patient's outline. This has implications for registration techniques that rely on external landmarks placed on the skin or surface matching of the skin surface, or the utilization of stereotactic frames, as they can be sensitive to geometric inaccuracies present in the MR data. However, bony structures can be considered more reliable landmarks for image data registration. This is because bones, as rigid bodies, are usually not affected by object-induced distortions and are located further away from the patient's outline. Therefore, the use of bony landmarks may be a more robust technique for accurate registration of MR images than the use of stereotactic frames or external landmarks [10].

Chapter 3

State of the Art

In this Chapter, some of the phantoms used in the measurement of geometric distortion in MRI are presented, as well as their design considerations. The main distortion correction methods developed and their current limitations are also explained.

3.1 Methods to resolve 3T disadvantages

3T MRI is a widely used imaging modality due to its high spatial and temporal resolution, excellent soft tissue contrast, and non-invasive nature. However, 3T MRI is not without its disadvantages, as explained in Section 2.5. In this Section, an overview of the current methods to resolve each previously listed 3T disadvantage is presented. Previously mentioned solutions are revisited in greater detail, and new ones are described.

The current state of the art in 3T MRI includes various correction and mitigation methods aimed at overcoming the disadvantages of using a higher field compared to the previously ubiquitous 1.5T scanners. These methods include correction of magnetic field inhomogeneities, mitigation of power deposition and heating, and improvements in imaging efficiency and speed. The continued development of these techniques is expected to provide improved diagnostic accuracy and patient comfort in 3T MRI.

3.1.1 Magnetic Susceptibility Artifacts

As mentioned in Section 2.5, magnetic susceptibility artifacts are a common problem in MRI imaging, especially in higher field strengths such as 3T or in patients with metallic foreign bodies such as orthodontic implants.

In order to minimize susceptibility artifacts caused by metallic foreign bodies, it is recommended to use SE sequences with a short TE [125]. The use of SE-based pulse sequences is highly favored over GRE sequences due to their increased robustness against signal loss and artifacts arising from metal interference [57]. Fast SE sequences are preferred over conventional SE sequences, as they tend to produce less prominent artifacts [126]. However, this approach may not always be feasible or significantly improve image quality [75]. A new sequence, Iterative Decomposition of Water and Fat with Echo Asymmetry and Least-squares Estimation (IDEAL), was developed to separate fat and water with a high SNR, and it is insensitive to magnetic field inhomogeneity. IDEAL has been shown to reduce metallic artifacts, especially in postoperative patients with metallic hardware [127], and improve fat suppression [128]. GRE and echo-planar sequences should be avoided as they tend to accentuate susceptibility artifacts [129]. However, in some cases where this is not possible, a TE reduction in a GRE sequence can still be helpful, as was done in this thesis and in other studies with a focus on precision.

In addition to these approaches, there are also hardware solutions that can be used to minimize susceptibility artifacts in MRI. These solutions include the use of specialized coils and shielding materials to reduce the effects of magnetic field inhomogeneities. Additionally, the use of high-performance gradient systems can help to reduce gradient-induced distortions and improve image quality [55, 56].

3.1.2 Increased Acoustic Noise

A major challenge in MRI with higher field strengths is the increase in acoustic noise generated during image acquisition. This increase in noise is due to an increase in several factors, including the magnetic field strength, radiofrequency power, and gradient fields. This noise can be disturbing for the patient and can cause physiological responses such as hearing damage, tinnitus, and increased stress levels, even at 1.5T [130]. Therefore, minimizing acoustic noise is crucial in MRI to ensure patient comfort and safety. There are several possible approaches to achieve this goal, which can range from reducing the noise the scanner produces to reducing the noise that reaches the patient's ear canal.

In MRI, the gradient system is the primary source of acoustic noise. This noise arises from the rapid fluctuations of electrical currents within the gradient coils, which, when combined with strong magnetic fields, lead to significant Lorentz forces exerted on the

coils [131]. These forces cause the coils to knock against their formers, generating acoustic noise that can impact patient comfort and potentially disrupt the imaging process by causing patient motion, for example.

As the gradient input changes, so does the nature and intensity of the audible noise generated during MRI. Generally, reducing slice thickness, FOV, and TE is expected to increase acoustic noise levels. Studies have shown that the simultaneous use of different gradients, such as in three-dimensional acquisitions, as well as gradients with rapid rise-times (fast imaging) or switching times (echo-planar-type imaging), result in the highest levels of acoustic noise [21, 131].

One approach to reducing acoustic noise in MRI is to use gradient hardware with optimized acoustic properties. Adaptations designed to block the coil's resonance frequency result in a sound pressure level reduction of up to 10 dB [132]. Additionally, the use of special acoustic padding and insulation materials around the scanner can help to absorb and reduce the noise level.

Another strategy to mitigate acoustic noise in MRI is the use of advanced pulse sequences that generate less noise. This includes the use of silent pulse sequences that use lower gradient strengths and switching rates, resulting in less acoustic noise. Heismannn et al. [133] obtained total acoustic noise reductions of 16.8 dBA and 14.4 dBA for the clinical-routine GRE and fast spin echo sequences, respectively, corresponding to sound pressure reductions of 86% and 81%.

Moreover, the distinctive properties of the gradient waveform and its accompanying vibratory effect on gradient generators yield an acoustic noise that exhibits a pseudo-periodic behavior. Therefore, the use of headphones with active noise cancellation is another alternative. While the concept of using antiphase acoustic noise to reduce MRI noise is not new, it presents an advantageous prospect, particularly with the recent developments in AI models. This approach provides substantial noise reduction without compromising the performance of the MR system's gradients or pulse sequences [131]. The successful implementation of this technique necessitates substantial amounts of rapid processing, but developments in digital signal processing technology have made these demands more affordable and accessible.

Furthermore, to minimize the negative effects of acoustic noise, patients are often provided with earplugs or headphones to reduce the noise level. However, some patients may not tolerate these methods, and healthcare workers may not be able to effectively

communicate with the patient during the scan [134]. The latter can be solved by using MRI compatible headset/microphone combinations.

The exposure of operators to acoustic noise in MRI is an important issue in interventional MRI procedures. Noise levels generated by rapidly switched gradient magnetic fields can exceed 100 dBA, which is well above the occupational exposure limits in many countries. Permanent hearing loss may occur with daily exposure greater than 80dBA [135]. Therefore, auditory protection should also be provided to interventional radiologists, since interventional MRI will otherwise pose a real risk of significant hearing loss due to the accumulative acoustic exposure of the operators.

Finally, it should be noted that there is ongoing research in ultrashort TE methods, as well as potentially silent gradients. These methods produce MR images that are almost silent [136], with acoustic noise levels comparable to ambient room noise values. Although not yet financially viable when compared to solutions such as using disposable earplugs, they hold promise as potential "near-perfect" solutions. Toshiba, for example, has recently developed the Pianissimo acoustic noise solution [137], which uses the results of Katsunuma et al. [138] to increase attenuation to $\sim$30dB.

3.1.3 T_1 Contrast Decrease

At higher magnetic field strengths, T_1 contrast between tissues can decrease due to shorter T_1 relaxation times at higher magnetic fields, reducing signal differences between tissues and diagnostic accuracy. However, advanced techniques can be used to improve T_1 contrast and enhance image quality.

One such technique involves the use of specialized contrast agents, such as Gadolinium-based contrast agents, which can increase T_1 contrast by shortening the T_1 relaxation time of specific tissues. Advanced techniques such as Magnetization Transfer Contrast (based on the application of off-resonance radio-frequency pulses and subsequent observation of their effects [139]) and Chemical Exchange Saturation Transfer (based on applying a frequency-selective saturation pulse to mobile protons and observing the exchange transfer of signal loss [140]) can also be employed to improve T_1 contrast between tissues with similar T_1 values.

Another technique to improve T_1 contrast is to use specialized pulse sequences. Spoiled Gradient Echo sequences (such as FSPGR, introduced in Section 2.3.2 and used as the experimental imaging sequence in Section 4) can generate T_1-weighted images with high

tissue contrast, while Inversion Recovery sequences can null the signal from specific tissues, enhancing contrast between the remaining ones.

Additionally, there are a host of advanced image processing techniques that can be employed to improve image quality in MRI, such as image reconstruction. The process of image reconstruction involves utilizing tomographic images acquired at various angles around the patient in order to mathematically construct a complete image. Through this process, significant enhancements to image quality have been observed, making it a critical component of modern imaging technologies [141]. Post-processing algorithms can also be used to improve the contrast between tissues, rendering even subtle differences more visible. Moreover, the use of parallel imaging and multi-channel coils has proven particularly advantageous in enabling faster imaging and higher spatial resolution, leading to better differentiation between tissues with similar T_1 relaxation times.

3.1.4 Patient Body Temperature Increase

Another important area of research in 3T MRI is the mitigation of power deposition and heating. At higher magnetic field strengths, one of the paramount difficulties is the propensity to increase patient body temperature during imaging due to resistive losses. Since the SAR is proportional to B_0^2, its value at 3T will be 4 times larger than the SAR at 1.5T [63]. The primary contributor to this power deposition is the absorption of radiofrequency energy by the patient's body, which can result in tissue heating and consequent thermal damage. Thus, it is critical to manage and closely monitor patient body temperature during MRI to ensure patient safety.

Advanced RF coil designs represent a promising approach to regulate body temperature during MRI. These RF coils are designed to limit the amount of RF energy absorbed by the patient's body, thereby minimizing the amount of heat generated. They also optimize the coil performance, in order to reduce its peak RF power [142]. This is especially important for patient with deep brain stimulation implants, who are sometimes not imaged using MRI due to heating concerns. Sophisticated cooling systems, including water cooling, can further aid in removing excess heat from the RF coils, preventing thermal injury. B_1 shimming has also been shown to significantly reduce SAR, even at magnetic fields up to 7T [143].

Another method to manage body temperature during MRI involves the use of specialized pulse sequences and acquisition parameters that restrict the amount of RF energy

absorbed by the patient's body. Prost et al. [144], for example, examined three techniques to reduce RF power deposition: increasing pulse width while reducing RF peak amplitude, using gradient echoes instead of spin echoes, and diminishing the flip angle of the phase reversal pulse. Out of these methods, utilizing gradient echoes was found to be the most efficient in both minimizing the power transmitted to the body and attaining swift data acquisition. Additionally, using reduced phase reversal pulses was identified as an effective strategy to obtain quick T_2-weighted images while decreasing the power delivered to the body by roughly 40%. Wheaton et al. [145] used an approach that employed a partial k-space acquisition for $T_{1,\rho}$-weighted MRI sequences that also reduced the SAR by 40%, in human brain images. In general, shorter sequences, or those with higher TR (which reduce the frequency of energy deposition and allow for thermal relaxation between pulses) are preferred in order to minimize the SAR [63].

The emergence of parallel transmission techniques, notably multi-transmit, merits a brief discussion for their potential to regulate RF energy distribution within the patient's body [146]. Multi-transmit is an MRI technique that leverages multiple RF coils to transmit the signal, thereby enhancing image quality, minimizing artifacts, and improving the magnetic field uniformity. This technique can overcome imaging challenges in specific anatomical regions. However, multi-transmit usage requires careful configuration, since the technique uses more RF coils and may cause injuries due to increased peak power deposition. This risk is complex and dependent on the patient's anatomy [147]. Nevertheless, parallel transmission techniques can hasten imaging while reducing the necessary RF waves [63]. At 3T, such techniques are particularly beneficial since the higher SNR allows for more optimization options. In fact, the resulting small loss in SNR, such as the 2% loss reported by Wheaton et al. [145], can be considered negligible compared to the substantial SAR reduction (almost 50%, in that study).

In addition to the aforementioned factors, continuous monitoring of patient body temperature throughout the MRI examination is essential to guarantee patient safety. This may be achieved through the use of temperature monitoring devices, such as thermocouples [148] or fiber optic probes [149], which may be inserted into the patient's body or placed on their skin (although superficial sites such as the forehead, axilla, and groin are widely utilized due to their accessibility, they are subject to a multitude of external factors that can affect their accuracy, including perspiration, ambient air circulation, humidity, use of blankets, and peripheral vasoconstriction). These devices enable real-time

monitoring of patient body temperature and allow MRI technologists to take timely and appropriate action in the event that temperature levels exceed safe thresholds.

3.1.5 B_1 Artifact

Artifacts due to the RF magnetic field pulse (also known as B_1 field) are a well-known obstacle in MRI at higher field strengths, such as 3T. These artifacts arise due to fluctuations in the B_1 magnetic field, leading to inconsistencies in signal intensity and suboptimal image quality. However, several techniques can be implemented to overcome these artifacts and enhance the image quality in MRI.

One of the ways to mitigate B_1 artifacts is through the use of advanced pulse sequences, such as adiabatic pulses [150], designed to compensate for B_1 magnetic field variations, and generate a more uniform signal intensity across the image. Adiabatic pulse sequences are designed to maintain the magnetization of the tissue being imaged, regardless of variations in the local magnetic field. These pulses are often used in challenging imaging scenarios, such as imaging near metal implants [151], where conventional RF pulses can lead to image distortions, signal loss and excessive heating. Moreover, designing pulse sequences that allow for shorter repetition times can reduce B_1 artifacts and enhance image quality.

RF shim coils are another effective method for counteracting B1 artifacts. Positioned on the patient's body, these coils act as regulators for the B_1 magnetic field, minimizing any variances and producing a more uniform signal intensity. Despite the difficulties in applying this technique to higher fields, recent designs demonstrate significant promise by providing great homogeneity and operating within prescribed SAR guidelines [152].

Moreover, multi-channel RF coils offer an excellent solution for B_1 field homogeneity by enabling a more precise control of the RF field. At higher fields, Larmor frequencies create shorter wavelengths and introduce interference effects that can impair field homogeneity. Multi-channel RF coils provide precise field control and are particularly advantageous at higher fields [153].

Advanced image reconstruction techniques, such as B_1 mapping [154, 155], are useful for correcting B_1 artifacts during post-processing. These methods measure the B1 magnetic field and enable compensation for any signal intensity variations across the image. TrueForm technology [156], by modulating the excitation phase in order to create more

homogeneous excitations in large imaging volumes [63], provides a correction for this issue.

Finally, careful subject positioning within the MRI scanner is another practical method to reduce B_1 artifacts [157]. By adjusting the subject's position within the scanner, it is possible to minimize B_1 magnetic field variations and improve image quality.

3.1.6 B_0 Inhomogeneity-related Distortions

The main magnetic field, B_0, is subject to variations that can cause image artifacts and distortion (Sections 2.4.1 and 2.7.1). However, a number of techniques exist to surmount these obstacles and improve image quality.

One promising approach to managing B_0 inhomogeneity-related distortions is the use of specialized shimming techniques. The concept of shimming is rooted in adjusting the inhomogeneity of the magnetic field by introducing small magnetic fields to counteract variations in the main magnetic field (through the use of special shim coils into the magnet system), as well as by varying the amount of electric current passing through the shim coils that make up the room-temperature shim set [158, 10]. Hardware-based shimming is one approach, for example, with passive shimming using magnetic shim plates, whereas software-based shimming is another, utilizing dynamic shim updating with real-time feedback (Section 2.7.1).

Altering the pulse sequence, as well as their individual specifications, can be used to manage distortions related to B_0 inhomogeneity. In particular, imaging techniques utilizing gradient echoes (such as Echo Planar Imaging) and other applications with limited bandwidths are particularly vulnerable to B_0 imperfections [159], thus their use is restricted at higher fields. Advanced parallel imaging methods, such as sensitivity encoding [160], can also be used to reduce the effect of distortions caused by B_0 inhomogeneity on the quality of images.

It has been observed that B_0 field inhomogeneities seem to shift when the polarity of the readout gradient is reserved, whereas gradient distortions stay constant. This implies that the distortion caused by Gradient Non-Linearity (GNL) can be isolated by calculating the average distortion of two scans with reversed polarity [57]. Although many MRI scanners allow polarity switching through the clinical interface, certain scanners may require access to research or service mode to enable this functionality.

In addition, post-processing methods for correcting distortion associated with B_0 inhomogeneity can be used. Such methods may require additional image data acquisition using different encoding directions. Various techniques presently available or under investigation for distortion correction are presented in Section 3.5.

3.2 Advantages and Disadvantages of FSPGR

IPO-Porto has made the informed decision to use the FSPGR sequence for brain imaging in SRS treatment planning due to its specific advantages in this context. Specifically, the high spatial resolution of FSPGR allows for precise localization and delineation of small target volumes, such as brain tumors, facilitating accurate treatment planning. The short acquisition time of FSPGR is particularly beneficial for SRS patients, minimizing the potential for motion artifacts and ensuring efficient treatment delivery. The superior contrast and multiplanar capability further contribute to confident target volume identification and evaluation. While FSPGR does have certain limitations, the benefits it offers align well with the requirements of SRS treatment planning at IPO-Porto. It has been shown to perform well compared to its alternatives [161] and is commonly used, having been included in standard brain imaging protocols [162]. This is very advantageous, as it provides numerous benchmarks and standardized documents for IPO-Porto to compare its performance with, as well as for optimization procedures.

While FSPGR is a suitable choice for brain imaging in SRS treatment planning, alternative MRI sequences can also perform effectively. One such sequence type are 3D-turbo-SE sequences, such as T_1-SPACE [74, 91], which provides excellent intracranial volume delineation. Some studies suggest that, in this regard, the T_1-SPACE sequence is superior to the FSPGR [163, 164]. However, it provides less contrast between grey and white matter [161] and it has a longer imaging time, being a SE sequence.

Additionally, the Fluid-Attenuated Inversion Recovery (FLAIR) sequence can aid in the detection and delineation of lesions with high sensitivity [14]. Its application in SRS has been the subject of various studies [165, 166] and it is used in some institutions [167, 74]. The main advantage of this sequence is the possibility of CSF suppression, which can help localize and identify smaller lesions that could be obscured by CSF in other sequences [168]. However, the contrast between white and grey matter is poor, and it has a longer imaging time than FSPGR, mainly due to longer TE [169].

A quick note on clinical workflow and vendor-hospital communication is now merited, as these factors are also important in the final sequence choice and clinical implementation methods. Indeed, regarding SRS planning, it should be observed that brands such as GE and others do not seem to be overly concerned with geometric distortion. This can be attributed to the fact that they primarily sell scanners for Radiology, specifically for diagnostic purposes. In the context of diagnosis, a certain degree of distortion is considered inconsequential, as the parameters of interest are SNR and CNR. Consequently, it becomes the responsibility of the hospital staff, utilizing appropriate phantoms, to measure the distortions. Often, the only guarantee of the manufacturer is that this sequence is suitable for brain imaging, without specifically mentioning SRS or other specific applications that might need further optimization. The decision to adopt this sequence for planning purposes is then usually made by the physicians at the hospital, based solely on its suitability for brain imaging. Consequently, it becomes the responsibility of the Medical Physics staff to measure the distortions, using appropriate phantoms.

3.3 GE Signa Scanner

Since the distortion profiles and their correction depend on the scanner, this Section presents an overview of the used scanner, the GE Signa 3.0T HDxt, highlighting its inherent tools that contribute to the reduction of geometric distortion.

One key attribute of this scanner is its high gradient amplitude of 50 mT/m. This gradient amplitude enables the acquisition of images with lower TE values, resulting in faster imaging and reduced motion artifacts. Faster imaging is particularly important for institutions with high patient loads, as is the case of IPO-Porto. High gradient strengths not only reduce motion artifacts, but also provide better spatial resolution, which is particularly advantageous for SRS treatment planning, where precise visualization of anatomical structures is of utmost importance.

Although it has been observed that the GE Signa 3.0T HDxt scanner may generate slightly more heat compared to equivalent Philips models [170], this thermal effect does not pose a significant concern, even for magnetic dental attachments, which are the most common type of medical implant. Thus, clinicians can confidently employ this scanner without compromising patient safety or the integrity of dental implants such as orthodontic braces. However, these can still cause metallic artifacts, as was explained in Section 2.6, and the scanner does not offer any method specifically tailored to reduce this problem.

It is worth noting that the GE Signa 3.0T HDxt scanner has been reported to exhibit higher distortion levels when compared to the Signa HDxt 1.5T model [171]. This is to be expected since, as mentioned in Section 2.5 this is the main disadvantage of using higher magnetic field strengths, and it increases the importance of applying distortion correction techniques, either in post-processing or during sequence optimization and protocol definition.

This scanner uses parallel-imaging acceleration techniques. These techniques expedite the imaging process, thereby reducing overall scan time. Moreover, parallel imaging techniques aid in compensating for susceptibility artifacts, a crucial factor to consider for FSPGR sequences utilized in SRS treatment planning.

Electromagnetic interference reduction is a critical feature of the GE Signa 3.0T HDxt scanner, with a reduction rate of 99%. This reduction minimizes the impact of external electromagnetic sources on image quality, ensuring reliable and precise imaging results. In particular, it minimizes any effects of the eddy currents mentioned in Section 2.7.1, which could cause significant susceptibility artifacts and lower the SNR of the images.

The scanner allows for a minimum slice thickness of 0.5 mm in a 2D acquisition, offering exceptional spatial resolution. This capability is particularly valuable for SRS treatment planning. It also allows the testing of the effect of compensating lower slice thicknesses by using lower bandwidths (Section 4.4).

Finally, the GE Signa 3.0T HDxt scanner demonstrates very good long-term stability, with a rate of less than 0.1 ppm per hour of continued operation, sustained for up to 24 hours. This stability ensures consistent performance and reliable image quality during prolonged scanning sessions, reinforcing the scanner's suitability for SRS treatment planning. This is important in the particular case of IPO-Porto, given its long operating hours and high patient load.

A final note should be presented regarding direct methods for distortion and artifacts correction. GE (and other vendors) mention them in their brochures and websites, but no concrete information is presented, and in some cases, such as for this scanner, not even the full technical sheet is publicly available. Although the justification for this is probably tied to economical and competitive reasons, the lack of information regarding many of the hardware components in this and other MRI scanners hinders the numerous studies which could benefit from this information.

This lack of transparency from vendors and MRI centers has actually been the object of various studies, such as Karakuzu et al [172], who mentioned that this hinders the reproducibility of the published developed techniques and presents a roadblock in the deployment of standardized sequences. Unfortunately, this is not the only case where business-related interests interfere with scientific progress in the field of MRI, as vendor-specific naming conventions, for example, also pose a problem in cross-comparison studies and those who use automatic multi-vendor data extraction [173].

3.4 Phantoms for Measurement of Geometric Distortion in MRI

Phantoms are indispensable both in assessing the performance of MRI and in measuring its geometric distortion. Recent years have witnessed remarkable progress in phantom development and application, particularly for the latter purpose.

The fundamental concept behind the design of geometric phantoms for measuring geometric distortion in MRI is elegantly simple. Geometric phantoms typically incorporate a set of reference points, or features, that are easily identifiable in MR images. For convenience, the position of these reference points, or "control points", are known and defined by the phantom's geometry. This correspondence allows for the measurement of geometric distortion in the distorted MR image against a CT scan of the phantom or against another reference image [85]. Notably, some of the developed phantoms define control points only in 2 dimensions, distinguishing them as 2D phantoms, in contrast to those with control points defined fully in 3 dimensions, aptly termed 3D phantoms.

The grid phantom is one of the most prevalent phantoms for measuring geometric distortion in MRI [84]. It consists of a grid pattern of intersecting lines or tubes that serves as a known spatial reference for measuring geometric distortion. Each intersection between the mesh lines can be considered a reference point, allowing for reproducible geometric distortion tests. Grid phantoms are cost-effective and easy to produce [they can even be 3D printed, such as in Jafar et al. 174], making them a popular choice for assessing distortion in MRI.

Spherical phantoms are also commonly used for measuring geometric distortion in MRI. They are made up of one or more spherical objects that provide a known spatial reference for the measurement of geometric distortion [e.g., 175]. These phantoms are highly reproducible and can evaluate the distortion in MRI images over a range of spatial frequencies, as well as minimizing the phantom interaction with the magnetic field, as can

happen in sharp corners [113]. A tissue-equivalent spherical phantom (MATROSHKA-R) was used to study the characteristics of space radiation in the ISS [176, 177]. Its shape makes spherical phantoms particularly suitable for radial distribution studies, such as the aforementioned ones. However, grid phantoms are also capable of providing radial distribution data, while often being easier to stabilize during imaging and to manufacture.

Anthropomorphic phantoms have recently garnered increased attention for the measurement of geometric distortion in MRI. These phantoms replicate the geometry and properties of human tissues and organs, resulting in a more precise and realistic representation of the MRI environment [e.g., 178]. Anthropomorphic phantoms can be tailored to evaluate the performance of MRI systems for specific applications, such as brain [179, 180] or breast imaging [181, 182, 183], and can be created using various materials, including polymers, gels, and plastics.

The thickness of the walls in phantoms holds a significant place in the design considerations. Interfaces between air and phantom walls can cause susceptibility-induced distortions in the magnetic field. To mitigate these errors, one can increase the thickness of the walls, which in turn increases the distance between the air/phantom wall interface and the volume producing MR signal [113]. This approach can effectively minimize susceptibility-induced errors and enhance the accuracy of magnetic resonance measurements. To reduce the influence of slice curvature, the phantom is also recommended to be at least twice as thick as the slice thickness utilized in the measurement [184].

The progress in the measurement of geometric distortion in MRI has been partly due to new phantom designs, but the development of advanced imaging and analysis techniques has also contributed significantly. The incorporation of these techniques, described in Sections 3.1 and 3.5, in tests done with new phantoms, has resulted in more precise quantifications of distortions present in MRI images. Other techniques, such as the use of fiducial markers or magnetic field probes, can measure the magnetic field gradient in the MRI scanner, thus also enhancing the accuracy of geometric distortion measurements.

The phantoms used in medical imaging tests can have various characteristics, according to their purpose and design priorities. The dimensional parameters of the phantom and its grids are particularly dependant on the desired studies in which it will be used. An overview of the characteristics of commercial phantoms that can be used to measure MRI distortion is presented in Table A.1. A 3D printed design proposed by [185] is also

included, since this type of design, due to its ease of construction and cost efficiency, may become the standard in the future.

As for the shape, it can be seen that most of the phantoms shown are cylindrical, with two exceptions (the GRID 3D Quasar is cubic, and the CIRS MRI Head is anthropomorphic). Compared to the other two major design types presented in this Section (anthropomorphic and sphere), the cylinder has the advantage of being both easy to fabricate, unlike the former, and being easy to insert in the gantry for imaging, unlike the latter. Moreover, they are useful for minimizing phantom induced field distortions [113], and the fact that cylindrical phantoms have a uniform thickness along its entire length is important for calibration and quality assurance. In the case of geometric distortion studies, it ensures that each plane can have the same number of reference points. Anthropomorphic phantoms, such as the 603-GS, are more expensive and harder to build, given their complexity, but they provide unique advantages. The fact that their shape is similar to that of a patient allows, for example, studies of high distortion areas deriving from patient anatomy, such as air-cavities in the sinuses and eyes [186].

It can also be inferred from Table A.1 that the most common material used in phantoms is acrylic, which is justified by its unique properties and advantages. Firstly, acrylic is biocompatible and non-toxic, ensuring its safety in medical applications without causing any adverse effects or tissue reactions [187].

Furthermore, acrylic is radiologically transparent, meaning it does not significantly attenuate X-rays or other imaging modalities. This characteristic makes acrylic an optimal choice for building phantoms as it does not introduce any additional artifacts or distortions into the images, ensuring accurate and reliable results. In addition to its radiological transparency, acrylic is known for its durability and longevity. It is resistant to wear and tear, making it suitable for repeated use, cleaning, and sterilization. This durability ensures that acrylic-based phantoms can withstand rigorous and prolonged usage, maintaining their integrity and functionality over an extended period.

Moreover, acrylic is easy to shape, allowing for precise customization of phantom geometries. It can be cut, drilled, and molded into complex shapes, making it convenient for building phantoms with specific designs or configurations to meet diverse imaging requirements. Lastly, the cost-effectiveness of acrylic makes it a viable option for constructing phantoms. Compared to other materials such as metals, acrylic is relatively

low-cost, making it a cost-efficient choice for building phantoms without compromising on quality and performance.

3.4.1 Phantom Fillings

The use of liquid-filled phantoms in medical imaging is motivated by the need to replicate the characteristics of human tissues regarding the specific imaging mechanism. Human tissues are predominantly composed of water, making liquid-filled phantoms the preferred choice in mimicking tissue characteristics. Additionally, just like air, liquids conform to the shape of their containers, making them easy to shape, even in geometrically complex phantoms.

In addition, the stable density of liquids makes them ideal for phantoms used in quality assurance and calibration procedures. The density of liquids remains consistent over time, allowing for precise control and monitoring of phantom density during calibration and quality assurance processes, ensuring accuracy and reliability.

3.5 Distortion Correction Methods

Geometric distortion correction in MRI is a crucial step in obtaining accurate and reliable images, particularly in clinical applications such as SRS and functional MRI. Methods for correcting magnetic susceptibility and B_1 artifacts, as well as B_0 inhomogeneity-related distortions at 3T, were presented in Section 3.1. This Section is thus dedicated to covering the remaining topics regarding the state of art of distortion correction methods, in a more general manner.

The current state of the art involves the use of various techniques to mitigate image distortions caused by magnetic field inhomogeneities [e.g., 23, 188]. A common approach is image registration, which uses mathematical algorithms to align the distorted image with a reference image acquired with a correction technique or a different pulse sequence. However, the efficacy of these algorithms can exhibit variability dependent on the specific image under consideration. This observation implies that the universal adoption of a non-adaptive algorithm for all image types may not be prudent, particularly in scenarios necessitating utmost precision, as exemplified in SRS [23]. To elaborate on this point, let us denote the positions of control points, as determined by the phantom's geometry, using the Cartesian coordinates (x, y, z), while the primed coordinates (x', y', z') symbolize their

corresponding locations within the distorted image space [85]. With these representations, the comprehensive characterization of geometric distortion can be succinctly conveyed through the following correspondence:

$$\begin{pmatrix} x \longleftrightarrow x' \\ y \longleftrightarrow y' \\ z \longleftrightarrow z' \end{pmatrix} \tag{3.1}$$

Thus, the geometric distortion within the effective volume of the phantom can be fully characterized by positional deviations along the three orthogonal axes at the control points present in the phantom, by analysing the differences:

$$dr'_{i,j,k} = r_{i,j,k} - r'_{i,j,k} \tag{3.2}$$

This way, the undistorted image space can be recovered from the distorted image space by adding to it the geometric distortion correction factors at each control point, and using an interpolation method for the remaining points, as suggested by Wang & Doddrell [85]. They continue by expanding this concept to global mapping functions, which provide a complete 3D correction via functions of the form $x' = f_x(x, y, z)$ for each of the distorted image space coordinates. However, as pointed out in that study, the use of global functions in the modeling of geometric distortions in MRI brings about some drawbacks. Among them the issue of identifying the ideal terms that should be included in a particular modeling problem. Incorporating higher-order terms may result in a more accurate fit to the source data, yet it does not always provide the best modeling solution, and may introduce overfitted models. Moreover, global functions sometimes lack "spatial flexibility", making it difficult to satisfactorily model local features.

Regarding other ways to quantify geometric distortion, Liu et al. [81] used the Euclidean distance formula to quantify their 3D distortion values, which could then be optimized by its minimization:

$$Distortion = \sqrt{(x - x')^2 + (y - y')^2 + (z - z')^2} \tag{3.3}$$

Another approach for geometric distortion correction is the use of field maps [10], which provide information about the magnetic field inhomogeneities in the imaging volume and can be used to correct distortions in the images. Field maps can be acquired

using different pulse sequences, and the choice of pulse sequence is typically guided by the specific imaging application and desired correction accuracy [188].

The correction of 3D GNL distortion provided by vendors is the bare minimum that should be applied, according to Paulson et al. [108]. A detailed analysis of vendor-supplied correction algorithms in some clinical MR systems can be found in Wang et al. [189]. However, it is important to note that despite these corrections, residual distortions on the order of several millimeters may persist. Thus, it is crucial to characterize them independently, without relying solely on vendor-provided methods, which have some limitations and may only account for first-order nonlinearity of the gradients [85, 10]. In some cases, additional corrections utilizing 3D deformation vector fields may be necessary, especially for large FOV images [190]. Alternatively, innovative techniques such as the "step-and-shoot" approach [191] or acquisition during continuous table movement [192] have been proposed as potential methods to reduce these distortions. In "step-and-shoot" techniques, the MRI scanner acquires individual slices of the body one at a time, with a pause or "step" between each slice. The patient remains still during the acquisition of each slice, and the table does not move during image acquisition. On the other hand, with continuous table movement acquisition, the MRI scanner acquires images while the patient continuously moves through the scanner bore on the table. The table moves at a constant velocity, and images are acquired continuously without any pauses or steps.

Deep learning algorithms have also displayed encouraging potential in enhancing the precision and resilience of geometric distortion correction, particularly in complex imaging scenarios where conventional techniques often fall short, using convolutional neural networks (CNN). A key advantage of these algorithms lies in their adaptability, enabling their application across various image types. This adaptability effectively addresses the limitations of non-adaptive algorithms, which often exhibit inconsistent performance. Recent breakthroughs involve the use of new CNN architectures to dynamically predict B_0 inhomogeneities generated by patient motion [77]. However, ongoing research in this area still aims to develop more accurate, robust, and efficient correction methods [193].

It is worth noting that, although MRI scanners are equipped with algorithms designed to correct hardware-related distortions, residual geometric distortion generally remains [112, 4]. As mentioned before, the magnitude of geometric distortion is influenced by various factors, such as MRI machine brand, magnetic field strength, gradient type, pulse sequences, and patient scanning parameters [194, 186].

Recent studies have demonstrated that the issues of static field inhomogeneity, magnetic susceptibility, and chemical shift distortions can be mitigated by alternative methods based on the amplification of the gradient field strength, such as by increasing the readout bandwidth [195]. A commonly followed guideline to mitigate distortions is to set the readout bandwidth to twice the fat-water shift, such as 440 Hz at 1.5 T and 880 Hz at 3 T [196]. Despite its effectiveness in mitigating distortions, this approach also results in a minimum reduction of 30% in SNR. Thus, many radiology departments opt for lower bandwidths in order to minimize imaging time while preserving a favorable SNR. However, when it comes to MRI for radiotherapy planning, a divergent approach is warranted. In this context, higher bandwidths are preferred to mitigate the adverse effects of B0 inhomogeneities on image distortions [74]. Notably, it has been observed that gradient nonlinearity errors are not influenced by the gradient strength and remain independent of its magnitude [10, 57].

Glide-Hurst et al. [57] also present an equation to obtain the readout bandwidth required to reduce geometric distortion to permissible ranges, given a permissible shift along the readout direction, that depends on the imaging workflow and type of treatment (for SRS, for example, a maximum shift of 1 mm is deemed acceptable [74]):

$$Bandwidth\left(\frac{Hz}{pixel}\right) = \frac{Max\Delta B_0(ppm) * f_0(MHz) * FOV(mm)}{Shift(mm) * MatrixSize(pixel)} \tag{3.4}$$

where f_0 is the system frequency, and the FOV and matrix size govern the spatial coverage and resolution of the image. This method of tailoring the readout bandwidth setting for a specific scanning protocol, field strength, and body region, while mitigating excessive loss in SNR, has been shown to be effective. It is important to note, however, that the upper limit on readout bandwidth may be constrained by the gradient system available on the scanner (which limits the first term of the numerator). Likewise, the lower limit on readout bandwidth should be carefully determined to minimize chemical shift, such as water-fat shift, to less than 1 pixel for a given field strength (e.g., 220 Hz at 1.5 T and 440 Hz at 3 T).

Once the readout bandwidth has been optimized for a specific disease site, several strategies were proposed by Glide-Hurst et al. [57] to recover any lost SNR. One approach is to increase the number of averages or excitations. However, increasing the number of averages by N will result in an increase in acquisition time by a factor of N,

but the improvement in SNR will only be proportional to the square root of N. Alternative approaches may include switching to 3D acquisitions and utilizing phase and slice oversampling, although these strategies may also result in increased scan times. Careful consideration of these strategies is warranted to strike a balance between SNR recovery and scan time, depending on the specific imaging requirements and constraints of the study.

Experimental data shows that the distortion is least at the center of the scan volume and gradually increases toward the radial borders [81, 197, 4]. Even for head scans with a small field of view, the maximum distortion can reach 3 mm [198, 57]. Therefore, the development of more effective correction methods remains a high priority in the MRI research community to ensure accurate and reliable MRI image quantification.

Indeed, even studies using comprehensive parameter optimization along with geometric distortion correction methods may yield only slight improvements. Taghizadeh et al. [91] had MR images with deviations between 0.4 mm and 1.2 mm before correction, compared to CT images used for SRS coordinate definition. After geometrical correction, they observed a maximum deviation of 1.1 mm and minimum deviation of only 0.3 mm. Although the initial deviations were already relatively small, the improvements only improved the maximum and minimum deviations by 0.1 mm.

On the other hand, there are examples of studies that utilized correction methods to great effect. The group at German Cancer Research Center in Heidelberg in 1992 [7] or 1994 [199] are historical examples. The latter used a stereotactic localization frame during MR imaging and irradiation. Afterwards, system-dependent distortion correction methods reduced the error in the position of the stereotactic frame coordinates from about 2-3 mm to 1 mm, which was the lower distortion limit, given the pixel size. The group didn't use patient-dependent correction methods, choosing instead to minimize the impact of this type of distortion by appropriately choosing the imaging parameters.

Chapter 4

Materials and Methods

4.1 Phantom Filling Solution Tests

The choice of filling material for geometric phantoms is a critical factor that can significantly impact the accuracy and reliability of MRI geometric distortion studies. In this Section, the tests performed to determine the optimal filling material for the geometric phantom will be explained.

To begin our study, we carefully selected four candidate materials for testing: mineral oil, gadolinium, copper sulfate, and nickel chloride. These materials were chosen based on their properties, including their magnetic characteristics, toxicity, and potential similarity to contrast agents used in patients. Gadolinium has already been presented in Sections 2.2.4 and 4.2, and it is a rare earth metal whose high magnetic moment makes it interact strongly with magnetic fields, as desired. Gadoteric acid, the substance used in this study, has been deemed safe to use in patients. In particular, the gadolinium contrast solution used in IPO-Porto is Dotarem®, which has been extensively researched regarding safety and efficacy in humans [e.g., 200, 201].

Mineral oil is a clear, odorless, and non-toxic liquid whose relevance stems from the fact that it has similar physical properties to human tissue (particularly its T_1 and T_2 times). It is usually a mixture of diverse hydrocarbons, drawn forth from unprocessed petroleum by means of refining methodologies. The precise configuration can exhibit deviations contingent on the origin and deliberate application of the mineral oil [202]. Moreover, mineral oil is non-reactive and allows plastics to remain dimensionally stable over time unlike water, for example, which causes plastics to swell. Its dielectric constant

is much lower than water, mitigating the effect of dielectric resonance and its related artifacts. Mineral oil is also economical and has shown promising results in previous tests done by the Medical Physics staff at IPO-Porto (private communication).

As for copper sulfate and nickel chloride, they are blue and green-coloured salts, respectively, which have magnetic and metallic properties that can be used to purposefully create susceptibility differences and image distortion. Copper sulfate has been used in many studies, such as Bettiol et al. [203], Keenan et al. [204] and Thangavel et al. [205], each with a slightly different concentration and solution mix, as well as in the commercial Maghpan phantoms, whose 820 model was presented in Section 3.4. Nickel chloride is used in the ACR MRI phantoms, also mentioned in Section 3.4.

A brief note regarding safety measures is merited. Indeed, the MR environment presents unique risks to both patients and staff, and there have been instances of injuries and even deaths as a result, although these are very rare [206]. Therefore, MR experiments require careful consideration of safety measures to protect everyone involved [57]. Thus, throughout this and every step in the study, strict safety protocols were followed, according to IPO-Porto's internal protocols (e.g., exclusion of all ferrous objects from Zone IV), and AAPM Report 20 [207].

4.1.1 Preliminary Study in Anthropomorphic Phantom

We conducted a series of CT and MRI scans on the "RANDO" male anthropomorphic phantom (Figure 4.1) using the four candidate materials for the filling of the geometric phantom. This phantom contains a human skull, which provides the bone asymmetry normally found in patients, molded in tissue-equivalent material [208]. The phantom is cut in 2.5 cm cross sectional slices [209]. The internal volume of each acrylic insert is 0.103 ml [210]. The phantom was positioned in a manner that mimicked a typical clinical MRI setup, and imaging was performed using a standard clinical MRI protocol (Section 4.4). The phantom has been shown to be compatible with MRI imaging in previous studies conducted at IPO-Porto [210].

For this first test, the 2nd and 3rd slices of the phantom from the top were chosen, and 20 inserts (5 of each solution) were distributed as shown in Figure 4.2, with 10 inserts in each of the slices.

The distribution was chosen in order to guarantee that each of the tested filling substances had equivalent testing conditions, in order for direct comparisons to be drawn.

FIGURE 4.1: "RANDO" head phantom used in this study.

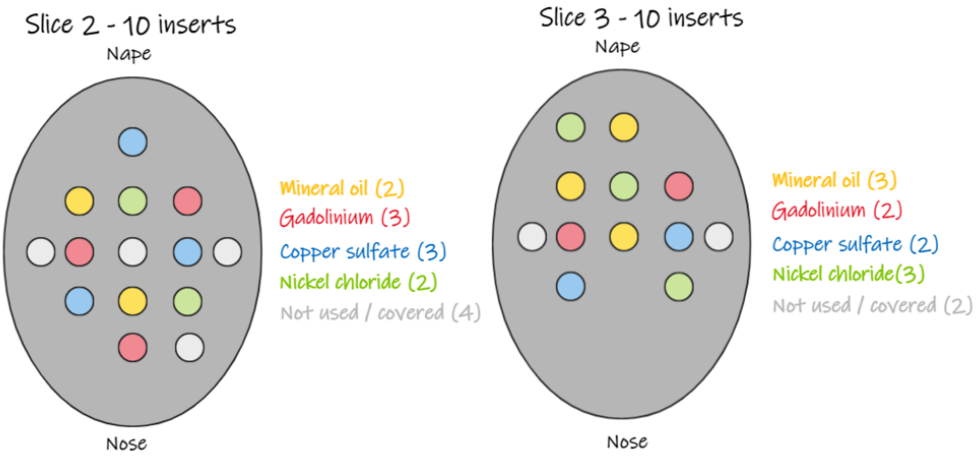

FIGURE 4.2: Distribution of the inserts in the tested "RANDO" head phantom.

This means, specifically, that each substance has 3 inserts in one of the slices and 2 in the other, and that their radial positions are as balanced as possible, with matching overlaps when possible, to minimize any potential interference.

TABLE 4.1: Concentration of Solutions (mmol/L). The solutions were diluted in 0.9% saline solution. The mineral oil (brand "Radex", exact chemical composition not available) was not diluted.

Solution	**Concentration (mmol/L)**
Copper Sulfate	4.26
Gadolinium	1
Nickel chloride	10

The resulting images were carefully analysed to assess the geometric distortions induced by each filling material, by comparing the MRI images with the corresponding CT

ones, which were considered to be the ground truth. This comparison involved a registration process that is detailed in Figure 4.3 and which will be explained below.

FIGURE 4.3: Registration process for MRI coordinates in the "RANDO" phantom tests.

After extracting the MRI and CT coordinates from the slice being studied (Figures A.1 and A.2), the first registration step was a translational one, using the values given by the software used in IPO-Porto for registration and radiotherapy treatment planning, Eclipse (Varian Medical Systems). The new coordinates (x_n,y_n,z_n) were given as a function of the translation values given by the software (x_{tr},y_{tr},z_{tr}) by:

$$\begin{bmatrix} x_n \\ y_n \\ z_n \\ 1 \end{bmatrix} = \begin{bmatrix} 1 & 0 & 0 & x_{tr} \\ 0 & 1 & 0 & y_{tr} \\ 0 & 0 & 1 & z_{tr} \\ 0 & 0 & 0 & 1 \end{bmatrix} \begin{bmatrix} x \\ y \\ z \\ 1 \end{bmatrix} \longleftrightarrow \begin{cases} x_n = x + x_{tr} \\ y_n = y + y_{tr} \\ z_n = z + z_{tr} \end{cases} \tag{4.1}$$

The second step was to add the rotational registration of the same software for x and y, with angles θ_1 and θ_2, respectively. The rotation in z was considered to be negligible ($\approx 0.1°$). Thus, the new coordinates were given by applying rotational matrices, so that $\vec{r}' = R_y(\theta_2)R_x(\theta_1)\vec{r}$, or written in full:

$$\begin{bmatrix} x' \\ y' \\ z' \end{bmatrix} = \begin{bmatrix} cos(\theta_2) & 0 & -sin(\theta_2) \\ 0 & 1 & 0 \\ sin(\theta_2) & 0 & cos(\theta_2) \end{bmatrix} \begin{bmatrix} 1 & 0 & 0 \\ 0 & cos(\theta_1) & sin(\theta_1) \\ 0 & -sin(\theta_1) & cos(\theta_1) \end{bmatrix} \begin{bmatrix} x_n \\ y_n \\ z_n \end{bmatrix} \tag{4.2}$$

The final step consisted of a final transformation to ensure that the MRI and CT coordinates were in the same reference system, to allow for direct comparisons. This was done

by measuring the coordinates of the central insert and matching them. Thus, the differences yielded the total distortions for each insert, given by $\sqrt{(x_{CT} - x_{MRI})^2 + (y_{CT} - y_{MRI})^2}$. The results of this test are presented in Section 5.1.1. Based on our comprehensive analysis of the experimental results, we concluded that gadolinium was the optimal filling material for our geometric phantom. Despite its significant distortion characteristics, it provided valuable insights into the effects of the filling material on MRI geometric distortions. Moreover, its similarity to patient contrasts and relatively low toxicity profile made it a suitable choice for our research purposes.

4.1.2 Optimal Solution Concentration Tests

After the tests performed on the anthropomorphic phantom RANDO, an additional test was performed to determine the best solution and concentration for the phantom filling. Thus, we studied the effects of the gadolinium concentration on MRI average pixel intensity and on CT Hounsfield Units (HU). The latter is defined as:

$$HU = \left(\frac{\mu_{material} - \mu_{water}}{\mu_{water}} \right) \times 1000, \tag{4.3}$$

where μ is the CT linear attenuation coefficient. Therefore, at standard pressure and temperature conditions, water has a value of 0 HU, while air has -1000 HU, due to its null attenuation coefficient value.

The motivation behind this investigation lies in the fact that exceedingly high Gd concentrations may not be discernible in MRI images, whereas overly low concentrations may not be distinguishable in CT scans, particularly when compared to acrylic materials (with approximately 92 HU). This issue was previously discussed in Kim et al. [211], which also served as inspiration for employing a 10% Gd concentration in saline solution. However, this concentration has proven to be costly and not compatible with real clinical scenarios, where Gd concentrations are typically lower. Furthermore, MRI signals for water and healthy biological tissues exhibit signal intensities ranging from approximately 2400 to 4000, whereas metastases (marked with Gd) display variable signal intensities, which generally hover around 8000. These pixel intensity units are the ones defined and measured in the image processing software *ImageJ*, obtained by summing the gray values of all pixels in the selection area, divided by the number of pixels [212]. Therefore, it was

imperative to establish a concentration of Gd with a signal intensity closely resembling that observed in actual patients.

Additionally, we wanted to study the effect of using the blue colourant FCF. It was selected to make the visualization of the phantom fillings easier, especially in order to confirm which inserts of the geometric phantom were filled. Therefore, the use of blue colourant was helpful both during the filling process and, afterwards, to assess potential changes in the liquid distribution in the phantom inserts and the presence of air bubbles.

For this test, two vertically adjacent rows of test plaques were placed in a PMMA container and submerged in water, in order to simulate physiological conditions and minimize MRI artifacts detected in a previous test made without them. The top layer was the control layer, while the colourant was added to the plaques in the bottom layer, for two different gadolinium solution concentrations, as well as for the copper sulfate concentration used in the previous test (Figure 4.4). Various gadolinium (1 mmol/L) and saline solution control points were set up on adjacent vertical plaque layers to ensure that the test result variations were solely attributed to the tested variables. The mean intensity results for each tested solution are shown in Section 5.1.2 (Figure 5.3). The solutions were prepared using an analytical balance from the Nuclear Medicine Department at IPO-Porto with a readability of up to 0.001 g.

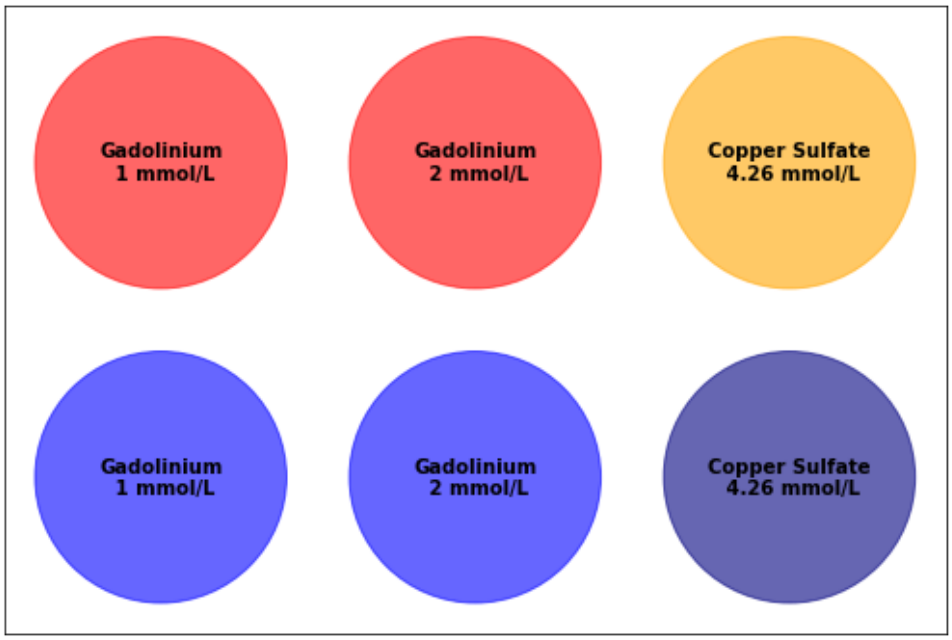

FIGURE 4.4: Experimental setup for concentration and colouring test. Upper row: solutions without colourant. Lower row: equivalent solutions with colourant.

4.2 Design of New Phantom for Geometric Distortion Measurement

In this Section, the design and construction of the geometric phantom are explained. The phantom was designed by our team, and built in the workshop of the Faculty of Sciences of the University of Porto (FCUP), under the careful supervision of a staff member, to ensure its accuracy and integrity.

The phantom was specifically designed to be used in the MRI scanner and was built around the dimensions of the the cylindrical outer part of a Jaszczak SPECT Phantom [213, 214]. This ensured that the phantom fit seamlessly into the MRI scanner, allowing for accurate and reliable imaging. IPO-Porto has a head antenna and a torso antenna with maximum diameters of, respectively, 22 and 43 cm (Figure A.3). Thus, 43 cm was the upper diameter limit of the phantom, if it was to fit the MRI scanner, and 22 cm if we wished to use the head antenna for the phantom MRI images. Given that this study is focused on SRS treatment planning, the images of interest are brain images and, therefore, the head antenna was the one used throughout the imaging tests.

The final design of the phantom grid consists of three perpendicular square grids, along with two axial grids at the top and bottom of the phantom. This comprehensive grid layout was meticulously planned to ensure that all planes of interest, both close to the isocenter and away from it, where distortion is known to be greater, could be effectively studied. This design allowed for a thorough evaluation of the MRI scanner's performance across different planes and regions, providing valuable insights into potential distortions and their impact on image quality. The frontal and superior views of one of the geometric phantom grids are presented in Figure 4.5. An overview of the phantom design and a photograph of the finalized phantom are shown in Figure 4.6.

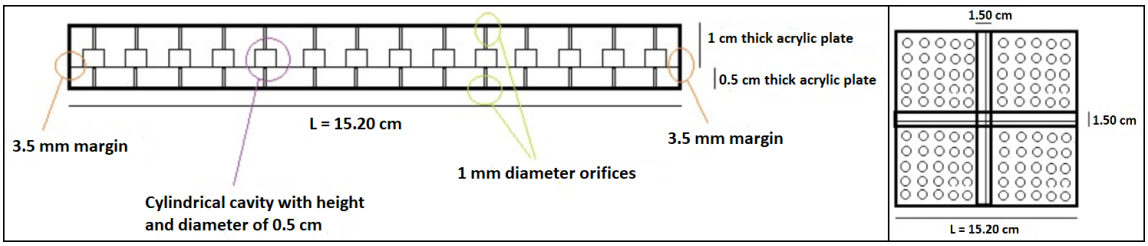

FIGURE 4.5: Frontal and superior view of one of the phantom grids.

Each grid of the phantom, after intersection with the others, can be divided into four smaller grids with 7x6 inserts, providing a total of 840 inserts throughout the phantom.

This number excludes the central row and column, which are inaccessible by design, since they are at the junction points with other grids. This central row and column for each grid could have been omitted, but keeping them facilitated the phantom fabrication process, and they could possibly be used to study the effects of air susceptibility. Further details regarding the dimensions and progress of the phantom construction and filling are present in Appendix A.2.

This configuration, with 7 rows and 6 columns in each grid quarter, was chosen to allow for a comprehensive evaluation of the MRI scanner's performance and to ensure that the phantom would be able to accurately simulate the anatomy of interest. In the design of the phantom, care was taken to ensure that the separation between air and liquid contrast media, formed by the acrylic walls and boundaries of the phantom, was more than 6 mm. This is due to the fact that, according to Modus QA [215], significant susceptibility distortions at the interface would otherwise be apparent.

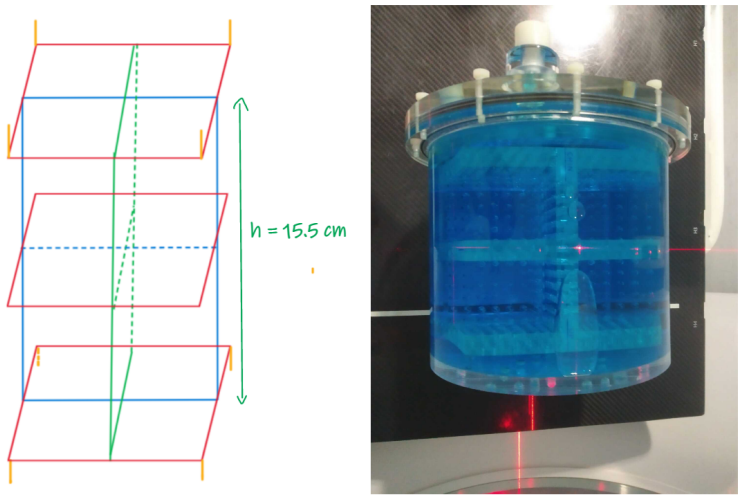

FIGURE 4.6: Phantom design overview (left) and photograph of the finalized phantom in CT imaging table (right).

To ensure the accuracy of the phantom, each insert in the grid was precisely drilled, notwithstanding the slight misalignments that always may occur during a handcrafted construction process. These misalignments were carefully accounted for during the subsequent image analysis, to ensure that they did not impede the success of the study. Despite the challenges of the construction process, the final geometric phantom adhered meticulously to the designed instructions, fitting snugly into the outer cylindrical part and accurately fulfilling its intended purpose. The phantom fitting was assured by the construction of an additional component, in the form of a sub-cover, which fits on top of the phantom and prevents it from moving inside the cylinder. Since the inserts were

numerous and small, their opening was tested in the workshop by applying sustained pressure with an air compressor. Afterwards, the phantom was leak tested in IPO-Porto laboratory using water, prior to its filling, given that a water leak would be safer and easier to clean than a filling liquid leak.

Before the first use, we ensured that no metal machining debris remained inside the phantom, as that could have caused significant errors [216]. Furthermore, utmost care was taken during the handling and transport of the phantom from the Faculty to the IPO-Porto to safeguard its integrity. The phantom was stabilized and covered in polyethylene to protect it from potential damage or contamination. Additionally, the temperature during the entire process was controlled to ensure that no significant thermal differences exceeding 5ºC existed, as thermal expansion in the acrylic material could potentially compromise the accuracy of the results. These measures were implemented to ensure that the phantom arrived at IPO in pristine condition, ready for precise and reliable imaging studies. The phantom was cleaned only with water, without using abrasives or rubbing alcohol, as these could irreversibly damage the PMMA structure of the phantom.

Moreover, proper storage of the phantom throughout the period of this study was ensured. Firstly, the phantom was stored in a temperature and humidity controlled environment, and kept away from heating elements [217], to prevent any potential degradation or distortion of the phantom.

Additional measures were implemented to safeguard the phantom from any detrimental substances, liquids, or materials that might jeopardize its constitution or modify its characteristics. Meticulous labeling and comprehensive documentation of the filling concentrations were also diligently upheld to secure the reproducibility of results, both in forthcoming investigations and in the event of a potential refilling of the phantom.

During the filling process of the phantom, we tried to fill the phantom completely to avoid introducing susceptibility artifacts caused by air bubbles. However, these could not be completely avoided while filling the inserts, since the filling process was done by displacing the air inside each individual insert and replacing it by the contrast solution using a flexible syringe. Thus, although care was taken to minimize their size and number, air bubbles did form below the intermediate axial grid after filling the lower plane inserts. When placing the phantom in the MRI scanner, these bubbles moved and formed a single air void at the top of the image plane, which facilitated the analysis factoring.

The phantom inserts were filled manually with a Gd 1 mmol/L solution. A syringe with a flexible tip was used, to allow access to the inserts closer to the axial grids, which would be impossible to fill using a normal, rigid syringe. This decision increased the number of inserts that could be filled, albeit with the presence of small air bubbles inside some inserts, whose influence was reduced by careful slice selection during image analysis. Approximately 9% of the inserts were not considered in the image analysis process due to having at least 50% of their cavity volume filled with air. The remaining 764 inserts were enough to assure the necessary precision of the results. Moreover, their random distribution did not risk their spatial distribution.

4.3 Algorithm for Automatic Geometric Distortion Calculation

One of the goals of this thesis is the development of an algorithm for automatic geometric distortion calculation. In this Section, its development process is presented. For the sake of allowing future studies to make use of the developed software, it is made publicly available*. The overall structure of the code can be divided into three parts, which are briefly presented before being analyzed in more detail afterwards.

- **Image Registration:** The registration process has been explained in the previous Section. Given the fact that Eclipse is not an open-source software, which limits the reproducibility of its results, an alternative software for registration was developed (Section 4.3.1) in order not to make this study dependent on commercial software. Given that Eclipse is fully integrated in the clinical workflow of IPO-Porto, with direct image transfer between the MRI scanner and other computers, its registration results were the ones used to obtain the final results.

- **Insert Detection:** Next, the inserts on the CT and MRI scans were separately detected after pre-processing and filtering the data so that only meaningful and accurate blobs were detected as inserts.

- **Distortion Calculation:** At this stage, after pre-processing steps related to slice thickness and resolution differences between the CT and MRI scans, as well as registration application, the geometric distortion was calculated for each matched insert centroid. The results were processed and visualization tools facilitated the interpretation of the output results.

*https://github.com/BernardoCampilho/MSc_Thesis_MRI_Distortion

4.3.1 Image Registration

The first step was the development of an image registration software in Python, which could be run from any computer.

At first, pre-existing software such as ITK-Snap [218], 3D Slicer [219] and ImageJ [220] were used for registration. However, the results showed differences from the Eclipse software that were considered significant, as they were larger than the 1 mm precision threshold. Therefore, it was necessary to develop software that could match Eclipse registry values and run on any computer.

The implemented code uses the SimpleITK library for image processing to perform registration between CT and MRI scans. The code reads DICOM images from the specified folders and converts them to a consistent data type. The optimization process consisted of testing different parameter combinations, such as the maximum number of iterations, the minimum step per iteration or the type of interpolation used. The results were then compared, namely the running time and total registration difference, to the Eclipse results, given by $\sqrt{(\Delta x)^2 + (\Delta y)^2 + (\Delta z)^2}$, where, for example, $\Delta x = x_{ITK} - x_{Eclipse}$ is the difference between the registration offset given by the different software.

Therefore, the registration process aligns the moving image (chosen to be the MRI scan) with the fixed image and outputs the transformation. Optional code for visualizing the registration result is provided. The elapsed time of the registration process is also measured. This code serves as a crucial step in aligning CT and MRI scans for further analysis.

To ease the integration of the code into the IPO-Porto workflow, the code was adapted to directly process DICOM inputs, eliminating the need for prior conversion to other image formats. It should be noted that in cases where the CT and MRI images compared had different FOVs (which is often the case in clinical settings), an additional adjustment step had to be incorporated, which matched the value of the highest FOV modality to the other one.

4.3.2 Insert Detection

The next step was the detection of blobs in the phantom images, corresponding to the circular inserts in the phantom grids (Section 4.2).

The initial step of this part of the code involves converting the DICOM images to PNG format. This conversion is necessary to facilitate further image processing and analysis.

By reading each DICOM image using the *PyDICOM* library and saving them as 16-bit grayscale PNG files, the code ensures compatibility and uniformity in subsequent operations. Additionally, the normalization of pixel values to the full range of 16-bit grayscale enhances the quality and accuracy of the converted images. Following the conversion, the PNG images undergo a series of processing steps to identify the blobs or inserts of interest. These steps are designed to extract meaningful information and filter out irrelevant image components.

Firstly, the application of Gaussian blur reduces noise. By smoothing out irregularities and suppressing fine details, this procedure also prepares the images for subsequent analysis and will decrease the number of false positive detection. Next, Otsu's thresholding method [221] is applied to obtain a binary image. This technique automatically determines an optimal threshold value based on the image histogram, effectively separating the background from the foreground and enhancing the contrast between them.

With the binary image in place, the code proceeds to extract contours corresponding to the detected inserts. Contours represent the boundaries of connected components in the image and serve as a fundamental tool for shape analysis. The contour extraction part was adapted from code developed by Dr. Bruno Mendes for tests on IPO-Porto's RANDO phantom. By identifying the contours, the code gains access to the shape and size information needed to differentiate blobs from other image features. To narrow down the selection to relevant blobs, several criteria are considered. In particular, thresholds are defined for contour area, distance from the center, and circularity, defined as:

$$Circularity = 4\pi \frac{Contour\ area}{(Perimeter)^2} \tag{4.4}$$

Knowing the dimensions of the phantom inserts (Section 4.2), the dimension thresholds can be set in order to filter out blobs caused by air bubbles, noise or partially filled inserts. As for the circularity, it is a useful filtering parameter, given that the inserts are all circular, meaning that any non-circular blob (below a certain circularity threshold, defined as 0.8) will not be relevant to this study. These thresholds provide a systematic approach to filter out unwanted contours and retain only those that are of interest. This is important because erroneously detected contours could compromise the accuracy of the central coordinates of those inserts, used to calculate the geometric distortion of the MRI scan in the next step. Given the 1 mm distortion threshold in SRS, it was thus considered preferable to detect fewer inserts and make sure that the detected ones are as accurate as possible.

Filtered contours are further assessed based on mean intensity values and an intensity threshold, which is set to be 90% of the mean intensity of each image. This additional criterion ensures that only blobs with significant intensity, namely those that did not have air bubbles for that slice, are considered. By evaluating the mean intensity within each contour using a masking technique, the code determines whether a blob meets the required intensity threshold.

The code visualizes the filtered contours by drawing them on the grayscale image (Figures 5.5 and 5.6). This visualization helps verify the accuracy of the blob detection process and provides a means of assessing the spatial distribution of the identified inserts. Furthermore, the code keeps track of the number of slices in which 15 or more inserts are detected, along with their respective slice numbers. This information is essential for quantifying the presence and distribution of inserts throughout the MRI scan series.

The same code is applied to both CT and MRI scans. However, some adjustments are made to optimize it for each imaging modality, given their unique characteristics. In particular, the CT version of the code uses a fixed threshold instead of Otsu's thresholding method. The CT code also uses different values for filtering criteria compared to the MRI code. The minimum contour area, maximum contour area, maximum distance from the center and circularity threshold are adjusted to better suit the characteristics of CT images. These changes were justified on separate parameter optimization tests yielding different optimal results for the two imaging methods. Moreover, given that the inserts are local pixel intensity minima on CT scans and maxima on the MRI ones, due to the acrylic being, respectively, white and black (Figures 5.5 and 5.6, for example), some changes were to be expected.

4.3.3 Distortion Calculation

Before comparing MRI and CT scans for distortion calculation, several pre-processing steps have to be taken in order to make sure that differences in slice thickness, FOV and pixel resolution are accounted for, as well as performing image registration. It is noteworthy that if MRI and CT images are to be compared in order to optimize MRI image quality, such as in this study, the FOV values should be the same, or at least similar. This is due to the fact that different FOV values greatly hinder the comparison process, by requiring various additional processing steps to account for the different phantom and insert sizes in the images.

- **Accounting for Slice Thickness and Image Resolution Variations**

  One significant challenge in directly comparing MRI and CT scans lies in possible differences in their slice thickness and image resolution (in mm/pixel). Using information from the DICOM scan files, these problems are preemptively addressed, to ensure the slice comparisons are correct.

  Thus, to address this issue, this first step of the distortion calculation code calculates slice thickness ratios by dividing the CT slice thickness by the MRI slice thickness. This approach ensures a consistent basis for comparing corresponding slices and mitigates potential distortions arising from differences in slice thickness.

  Next, the code incorporates pixel-to-mm conversion factors for both CT and MRI scans. These conversion factors facilitate seamless conversion between pixel units and millimeters, ensuring that distortion assessment is expressed in physical units that are easier to interpret and are not dependent on pixel resolution. Also, having the final result in mm is important in order to compare it to established thresholds, such as maximum desired distortion threshold of 1 mm for SRS.

- **Translational Registration Parameters**

  The MRI and CT scans need to be registered before their comparison. Thus, the code incorporates translation parameters, using the rigid registration output of the Eclipse software or by the code presented in Section 4.3.1. These parameters account for the necessary adjustments in the x, y directions to properly align the images.

  As for the slice alignment (z direction) in these axial scans, it uses the value from the registration software to assign a corresponding MRI slice number to each CT slice:

$$Slice_{MRI} = Slice_{CT} \times \frac{ST_{CT}}{ST_{MRI}} + \frac{z_{registration}}{ST_{MRI}}, \tag{4.5}$$

  where ST_{CT}, ST_{MRI} are the slice thickness values of the CT and MRI scans, respectively. Thus, the first term of the second member aligns the slice numbers based on the fact that the CT and MRI scans may have different thickness values, while the last term applies the registration using the software value (in mm) and converting it to a slice number registration value.

- **Matching Inserts and Adjustments**

Once the initialization and parameter setup is complete, the code proceeds to match inserts between the CT and MRI scans. This step involves iterative analysis of each MRI slice to identify corresponding CT centers, as detailed in the next step. In order to have sufficient matches in the studied slices to draw meaningful conclusions, only MRI slices with 15 or more detected inserts were considered. In cases where no CT centers are found for a particular CT slice number, the code skips that slice to ensure sufficient data for accurate comparison.

- **Comparison and Evaluation**

  The coordinates of insert centers were stored and linked to their corresponding slice numbers. The code proceeds to compare each CT center with the translated MRI centers to identify matched inserts. The comparison is performed by calculating the Euclidean distance between each pair of points, taking into account the respective pixel-to-mm conversion factors. If the minimum distance falls below a predefined threshold, the CT center is considered matched, indicating alignment between the two imaging modalities. This also ensures that the code works correctly when a different number of inserts are detected for a given corresponding slice, in the CT and MRI scans. This may happen due to different slice thicknesses or due to the two imaging modalities having different inherent contrasts.

  The maximum distortion threshold was set to 5 mm, which is the diameter of each insert, in order to filter out erroneous matches. Through this comparison and evaluation process, the code generates a distortion map that allows the visualization of the MRI scan distortion for each of the studied slices. For each slice, information about the coordinates of the matched inserts, their distortion value and distance to the isocenter is stored, to allow for retrospective analysis.

- **Visualization and Output**

  The visualization part of the code generates a distortion map that illustrates the magnitude and direction of distortion between corresponding CT and MRI slices. The MRI slice image is displayed as the background of the plot, and the distortion map is created by overlaying the matched MRI centers on the image, with different colors representing distortion magnitude. Arrows are drawn from each center to indicate the direction and magnitude of distortion.

The software outputs the insert coordinates, its distance to the isocenter, and the distortion values (in x, y and absolute value) for each matched insert, grouping the data by their MRI slice numbers. This allows for retrospective study of each tested sequence, whose results are shown in Sections 5.2 and 5.3.

4.4 Optimization of 3T MRI Image Acquisition for SRS Treatment Planning

This Section focuses on the optimization of MRI acquisition parameters through a series of experimental tests conducted with the geometric phantom. The primary objective of these tests is to identify the most suitable MRI sequences and associated parameters that would enhance image quality while minimising distortions. By systematically varying key acquisition parameters such as slice thickness, flip angle or sequence selection, for example, we aim to optimize the MRI acquisition process, particularly for SRS treatment planning. Hence, given the scope of this study, when we mention optimization of the MRI acquisition process and the resulting images, we mean a combination of higher SNR and contrast, as well as a reduction in distortion and image artifacts, if present, while keeping imaging times clinically feasible. This will be further analysed in Section 5.3.

The tests conducted at IPO's Signa HDxt 3.0T MRI scanner are shown in Table 4.2. Some of the originally planned tests weren't feasible, after consulting the MRI technologists, either due to high imaging times or hardware limitations. However, to avoid any subsequent errors or mix-up during processing of the DICOM images, the original test names were kept. Some of the tests involved manually changing the TR and TE values, which isn't possible in this scanner, as it automatically optimizes them for a given MRI sequence in terms of the other parameters. Thus, we focused on the optimization of the remaining parameters.

SEQUENCE NAME	ACQUISITION TYPE	SLICE THICKNESS (mm)	TR (ms)	TE (ms)	NEX	PIXEL BW (Hz/pixel)	BW (kHz)	MATRIX SIZE ($pixel^2$)	FLIP ANGLE (°)	PIXEL SIZE (mm^2)	FOV (cm)	RESOLUTION (pixels/mm)	OBS
PROTOCOL	3D	1	5.804	2.056	1	244.1405	62.50	256x256	12	0,9375x0,9375	24x24	1.0667	Automatic shimming
OPTIMIZED	3D	0.8	6.499	1.752	1	781.25	200.00	256x256	12	0,9375x0,9375	24x24	1.0667	
TEST 1	3D	0.6	6.868	2.604	1	162.7735	41.67	256x256	12	0,9375x0,9375	24x24	1.0667	
TEST 2	3D	1	5.804	2.056	1	244.1405	62.50	256x256	18	0,9375x0,9375	24x24	1.0667	
TEST 5	3D	1	5.804	2.056	1	244.1405	62.50	256x256	12	0,9375x0,9375	24x24	1.0667	Manual shimming
TEST 6	3D	0.6	6.136	2.376	1	244.1405	62.50	256x256	12	0,625X0,625	16X16	1.6000	
TEST 7	3D	1	5.641	1.732	2	781.25	200.00	256x256	12	0,9375x0,9375	24x24	1.0667	
TEST 10	3D	1	5.804	2.056	1	244.1405	62.50	256x256	10	0,9375x0,9375	24x24	1.0667	
TEST 12	2D	1.9	12.000	5.800	1	325.508	83.33	256x256	12	0,9375x0,9375	24x24	1.0667	Multi-echo GE seq.
TEST 13	3D	1	5.804	2.056	1	244.1405	62.50	256x256	12	0,9375x0,9375	24x24	1.0667	AP Phase

TABLE 4.2: 3T MRI image acquisition optimization tests. The gray row is the current imaging protocol used at IPO-Porto for SRS treatment planning using a FSPGR 3D sequence. Parameters in red are the tested ones, for each test.

The pixel bandwidth refers to the difference in MR frequencies between adjacent pixels [222], and was defined as:

$$Pixel\,bandwidth(Hz/pixel) = \frac{Bandwidth(Hz)}{Matrix\,size(pixel)} \tag{4.6}$$

Given the high patient load at IPO and the continuous utilization of MRI scanners, the testing window for optimization tests was limited. Consequently, a strategic approach was adopted to carefully select tests that would encompass a wide range of variables, with priority being given to testing multiple parameters, sometimes simultaneously, over exhaustive exploration of a few. This decision was made to ensure efficient use of machine time, as methodically changing each variable multiple times would require several days' worth of scanning, which may not be feasible within the constraints of the clinical schedule. Thus, the rationale behind each test is explained hereafter:

- "FSPGR 3D Optimized":

  In the first of these tests, we applied the parameters outlined by Silva et al. [210] in an optimization study also conducted at IPO-Porto, in 2022, using the "RANDO" phantom and different processing methods. We wanted to study how this optimization of the slice thickness and bandwidth would work in this study, and compare it to subsequent tests.

  The resulting image was reconstructed in a coronal orientation, which is possible for the used MRI scanner if the original acquisition type was 3D. This reconstruction was done to test its usefulness in providing additional information to help the distortion calculation. Since it can be done after the patient has left, it allows for retrospective studies, has no effect on the imaging time, and can reduce the need for repeated scans. The trade-off is that 3D acquisition takes longer than a 2D acquisition, generally.

- Test 1 – Slice Thickness and Pixel Bandwidth Evaluation:

  The aim of this test was to investigate whether reducing the slice thickness to 0.6 mm, while reducing the bandwidth to 41.67 kHz as a trade-off to keep a similar imaging time, would have positive results in terms of image quality.

  In fact, as described in Section 2.9, slice thickness plays a crucial role in determining the spatial resolution of MRI images, with thinner slices enabling the visualization of finer anatomical details. However, reducing the slice thickness typically

increases the amount of data that needs to be acquired, potentially prolonging the imaging time. To address this challenge, the bandwidth was adjusted as a trade-off to maintain a similar imaging time.

- Test 2 – Flip Angle Variation:

  In this test, we examined the effects of using a higher flip angle (18°) in the MRI sequences.

  By increasing the flip angle, we aimed to enhance the SNR, leading to improved image quality and better visualization of target structures. The higher flip angle offers increased magnetization, resulting in a stronger signal response. Moreover, elevating the flip angle can also enhance T_1 contrast, emphasizing the differences in tissue relaxation times and aiding in accurate target delineation for SRS treatment planning.

  However, higher flip angles have potential drawbacks, such as increased SAR (introduced in Section 2.5). Therefore, we carefully assessed the trade-off between the desired benefits of enhanced SNR and T_1 contrast and the potential risks associated with increased SAR, ensuring that patient safety remains a top priority in SRS treatment planning.

- Test 5 – Shimming Options:

  In this particular test, our focus was on evaluating the use of manual shimming techniques specifically tailored to the phantom volume, as opposed to applying automatic shimming across the entire FOV. By unchecking the "Automatic Shimming" option and selecting "Manual Shimming", we were able to customize the shimming parameters to specifically target the region of interest corresponding to the phantom's volume.

  The rationale behind this approach stems from the importance of achieving optimal image quality within the precise area of interest, which in this case is the phantom volume. By narrowing the focus of shimming to the specific region of the phantom, we aimed to enhance the accuracy and clarity of the acquired images.

- Test 7 – Bandwidth and Excitation Evaluation:

  This test aims to assess the trade-off between reducing distortions and potential decreases in SNR. Specifically, the focus is on evaluating the use of a bandwidth that

is as close as possible, within the hardware constraints of the scanner, to twice the fat-water shift to minimize distortions. This approach is motivated by Task Group 284 [57], who estimate that while this approach may reduce distortions, it also may result in a potential decrease in SNR, estimated to be around 30%.

To compensate for this decrease, the number of excitations can be increased. However, increasing the number of excitations leads to an increase in acquisition time. In general, this increase is proportional to the number of excitations, but this is not always the case, and is another aspect to study in this test. As for the SNR increase with the number of excitations, it generally follows its square root. Therefore, in this test, the effect of utilizing 2 excitations is evaluated as it strikes a balance between maintaining reasonable imaging time and achieving improved SNR.

- Test 10 – SPGR Sequence optimization (Claude):

  This test focused on evaluating the performance of an optimized SPGR (Spoiled Gradient Echo) sequence developed by Dr. Claude Sirlin from UCSD (University of California, San Diego). The sequence optimization was presented by Dr. Carmen Caruana in 2020 as representative of the European Federation of Organizations for Medical Physics (EFOMP). The primary objective of this test is to assess the sequence's performance and potential advantages in the context of our research.

  It should be noted that while there are differences between SPGR and FSPGR sequences, the main distinction lies in the imaging time, as FSPGR sequences are designed to provide faster imaging through the use of advanced imaging techniques such as parallel imaging. However, apart from the imaging time variation, the two sequences share several similarities in terms of their underlying principles and acquisition parameters. As a result, the optimization parameters presented in the aforementioned SPGR sequence can still hold relevance to our study, which utilizes FSPGR sequences.

  It was highlighted in the presentation that this SPGR sequence, optimized for abdominal imaging, showed promising results, particularly when utilizing a flip angle of 10°. It is important to note that sequence optimizations are typically tailored to the specific scanner, imaging goals, and other factors unique to the hospital, such as the employed coils. As a result, a direct translation of the presented optimization

parameters was not expected. Nevertheless, given the positive outcomes demonstrated in the abdominal imaging context, it is deemed worthwhile to explore the potential applicability and benefits of this optimized sequence in our SRS-focused research.

- Test 12 – Multi-echo GRE Sequence (Somayeh):

  In this test, we explore the potential relevance of the 2D acquisition multi-echo GRE sequence from Somayeh et al. [91] for SRS treatment planning optimization, specifically in the context of field map reconstruction. Although field map reconstruction was not performed in this study, the investigation holds importance from an optimization standpoint. By using the multi-echo GRE sequence, B_0 field distortions can potentially be explored and characterized, allowing for the correction of image distortions caused by magnetic field inhomogeneities.

- Test 13 – Additional Parameter Testing:

  In this test, we investigate the impact of changing the phase encoding direction to anterior-posterior (AP). By modifying this parameter while keeping other settings consistent with the protocol sequence, we aim to evaluate its potential benefits in reducing geometric distortion and artifacts in the acquired images. The main reason why brain images are usually acquired using either PA or AP phase-encoding directions is to make the distortions symmetrical between cerebral hemispheres [223], which can be useful when correcting them.

  The AP phase encoding direction is of particular interest, given that it may reduce susceptibility-induced distortions and improve anatomical delineation [224]. There is even a distortion correction method, known as *blip-up blip-down* method, that takes advantage of the fact that distortions will have opposite directions in images acquired with PA and AP phase encoding directions, which can be used to eliminate them [225]. However, as of now, this method is not clinically feasible, mainly since it would essentially double the imaging times.

For the SAR calculation, the default patient weight suggested by the American College of Radiology of 90.718 kg (200 lbs) was used [226]. The isocenter was calculated using the Eclipse software, in order to maintain a parallelism with IPO's clinical practice. The SNR was calculated in the usual way for MRI images [227], by dividing the mean pixel intensity in the signal region by the standard deviation of the background:

$$SNR = \frac{\mu_{signal}}{\sigma_{background}} \tag{4.7}$$

Here, the signal region was defined as the phantom volume, since it was the studied object. Thus, an adaptation of the developed software was made to automatically detect the phantom, and any point within it was considered signal, while any point outside of it was considered the background.

As for the CNR, it is now considered to be complementary to the SNR [228]. In fact, it is necessary for thorough analysis of image quality, since it provides a way to measure the differentiation of different tissue types [229]. An image may have minimal noise but significant image bias [230]. Thus, an image with high SNR may not allow for tissue differentiation, which is a key issue in SRS treatment planning. In the present study, the CNR is then an important indicator meant to safeguard against over-reliance on the SNR, providing additional information to ensure the validity of the interpretations regarding what the optimal sequences are.

The CNR introduces an additional factor by subtracting the mean pixel intensity of region of interest within the signal region. In this case, it was defined as:

$$CNR = \frac{|\mu_{signal} - \mu_{ROI}|}{\sigma_{background}}, \tag{4.8}$$

where the signal and background regions were defined the same way as in Eq. 4.7 and the region of interest was taken to be the detected inserts for each slice. This is a meaningful metric, as the inserts were precisely what we tried to differentiate from the rest of the phantom throughout the development of the insert detection software.

In order to quantify the optimal sequence, based on these results, 2 weighting factors were introduced, since clinical feasibility depends not only on the geometric distortion values, but also on other parameters such as imaging time or SAR. If these values are deemed too high for a certain sequence, for example, it would never be clinically implementable *in vivo*. Thus, these factors are meant to be a quantitative help in interpreting the obtained results globally, weighting them in a way that keeps accuracy as a goal, but takes clinical feasibility factors into account. They were defined such that high values are optimal, and were normalized by the maximum value to facilitate interpretation, as the values themselves do not have inherent physical meaning, and their importance lies on relative comparison between the tested sequence results. The rationale behind each weighting factor is now explained:

- λ **Factor**: This factor weighs the acquisition parameters by assigning them one of three priority classes. In the first priority class are the acquisition time and the mean distortion (squared weighting). The former is essential for clinical applicability, while the latter is critical for lesion localization, as in the case of SRS treatment planning. Next are the SNR, CNR and number of detected inserts (linear weighting). The first two are important to quantify the image quality, as explained before, but, unlike the first priority class parameters, are not enough to invalidate a sequence's feasibility by themselves, except in extreme cases. As for the number of detected inserts, it provides meaningful information, as a sequence in which the inserts are hard to detect may mean that metastasis are also hard to detect, for example. In this factor, the number of detected inserts was normalized by dividing them by the total number of inserts.

  Finally, the SAR and maximum distortion are assigned to the third priority class (fractional linear weighting). The SAR is important, but it only becomes a limiting parameter at approximately 2 W/kg [231] and all SAR values were below 0.5 W/kg. Thus, its weight in Equation 4.9 is defined so that $\lambda = 0$ if SAR = 2 W/kg. Regarding the maximum distortion, while it helps to quantify the worst-case scenario, it may also represent an outlier value, so the mean distortion is more important. Its factor is defined so that λ tends to zero as the maximum distortion approaches 10 mm, which is one order of magnitude bigger than the desired threshold. Thus, the λ factor is defined as:

$$\lambda = \frac{SNR \times CNR}{(Time)^2 \times (\mu_{dist})^2} \times \left(1 - \frac{SAR}{2}\right) \times N_{inserts,norm} \times \left(2 - \frac{Max_{dist}}{5}\right) \tag{4.9}$$

- β Factor: This factor was determined using a different approach. This approach used a simpler formula that entailed multiplying all acquisition parameters together, each weighted by an integer that ranged from 1 to 10 (with division for "negative" parameters such as average distortion or acquisition time). Each one was assigned a separate weight, and the challenge was to determine seven weights that were both meaningful and yielded the desired values (i.e., ensuring that the sequence 12 was not the best, for instance, given its unrealistic imaging time). To address this, a brute force optimization algorithm from the Python library "Itertools" was utilized. This program exhaustively tested all possible combinations of integer weights within

a specified range of 1 to 10. These combinations were subject to constraints (e.g., the weight for average distortion being the largest, SAR being small, etc.). The resulting combinations that satisfied the desired criteria and exhibited meaningful weights were filtered and retained, resulting in three final candidate sets of parameter weights. These will be presented and analyzed in Section 5.3.

Chapter 5

Results and Discussion

In this Chapter, the results of the experimental tests and software development described in the previous Chapter are presented. Their discussion is focused on qualitative and quantitative analysis, keeping in mind the goals of this thesis.

5.1 Phantom filling tests

5.1.1 Preliminary Study in Anthropomorphic Phantom

Discussion: Our findings revealed that gadolinium exhibited significant distortion characteristics, making it an ideal candidate for our study (Figures 5.1 and 5.2). While distortion is typically considered undesirable in clinical MRI, for our research purposes in this test, it was actually advantageous, as it allowed us to thoroughly investigate and quantify the distortion effects induced by the filling material, as they happen with patients.

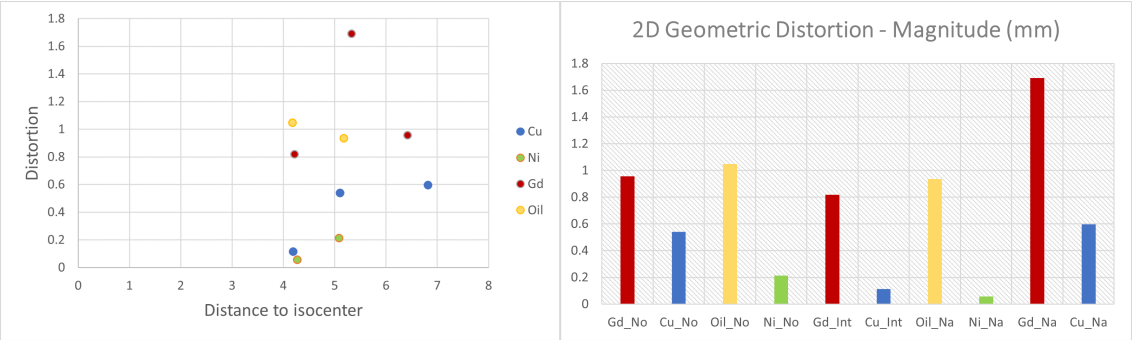

FIGURE 5.1: Distortion results of the "RANDO" studied inserts (slice 2) as a function of their distance to the isocenter and of the substance used. The indications "No", "Na" and "Int" refer, respectively, to the fact that the insert in question is closer to the nose, nape or is the intermediate one, in the case of there being 3 inserts of that substance in this slice. The abbreviations "Gd", "Cu", "Oil" and "Ni" refer, respectively, to "Gadolinium", "Copper Sulfate", "Mineral Oil" and "Nickel Chloride".

Furthermore, we considered other crucial factors such as toxicity and similarity to patient contrasts. Gadolinium, being a common contrast agent used in clinical practice, exhibited high similarity to patient contrasts, making it a favorable choice for our research. Additionally, it had a relatively low toxicity profile compared to other materials such as nickel chloride, which is known to be toxic [232, 233].

The findings indicate that the distortion experienced by nickel chloride is less pronounced than that encountered by the oil and gadolinium, although the sample size is limited. This suggests that, while nickel chloride is employed as a means of distortion correction in phantoms, it may not be an adequate surrogate for distortion in patients.

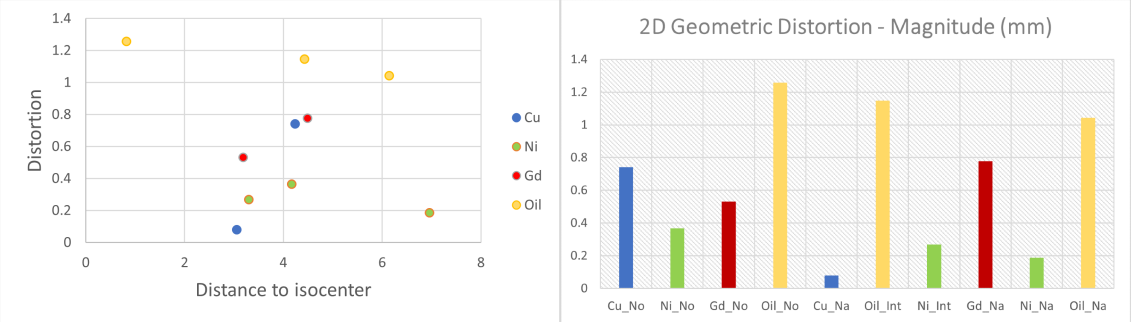

FIGURE 5.2: Distortion results of the "RANDO" studied inserts (slice 3) as a function of their distance to the isocenter and of the substance used.

5.1.2 Optimal Solution Concentration Tests

Upon examining the results of the optimal solution concentration test (Figure 5.3), it becomes apparent that the introduction of a blue FCF colourant in the lower row of plaques does not have a significant effect on the mean intensity values. The values for the plaques with and without the colourant are comparable. This suggests that the addition of the blue FCF colourant does not substantially alter the radiopacity of the plaques. This test also showed a positive correlation between Gd concentration and the resulting mean intensity values. Moreover, although the coloured 1mmol/L plaque actually has a slightly higher value than its non-coloured counterpart, for the other two plaque pairs the introduction of the colourant results in a decrease in the mean intensity values.

After consideration, the preference for gadolinium over copper sulfate is justified by its lower toxicity (particularly important for the phantom filling process, since it was done manually) and clinical relevance, as explained in Section 4.1.1. Additionally, when determining the optimal concentration for the phantom solution, it is important to consider the

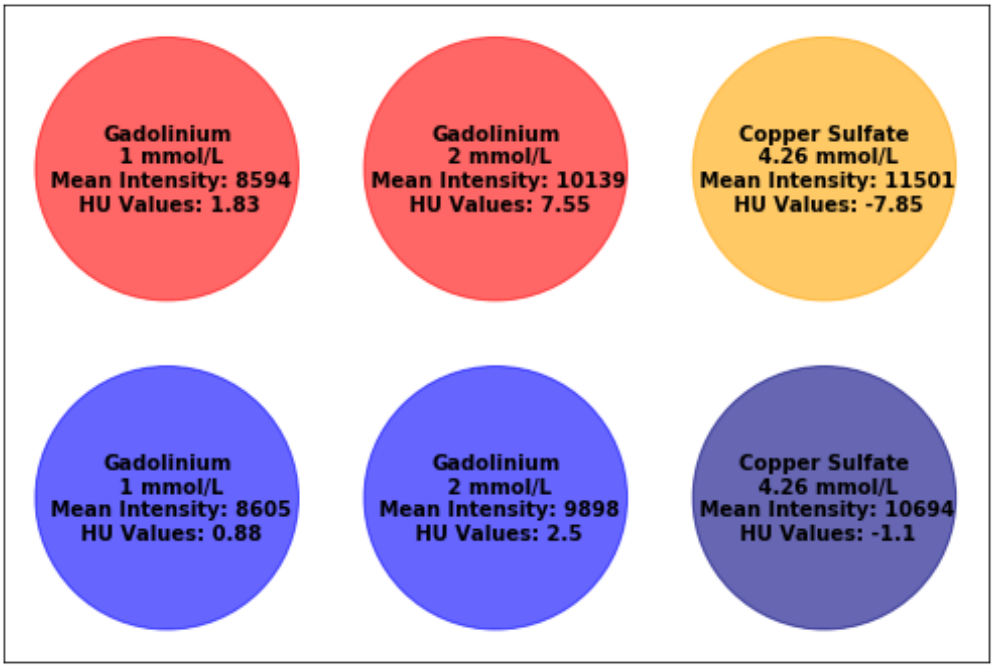

FIGURE 5.3: Experimental setup for concentration and colouring test. The mean pixel intensity and HU value results are shown for each test plaque.

concentration directives provided by regulatory bodies such as the U.S. Food and Drug Administration (FDA) and the Portuguese government. These directives recommend a maximum Gd concentration of 0.1 mmol/kg [234], with the European Committee having recently suggested that this upper limit should only be reached when deemed necessary [235].

Taking into account that the average weight in Portugal is about 72.65 kg [236, 237], this would correspond to 7.265 mmol of Gd. This value would be lower for a patient sample from an oncological treatment institution such as the IPO, due to the weight loss that is prevalent in oncologic patients [238]. As for the test concentrations used, assuming that the average adult blood volume is about 5 L [239] and that the samples correspond to a uniform patient concentration distribution, they would correspond to 5 mmol for the 1mmol/L concentration and 10 mmol using the 2 mmol/L one, with the former being slightly closer to the average patient administered dose. Therefore, from a clinical standpoint and in adherence to these guidelines, the 1 mmol/L Gd concentration becomes more clinically relevant. It should be noted that in reality, the concentration distribution of CA is a complex subject that is not straightforward to model [240], so the aforementioned calculations were approximations.

Furthermore, it is noteworthy that the mean intensity values obtained for the 1 mmol/L Gd concentration plaque (8594) align more closely with typical patient values (≈7000). This finding implies that the 1 mmol/L Gd concentration is more clinically relevant when considering radiopacity in medical imaging applications. Given these results, the chosen final solution and concentration for the geometric phantom was Gd 1 mmol/L.

5.2 Distortion Calculation Algorithm

A preliminary distortion map of the intermediate plaque was made by calculating the squared absolute difference of the image pixel intensities in the MRI and CT images at each point in the scanner's FOV, after co-registration (Figure 5.4). Inherent differences were taken into account (the fact that the acrylic is white in the CT scans and black in the MRI, for example). Qualitatively, it can be seen that there is a correlation between the distortion values and the distance from the isocenter, as expected. The distortion is not radially uniform, and the characteristics of the distortion map are unique to each scanner, due to inherent or acquired equipment inaccuracies, such as regarding the B_0 field homogeneity.

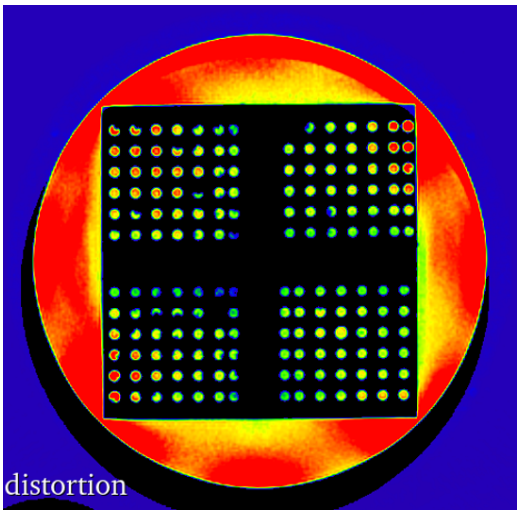

FIGURE 5.4: Initial test - global distortion map. The points with the lowest distortion are color coded in blue, while high distortion regions are color coded in red. Due to limitations of the used software, no color bar is provided.

This is not the most rigorous way of studying the distortion values, as a more accurate way of doing so, made possible by the developed insert detection software, is to match each insert point separately instead of doing a global difference. The evolution of the results of the insert detection software, for the CT scan, are shown in Figure 5.5. The

initial result was not detecting enough inserts, as well as detecting the air bubble on top as an insert. After introducing new intensity thresholds, filtering and a maximum distance from the center threshold, those problems were eliminated.

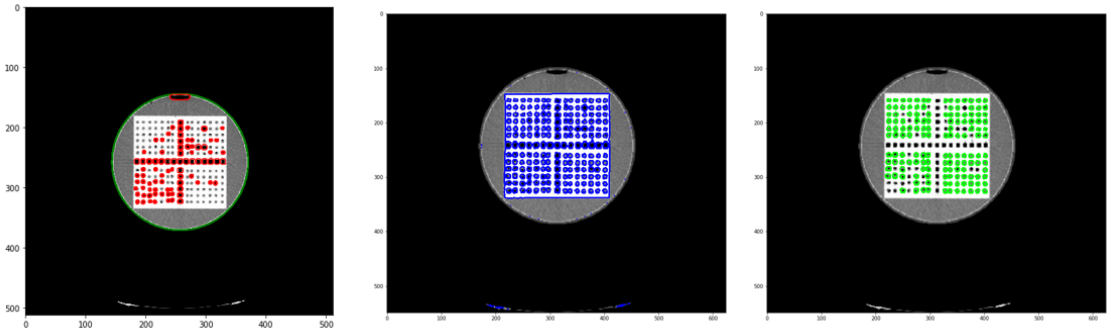

FIGURE 5.5: Progress of the insert detection software for CT scans: initial (left), intermediate (middle) and final (right).

In the intermediate result (middle image in Figure 5.5), every insert is detected, but this is still not ideal; the middle grid corresponds to the inserts where different plaques were glued during the phantom's construction, and so could not be filled. Those inserts, plus the ones with air bubbles, should ideally not be detected in order to get the most precise results, even if less inserts are detected in the final version. Moreover, the grid itself was detected as an insert, which was corrected by introducing a maximum area threshold.

The results for two MRI slices are shown in Figure 5.6. The process was similar to that of the CT scan, but some modifications had to be done, particularly due to the lower resolution of the MRI scans done for this phantom.

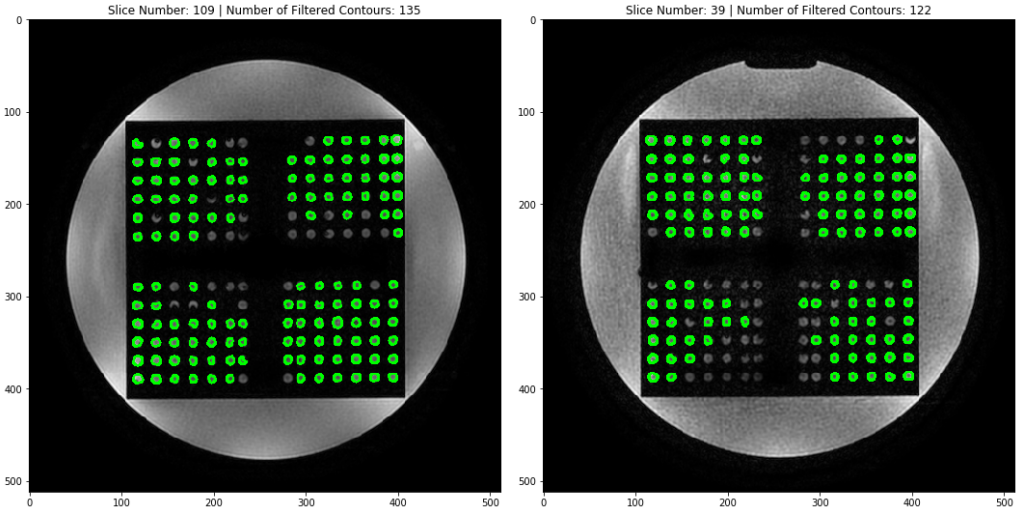

FIGURE 5.6: Insert detection software results for two MRI slices.

Although not all inserts are detected, this actually leads to more accurate overall results. In fact, detecting every insert would be possible by simply relaxing the circularity and intensity threshold criteria. However, this would result in partially air-filled inserts being detected (with consequent loss of centroid coordinate accuracy, as well as increased susceptibility artifacts), but it would mean that slightly circular noise patterns in intermediate slices would be erroneously detected as being inserts. Thus, given that more than 120 inserts were detected for each of the central grid slices, it was considered better to prioritize accuracy over further detection, due to the aforementioned reasons and the strict 1 mm distortion threshold we wished to compare the results to.

As for the distortion part of the software, which calculates distortion after co-registration and CT and MRI insert matching, the results for two slices are presented in Figure 5.7. This visualization tool can intuitively show distortion values and patterns in the image, before data analysis is conducted. For these two slices, each corresponding to a different sequence test, a slight dependence on the distance to the isocenter can be seen, which will be quantitatively analyzed together with the results from other slices for image acquisition optimization (Section 5.3).

As for the global distortion results, meaning joining every studied slice in the phantom, the results for the "Protocol" sequence are shown in detail in Figure 5.8. The distortion dependence on the distance to the isocenter is again perceptible, both for the global and individual components, although the correlation is not strong enough (Pearson r = 0.27) to reliably build a linear model for distortion prediction. This is due to the various, complex factors causing geometric distortion, which justify the need for data analysis software, such as in this study, for distortion quantification. The global results for all tested sequences are shown in Figure 5.9. These will be further discussed and interpreted in the next Section.

Given that for many sequences the distortion results were low in the majority of the test points, the resulting differences would be of the order of less than 5 pixels, resulting in a discrete range of results. Thus, for these cases, the images were upscaled using bicubic interpolation. This method was preferred over others (such as bilinear or nearest neighbour interpolation) to mitigate interpolation artifacts due to its ability to provide smoother results and preserve more details in the upscaled image. By considering a larger

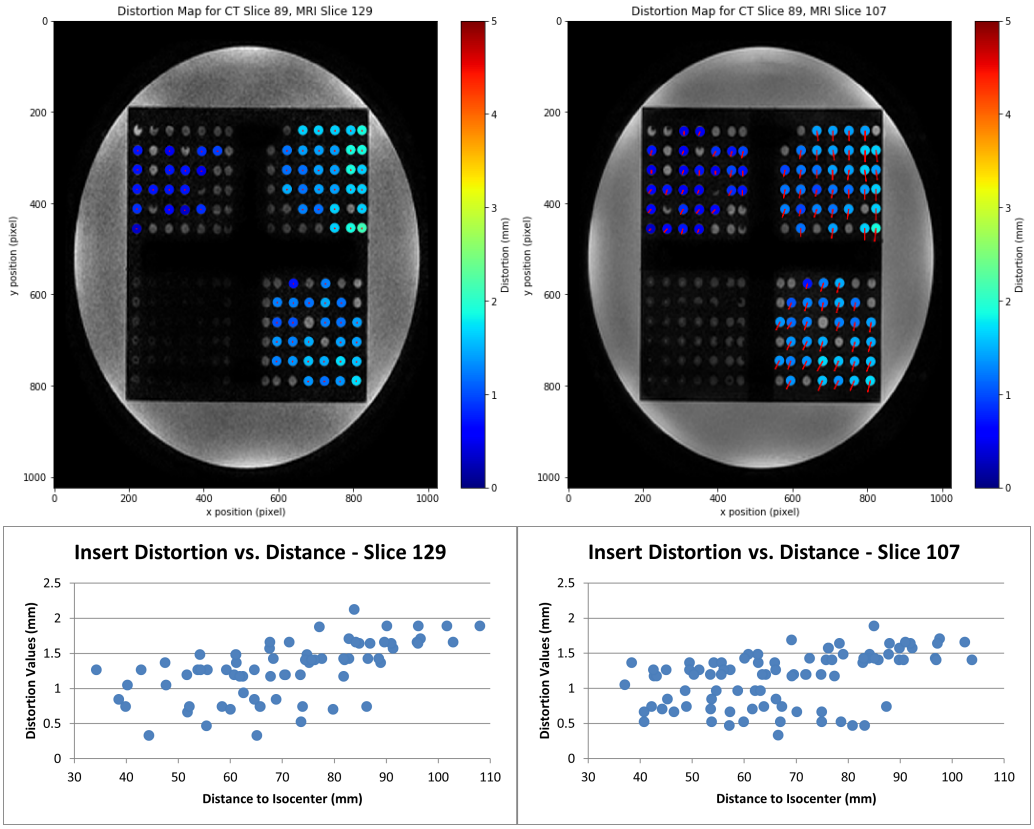

FIGURE 5.7: Visualization and distortion plots for central slices of Test 1 (left) and Test 2 (right). For purposes of visualization, the arrows on the right figure were increased 15 times, to allow perception of the distortion direction.

neighbourhood of pixels and utilizing a higher-degree polynomial approximation, bicubic interpolation offers smoother transitions, reduced blocky artifacts, and better preservation of fine details, while keeping a feasible running time [241, 242]. Even so there is an inevitable degree of discretization, particularly in the x and y distortion plots in Figure 5.8, due to inherent image limitations regarding their finite resolution, and further image upscaling could jeopardize the accuracy of the results.

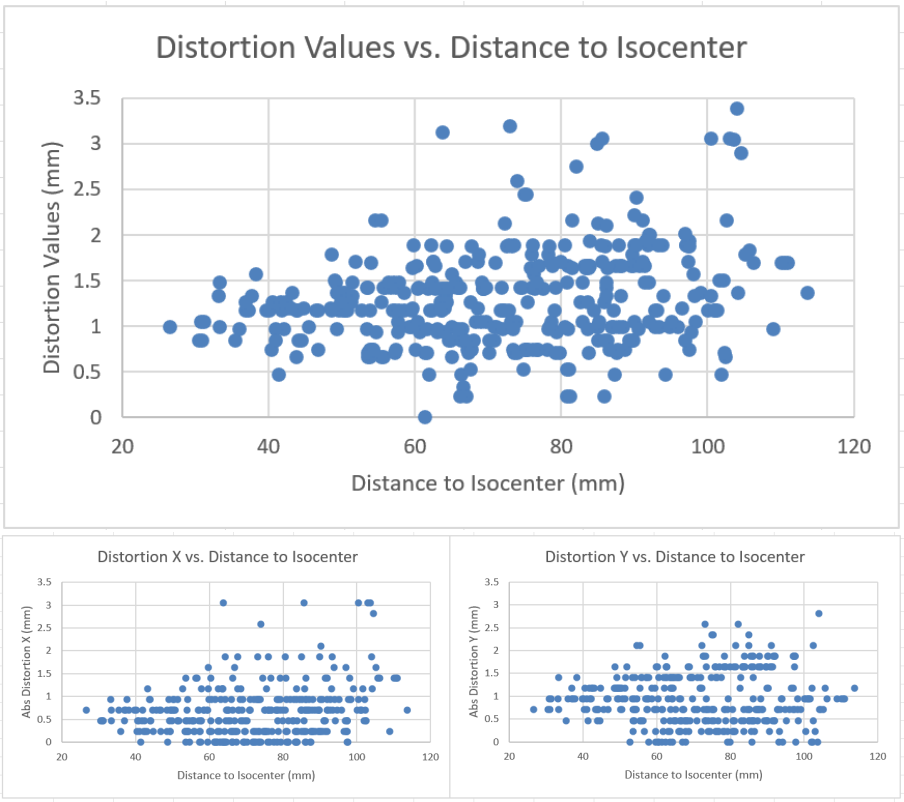

FIGURE 5.8: Global distortion results for the "Protocol" sequence (top), together with their individual components (bottom).

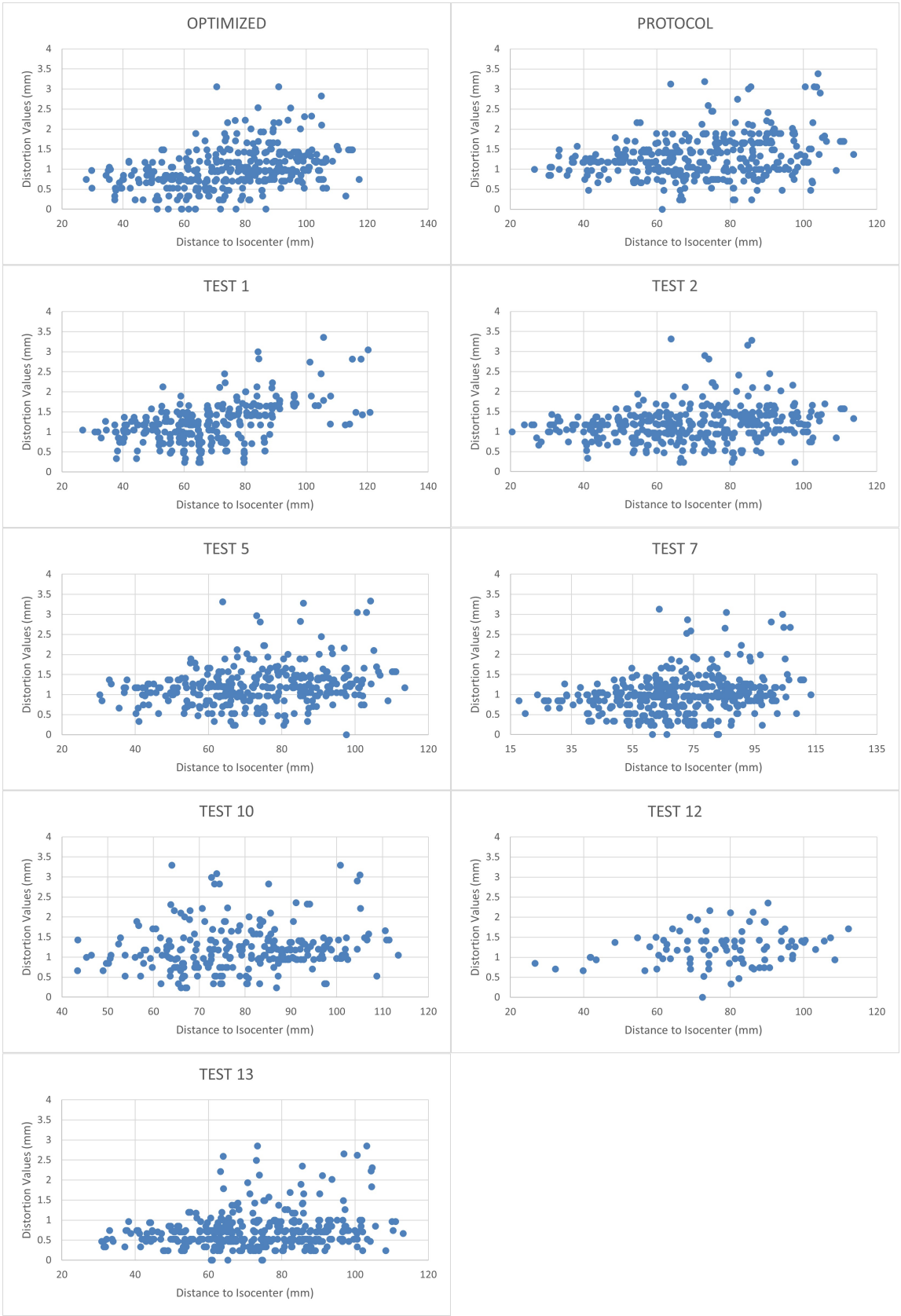

FIGURE 5.9: Distortion results for each tested sequence, as a function of the distance to the isocenter.

5.3 Optimization of 3T MRI Image Acquisition for SRS Treatment Planning

In this Section, the results of the MRI acquisition optimization tests are presented.* The overall results are shown in Table 5.1.

Sequence Name	Acquisition Time (minutes)	SAR (W/kg)	SNR	CNR	Number of Detected Inserts	Mean Distortion (mm)	Max Distortion (mm)
PROTOCOL	4.80	0.291	19.212	5.295	376	1.301	3.380
OPTIMIZED	5.72	0.266	14.791	4.430	404	0.968	3.056
TEST 1	5.90	0.256	19.927	5.645	368	1.222	3.356
TEST 2	4.78	0.473	20.119	7.292	412	1.181	3.315
TEST 5	4.77	0.291	17.789	4.775	360	1.207	3.331
TEST 7	18.30	0.296	10.957	2.740	439	0.978	3.127
TEST 10	4.78	0.246	15.604	4.735	263	1.191	3.290
TEST 12	3.15	0.037	10.786	5.185	88	1.215	2.355
TEST 13	4.78	0.291	19.545	5.235	384	0.725	2.851

TABLE 5.1: Results of the sequence parameter tests.

To compare the average distortion values among multiple sequences, a one-way analysis of variance (ANOVA) test was used. The one-way ANOVA can be used to test if there are statistically significant differences in the means of three or more groups (in this case, between the 9 tested sequences). Thus, the mean distortion differences were all deemed significant within a significance level of $\alpha = 0.001$.

In the following, a detailed analysis of the tested sequences is presented. Then, in Section 5.3.3, global correlations are tested.

The results shown in Table 5.1 suggest that the current sequence used by the IPO, labeled as "Protocol", exhibits a relatively short acquisition time, compared to the remaining tested sequences, of 4.80 minutes, making it efficient for an institution with heavy patient load. It also demonstrates a moderate SAR of 0.291 W/kg, indicating acceptable levels of energy deposition in the patient's body. However, the "Protocol" sequence sacrifices location accuracy for overall image quality. Indeed, although its SNR is high (19.212),

* Test 13 MRI sequence video.

the mean and maximum distortion values are the highest among the tested sequences. In particular, the mean distortion is above 1 mm, which was considered the threshold for SRS treatment planning.

In this regard, the ”Optimized”, ”Test 7” and ”Test 13” sequences were the only ones that achieved sub-millimetric mean distortion values. However, ”Test 7” had an imaging time of 18.30 minutes, which is clinically unfeasible, given the current 4.80 minutes of the ”Protocol” sequence. Thus, only the ”Optimized” and ”Test 13” sequences are eligible as candidates for significant improvements over the ”Protocol” sequence (analyzed in Section 5.3.2). We will first analyze the sequences that did not perform as well, trying to understand the reason and its practical significance:

- **Test 1**: This test sacrificed imaging time (by lowering the slice thickness) in order to achieve better image quality and lower distortion values. Although it shows slight improvements compared to the protocol sequence in most tested parameters, the improvements are not significant enough to justify the increased imaging time. In particular, the 18% increase in imaging time is only compensated by a 6% distortion reduction.

- **Test 2**: This sequence involved increasing the flip angle from 12° to 18°. A larger flip angle means that the spins are tipped more, resulting in a greater excitation of the nuclear spins and higher signal intensity in the acquired image. However, a larger flip angle requires a higher RF power deposition to achieve the desired excitation. Thus, the increase in SAR was theoretically expected. Although it is not ideal, this is not a limiting factor by itself, given that, as previously mentioned, the value is still within the safety range. This sequence actually performs better than the protocol one overall, with a similar imaging time, but the 9.22% distortion reduction is still not enough to place its mean distortion below 1 mm, as is the case for the ”Optimized” and ”Test 13” sequences.

- **Test 5**: This test involved using manual shimming techniques instead of the default automatic ones. Although this sequence showed a 7.22% distortion reduction compared to the protocol one, it sacrificed image quality (SNR and CNR) to do it, by 7.41% and 9.82%, respectively. This may actually be a worthwhile trade-off, but this sequence is not further considered as an improvement over the protocol one because other sequences achieved better distortion results without this trade-off.

- **Test 7**: This sequence used 2 excitations for each repetition, as well as an increased bandwidth in order to achieve sub-millimetric distortion values. However, not only does it reduce SNR and CNR by almost 50%, it also increases the imaging time to 18.30 minutes. As explained before, this is a limiting factor, as it renders it clinically unfeasible. In short, the trade-off is a 24.83% reduction in distortion for a $\approx$ 50% decrease in SNR and CNR, and a 281.25% increase in imaging time.

- **Test 10**: This time, the flip angle was lowered to 10°. This has the opposite effect, regarding the SAR, of Test 2, and a slight SAR decrease is indeed verified. However, this sequence performs worse than the protocol one in terms of the SNR, CNR and the number of detected inserts, which compromises its use, given the comparatively small (8.46%) distortion reduction.

- **Test 12**: This multi-echo GRE sequence showed interesting results. In fact, not only is it significantly faster than the other ones (34.38% compared to the protocol one), the SAR is also the lowest by far and the maximum distortion is also the lowest, implying a more homogeneous distortion profile. However, the average distortion is still considerably high (6.61% reduction compared to the protocol) and the SAR is reduced by $\approx$ 50%. Moreover, the number of detected inserts is very low, which means that this sequence may have difficulty in reliably identifying small lesions such as brain metastasis.

5.3.1 Weighting factors

After the brute force process for definition of the parameter's weights, the final three candidate weighting sets resulting from the optimization algorithm designed to define the β Factor (Section 4.4) are presented in Figure 5.10. After analyzing these options, "Factor 1" was chosen as the β factor, since its parameter weights are more appropriately balanced, particularly those that pertain to image quality. The other two factors were discarded.

	Acquisition Time (minutes)	SAR (W/kg)	SNR	CNR	Number of detected inserts	Mean distortion (mm)	Max distortion (mm)
FACTOR 1	9	3	9	8	6	10	4
FACTOR 2	6	1	6	6	4	7	2
FACTOR 3	9	2	7	6	7	10	3

FIGURE 5.10: Final weighting set candidates.

Thus, the λ and β factors assigns different importance to different parameters, having been defined using two different methods (Section 4.4). Indeed, there is no unique way to quantitatively determine the "best" sequence, given the subjective and complex nature of this determination. In the following, given that the λ factor is the most comprehensive one, and we have all the necessary factors, λ will be considered the default quantification metric. Table 5.2 presents the full, color-coded results, including the λ and β factors.

Sequence Name	Acquisition Time (minutes)	SAR (W/kg)	SNR	CNR	Number of Detected Inserts	Mean Distortion (mm)	Max Distortion (mm)	Lambda Factor	Beta Factor
PROTOCOL	4.80	0.291	19.212	5.295	376	1.301	3.380	0.277	0.456
OPTIMIZED	5.72	0.266	14.791	4.430	404	0.968	3.056	0.260	0.420
TEST 1	5.90	0.256	19.927	5.645	368	1.222	3.356	0.231	0.473
TEST 2	4.78	0.473	20.119	7.292	412	1.181	3.315	0.484	0.554
TEST 5	4.77	0.291	17.789	4.775	360	1.207	3.331	0.263	0.401
TEST 7	18.30	0.296	10.957	2.740	439	0.978	3.127	0.012	0.058
TEST 10	4.78	0.246	15.604	4.735	263	1.191	3.290	0.176	0.295
TEST 12	3.15	0.037	10.786	5.185	88	1.215	2.355	0.126	0.392
TEST 13	4.78	0.291	19.545	5.235	384	0.725	2.851	1.000	1.000

TABLE 5.2: Full color-coded results of the sequence parameter tests, including the λ and β factors. Green and red are used to highlight, respectively, sequence parameter results that were significantly better or worse than the average for all tested sequences, in order to facilitate its analysis.

The weighting parameter values of "Test 13" and "Test 2" are the highest, with "Test 13" being a clear standout. It is interesting to note that both weighting parameters show general agreement in the results and sequence quality ordering, although the α factor favours sequences with high SNR and has a smaller result amplitude. Thus, the λ factor separates the sequence results more distinctively. On the other hand, it assigns a higher importance to the acquisition time, as can be seen by comparing the results for the "Protocol" and "Test 1" sequences (Table 5.2. Thus, as previously mentioned, these weighting factors offer complimentary qualitative information, and the choice of which one to use must be made according to the priorities and clinical applications of the institution in question.

The plots illustrating the general results are shown in Figure 5.11. Out of these, the "Optimized" and "Test 13" sequences show great potential, and will be analyzed in the next Section.

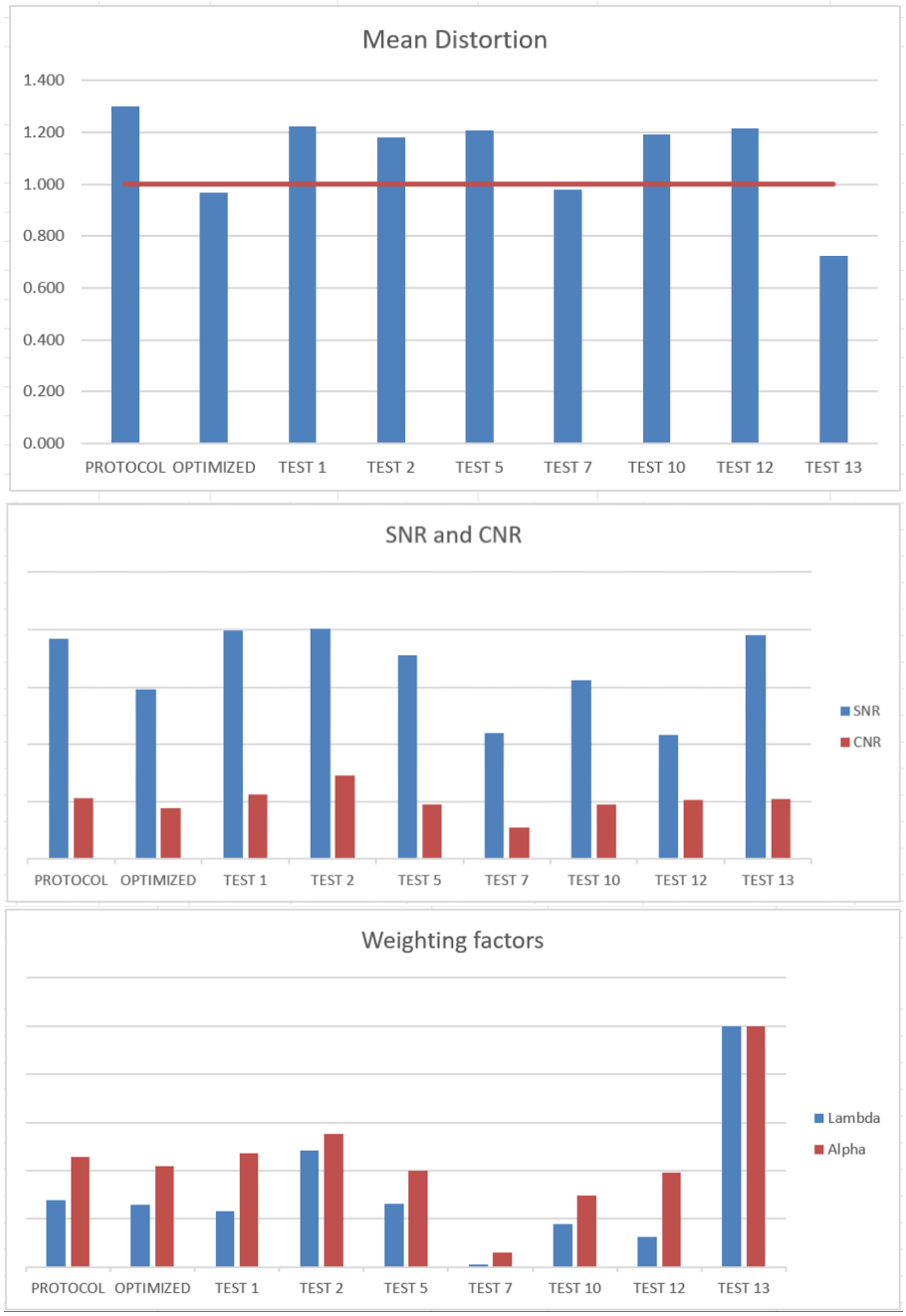

FIGURE 5.11: Mean distortion (top), SNR and CNR (middle), and weighting factors (bottom) values for all tested sequences.

5.3.2 Sequences that showed improvements over the "Protocol" sequence

As previously mentioned, the two sequences eligible to bring significant improvements over the protocol one are the "Optimized" and "Test 13" sequences, mainly due to the fact that they can achieve sub-millimetric contrast without great imaging time increases, as reflected from their higher weighting parameter values (Table 5.2). The pattern of distortion reduction with distance to the isocenter can be seen in Figure 5.12.

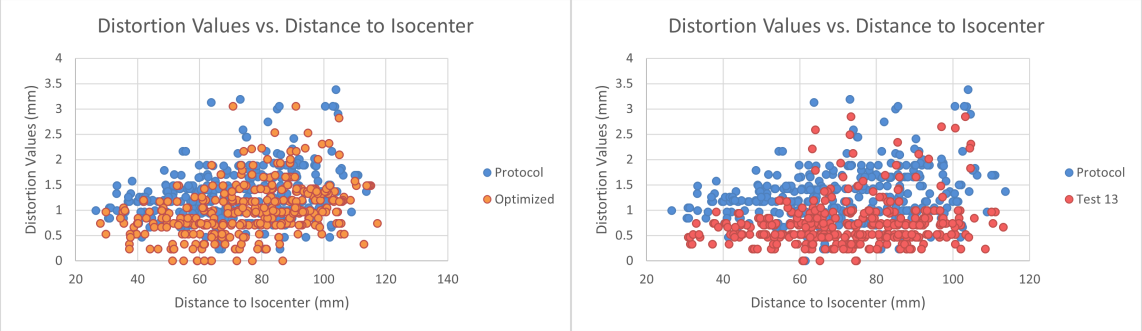

FIGURE 5.12: Comparison between the distortion values of the "Protocol" sequence and the two best performing sequences in terms of mean geometric distortion ("Optimized" and "Test 13").

However, a detailed comparison of these two sequences shows that the "Optimized" one falls significantly short of the "Test 13" sequence. Indeed, it reduces the mean distortion by 25.60%, but it sacrifices image quality to do so (23.01% and 16.34% for SNR and CNR, respectively), while also increasing the acquisition time by 19.17%. These results are positive, as no single parameter is reduced by more than what the distortion is reduced by, but the combined results of 3 parameters being sacrificed for distortion reduction worsens its potential. Still, it could be an alternative worth considering for SRS treatment planning, were it not for the fact that the "Test 13" sequence does not sacrifice any parameter.

Indeed, the "Test 13" sequence emerges as a clear improvement over the protocol sequence. It is similar in the acquisition time, SAR, SNR, CNR and detected inserts, while significantly lowering the mean and maximum distortion (by 44.27% and 15.65%, respectively). This test reversed the phase-encoding direction to AP instead of PA.

There was no theoretical *a priori* reason for the improvement brought upon by this sequence. In fact, while some distortion correction methods involve acquiring two sets of images with reversed phase-encoding directions [243], this sequence did not included any extra set of images, in order not to double the imaging time. Therefore, the cause of this very positive result cannot be confidently ascertained, as no published research was found to delve into this particular topic. Metal artifacts have been shown to depend on the phase-encoding direction in some cases [244], but the phantom used contained no metal, being made of acrylic. On the other hand, the gadolinium used in the contrast solution is a metal, and although its concentration was low, it is still possible that it is the reason for this behaviour. Given that gadolinium is the most commonly used CA in patients for brain imaging, this might mean a direct translation for human patient results.

However, without further exhaustive testing and research, it is not possible to make a definite conclusion regarding the cause of this improvement, as it might have to do with any of the used equipment parameters (including the scanner itself), as well as with any eliminated artifact, possibly specific to this sequence or field strength and thus relatively unexplored.

Therefore, an idea for future work, before any potential clinical implementation, would be to run these tests on different 3 T scanners, before proceeding to conduct tests on voluntary patients to check if this behaviour is matched on humans. In the next Section, we analyze correlations detected during the data analysis stage, with the goal of finding statistical patterns that could help explain the obtained results.

5.3.3 Correlation tests

We conducted Spearman's rank correlation coefficient results for mean distortion, to analyze any correlation between the mean distortion and other parameters. This method was preferred over Pearson's product-moment correlation for three main reasons: firstly, the associations may not be linear; secondly, because of its robustness to outliers; finally, because some of the variables, such as the SAR or acquisition time, show skewed distributions, and thus may not be assumed to follow a normal distribution. This last reason is important, as rank-based significance tests are preferred when the data cannot be assumed to follow any particular distribution [245], as in this case. A more subtle reason is that we are more interested in ranking the tested sequences more than in the precise nature of the correlations, so that the outcome (mean distortion) can be treated as an ordinal variable. The results are shown in Table 5.3.

For the studied sample, there were no significant correlations between the mean distortion and other parameters using a significance level $\alpha = 0.05$, although we can briefly look into two which are significant for $\alpha = 0.1$: TE and the maximum distortion. The latter is clear, implying that sequences with higher maximum distortion values also have higher mean distortion values. As for positive correlation between mean distortion and TE, it is also theoretically sensible. It can be due to many factors, such as the fact that with longer TE, there is more time for dephasing to occur, resulting in increased distortions in the acquired images. Moreover, longer TE values can lead to more pronounced distortions due to the longer period during which the magnetic field inhomogeneities can influence the phase of the acquired signal.

Correlated parameters	Correlation	p-value
Slice Thickness vs Mean distortion	0.079	0.839
TR vs Mean distortion	0.347	0.360
TE vs Mean distortion	0.621	0.074
NEX vs Mean distortion	-0.274	0.476
BW vs Mean distortion	-0.339	0.372
Flip angle vs Mean distortion	-0.091	0.815
Acquisition Time vs Mean distortion	-0.119	0.761
SAR vs Mean distortion	-0.339	0.372
Mean distortion vs Max distortion	0.633	0.067

TABLE 5.3: Spearman's rank correlation coefficient results for mean distortion. Correlations values whose absolute value is greater than 0.25 are highlighted. Significant correlations at $\alpha = 0.1$ and those with $p > 4\ \alpha$ (low correlation significance) are highlighted in green and red, respectively.

It is also interesting to note that there was no correlation found between the mean distortion and parameters such as the slice thickness, bandwidth or the acquisition time, for the studied sample. It may only be relevant to FSPGR sequences, but it implies that any optimization attempts should not particularly focus on slice thickness or bandwidth alterations. It also means, within the confines of this study, that longer sequences are not necessarily better in terms of geometric distortion results.

Next, we analyze, using the same method, significant correlations found in this study for other parameters, using $\alpha = 0.05$, as shown in Table 5.4. As this work involved parsing through a high volume of data, these statistical tests serve both as verification steps for expected behaviour, as well as a way to look for patterns that could explain the obtained results. In fact, most of these correlations are a byproduct of the MRI sequence design principles. For example, the first negative correlation (Slice Thickness vs Acquisition Time) is expected, as thinner slices require more acquisitions to cover the desired anatomical volume, leading to increased acquisition time.

Thus, the correlations which provide new information are the ones regarding the number of detected inserts. The results suggest that, for the presently studied sample, it is beneficial for sequences to have lower TE values and higher bandwidth values in order to improve insert detection. This increase in bandwidth carries a corresponding increase in the SAR value (these two variables were perfectly matched in the rank test) which, although not desirable, may be an acceptable trade-off as long as the SAR values do not exceed the safety regulatory limits. The correlation between the λ and α factors verifies the aforementioned fact that the overall ordering provided by the two weighting factors

Correlated parameters	Correlation	p-value
Slice Thickness vs Acquisition Time	-0.695	0.038
TR vs TE	0.700	0.036
TR vs BW	-0.743	0.022
TR vs SAR	-0.743	0.022
TE vs Number of Detected Inserts	-0.749	0.020
TE vs Alpha factor	0.785	0.012
BW vs SAR	1.000	0.000
BW vs Number of Detected Inserts	0.814	0.008
SAR vs Number of Detected Inserts	0.814	0.008
SNR vs CNR	0.817	0.007
Lambda Factor vs Alpha Factor	0.867	0.002

TABLE 5.4: Spearman's rank correlation coefficient for other results deemed significant using $\alpha = 0.05$.

is similar, without being identical.

Chapter 6

Conclusion

In this thesis, the challenge of geometric distortion in MRI for SRS treatment planning was addressed. The presence of geometric distortion poses significant concerns, especially in scenarios where stringent accuracy requirements demand distortion thresholds of no more than 1 mm, as is the case with SRS treatment planning. The research focused on optimizing MRI sequence parameters and quantifying distortion values within the FOV of a 3 T GE Signa MRI scanner used for SRS treatment planning at the IPO-Porto.

To achieve these objectives, a custom geometric phantom to accurately assess geometric distortion was designed and built. Through preliminary investigations in an anthropomorphic phantom, we found gadolinium to be an ideal candidate for our study, as its distortion characteristics closely resembled those observed with patients. Distortion quantification software that automated the detection and matching of phantom inserts between MRI and CT scans was developed, enabling accurate calculation of distortion values. The software also presented the distortion vectors at each matched insert.

Additionally, the MRI image acquisition process was optimized by systematically exploring different acquisition parameters, aiming to reduce geometric distortion while considering factors such as acquisition time, SAR, SNR and CNR.

The results revealed important findings regarding sequence optimization and distortion reduction. Among the tested sequences, the ”Test 13” sequence, which involved reversing the phase-encoding direction, demonstrated significant improvement over the existing ”Protocol” sequence used at IPO-Porto. It achieved a remarkable reduction in the mean distortion values without compromising imaging time or image quality. The cause of this improvement remains to be definitively determined and warrants further investigation on different scanners and in voluntary patients.

The outcomes of this research may have significant implications for MRI-based treatment planning for SRS at the IPO-Porto. By addressing the challenge of geometric distortion, we have contributed to improving the accuracy and reliability of MRI scans, particularly in the context of SRS. The findings highlight the potential for optimized sequence parameters to achieve sub-millimetric distortion values while maintaining acceptable imaging time and image quality.

Additional future work focused on reproducing and analysing the cause of the clear improvement in geometric distortion verified when inverting the phase encoding direction is merited, as well as an expansion of the distortion quantification software to incorporate the z-axis component, thereby giving 3D distortion information.

The developed distortion quantification software and the insights gained from our study can be applied not only to the specific MRI scanner at IPO-Porto but also to other MRI systems. This research builds upon previous studies and advancements in MRI-based SRS treatment planning, and may be used as a foundation for future ones, always keeping in mind the final goal of enhancing patient outcomes in radiotherapy. As the magnetic field strength of the scanners used in MRI centers increases, so too will the need for better compensating distortion correction techniques.

Appendix A

Experimental Details - Additional Figures

A.1 Phantom filling tests

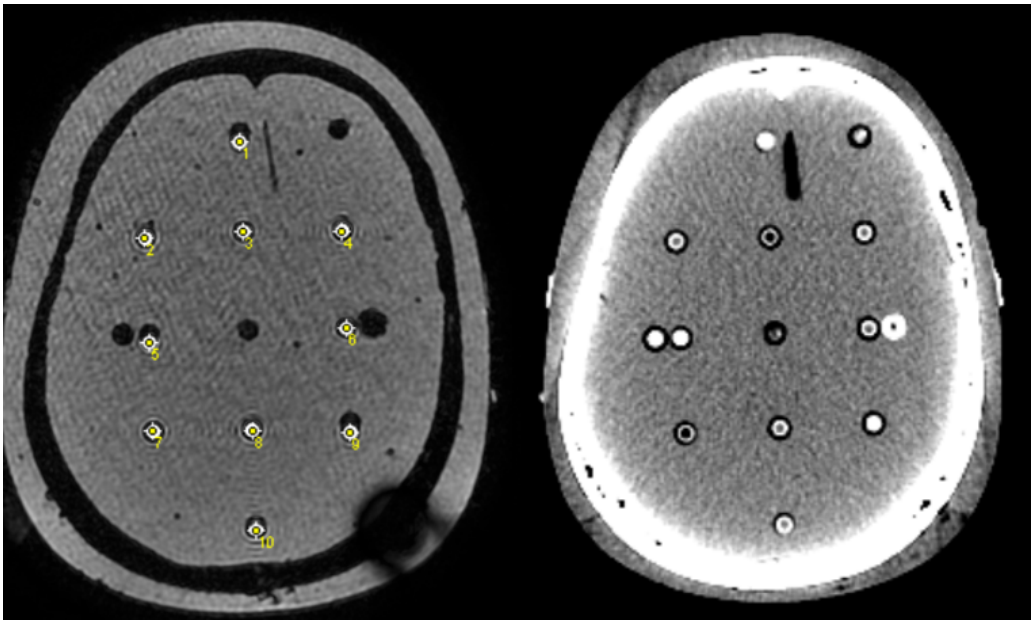

FIGURE A.1: MRI (left) and CT (right) scans of slice 2 of "RANDO" head phantom, along with the studied insert points (images displayed not to scale).

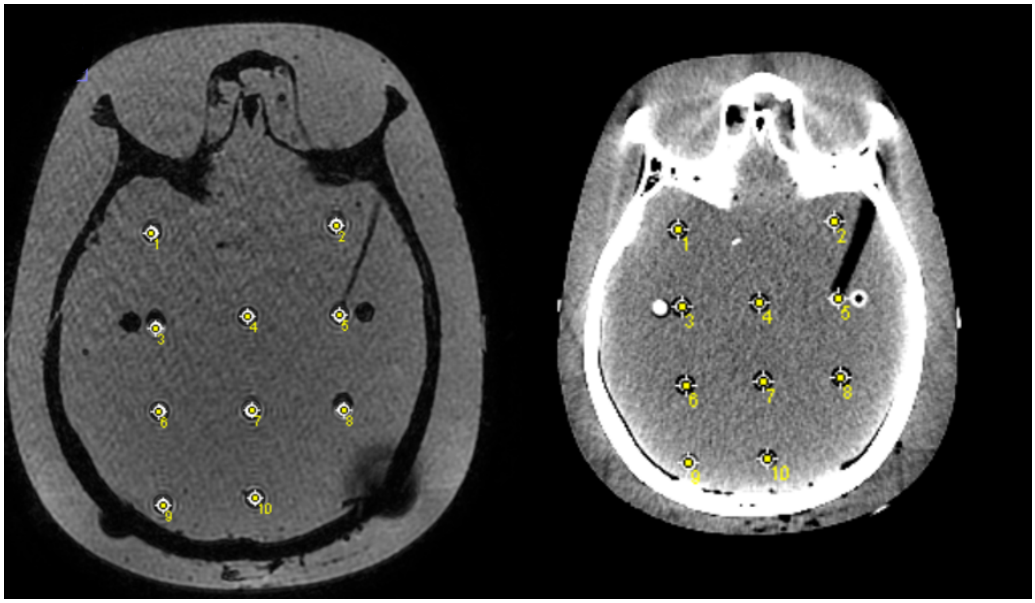

FIGURE A.2: MRI (left) and CT (right) scans of slice 3 of "RANDO" head phantom, along with the studied insert points (images displayed not to scale).

A.2 Phantom Design Details and Results

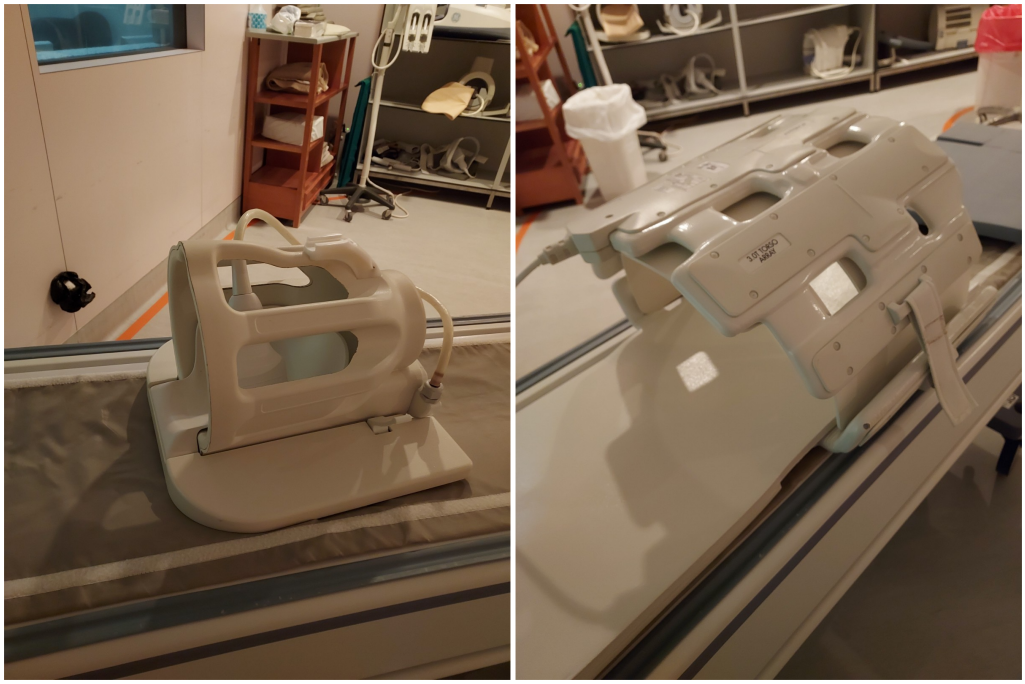

FIGURE A.3: Head (left) and torso (right) antennae considered in this study. Only the head antenna was used.

Given the 10.75 cm radius of the cylindrical phantom enclosure that existed in the IPO already, the square grids were made to fit them perfectly. Thus, the side of the maximal square that could fit that circle was calculated using the formula $l = r\sqrt{2}$, where l is the

TABLE A.1: Characteristics of some of the phantoms used for measurement of geometric distortion in MRI.

Phantom	General design notes	Dimensions	Material	Grid Thickness	Grid Spacing
CIRS large field MRI distortion phantom (604-GS)	**Cylinder**, which contains an orthogonal 3D grid inside the volume.	300 x 276 x 330mm (length, height, diameter)	**Acrylic** Plastic rods for grids	3 mm (diameter)	**20.3mm** (I-S), 20.5mm (AP) and 21.5mm (L-R). Grid intersections enhanced by 6mm diameter sphere.
ACR MRI	**Cylinder**. Inside the cylinder are multiple structures for a variety of scanner performance tests.	The inside length is 148 mm; the inside diameter is 190 mm. (small enough for head coils)	**Acrylic** (+ glass and silicone rubber). Filled with NiCl2 / NaCl solution.	1.1, 1.0 and 0.9 mm (left, center, right pair)	2x hole diameter
3D printed 5mm grid (Isokoski 2021 thesis)	**Cylinder** + 2 grids fitted inside.	-----	MED610 (bio-compatible)	1 mm	5 mm
Elekta MRI	**Cylinder** with 190 marker points	180.5 mm in diameter and 131 mm in height	**Acrylic**	2 mm diameter, 2.5 mm height	------
CIRS MRI **Head** Phantom (603-GS)	Tissue equivalent, anthropomorphic design. Includes left and right air voids to simulate each ear canal.	32 x 24 x 18 cm	Skull: Plastic-based bone substitute Interstitial/ Soft tissues: Water-base polymer Grid: Reinforced nylon	2.5 mm diameter cross-like shaped rods	10mm (I-S), 10.5mm (AP) and 11mm (L-R)
Magphan® RT Phantom (820 model)	The Magphan® RT 820 has a two-piece cylindrical configuration (top and bottom) – **modular** design.	35 x 27 x 21cm	Acrylic (prob.) Filled with solution (96.4% water + Sodium Chloride, PVP40, Copper Sulfate, Potassium Sorbate, Blue Food Colorant)	1 cm fiducial spheres. 24 contrast spheres with 1.7mm diameter, 12 distinct solutions	---------
GRID 3D Quasar (Modus QA)	**Cube**. Designed for use with Gamma Knife but can be used for MRI or CT as well.	11 x 13 x 14 cm	**Acrylic.**	1.5 mm	----------
Spectronic Medical GRADE phantom	Cylindrical, consisting of approximately 1,200 small spherical markers at known positions embedded in expanded foam	----------	Acrylic (prob.) The markers are made of polyethylene glycol.	17 mm diameter for markers.	Aprox. 50 mm, with smaller spacing near the edges (30 mm).
MRID 3D Quasar (Modus QA)	Cylinder.	39.4 cm diameter x 39.4 cm long (Imaging slightly <)	**Acrylic.** Filled with Paraffinic Mineral Oil	----------	----------

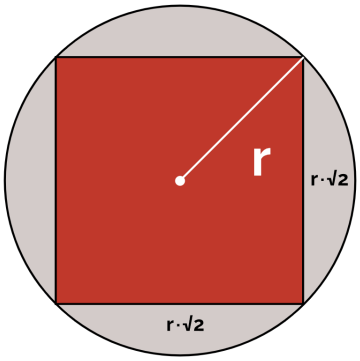

FIGURE A.4: Maximal square in a circle

square side and r is the circle radius (Figure A.4). Thus, the square side was determined to be $10.75\sqrt{2} = 15.20$ cm.

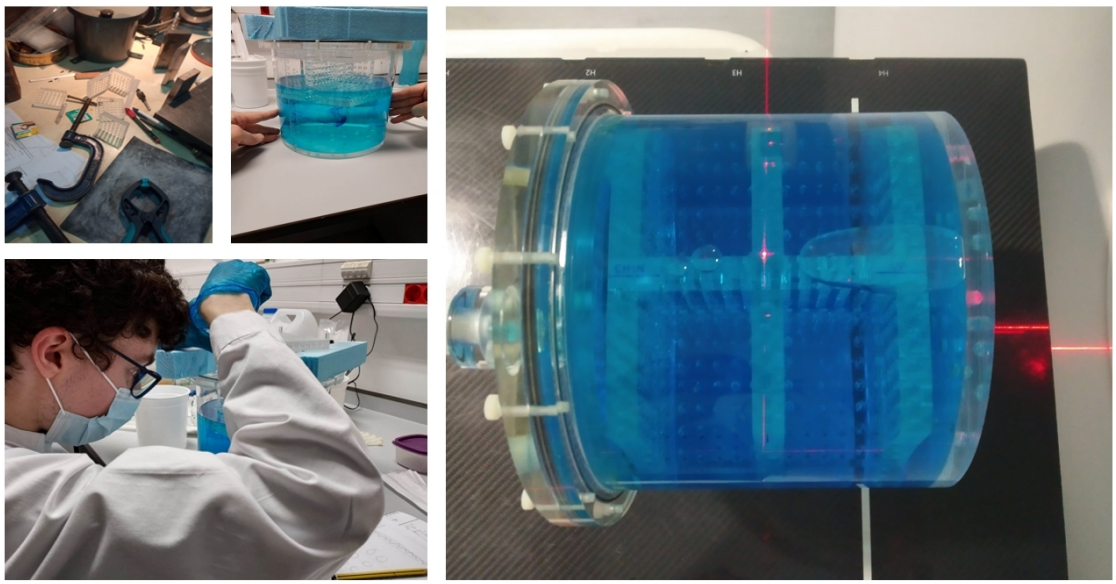

FIGURE A.5: Photographs of the construction and filling process of the geometric phantom: construction at the faculty workshop and background filling, including colourant addition (top left); insert filling (bottom left); finalized phantom in CT imaging table (right).

Bibliography

[1] Denis Le Bihan, Peter Jezzard, James Haxby, Norihiro Sadato, Linda Rueckert, and Venkata Mattay. Functional magnetic resonance imaging of the brain. *Annals of Internal Medicine*, 122(4):296–303, 1995. [Cited on page 4.]

[2] Maria A Schmidt and Geoffrey S Payne. Radiotherapy planning using mri. *Physics in Medicine & Biology*, 60(22):R323, 2015. [Cited on page 4.]

[3] Marie E Korsholm, Line W Waring, and Jens M Edmund. A criterion for the reliable use of mri-only radiotherapy. *Radiation Oncology*, 9:1–7, 2014. [Cited on page 4.]

[4] Meshal Alzahrani, David Broadbent, Robert Chuter, Bashar Al-Qaisieh, Steven Jackson, Hutton Michael, Robert Johnstone, Simon Shah, Andreas Wetscherek, H. Chick, Jonathan Wyatt, Hazel McCallum, and Richard Speight. Audit feasibility for geometric distortion in magnetic resonance imaging for radiotherapy. *Physics and Imaging in Radiation Oncology*, 15:80–84, 07 2020. [Cited on pages 4, 30, 59, and 61.]

[5] Emily Johnstone, Jonathan Wyatt, Ann Henry, Susan Short, David Sebag-Montefiore, Louise Murray, Charles Kelly, Hazel McCallum, and Richard Speight. A systematic review of synthetic ct generation methodologies for use in mri-only radiotherapy. *International Journal of Radiation Oncology*Biology*Physics*, 100, 09 2017. [Cited on page 4.]

[6] Richard Pötter, Bettina Heil, Lorenz Schneider, Horst Lenzen, Christl Al-Dandashi, and Elmar Schnepper. Sagittal and coronal planes from mri for treatment planning in tumors of brain, head and neck: Mri assisted simulation. *Radiotherapy and Oncology*, 23(2):127–130, 1992. [Cited on page 4.]

[7] Lothar R Schad, Günther Gademann, Michael Knopp, Hans-J Zabel, Wolfgang Schlegel, and Walter J Lorenz. Radiotherapy treatment planning of basal meningiomas: improved tumor localization by correlation of ct and mr imaging data. *Radiotherapy and Oncology*, 25(1):56–62, 1992. [Cited on pages 4 and 61.]

[8] Kazufumi Kagawa, W Robert Lee, Timothy E Schultheiss, Margie A Hunt, Andrew H Shaer, and Gerald E Hanks. Initial clinical assessment of ct-mri image fusion software in localization of the prostate for 3d conformal radiation therapy. *International Journal of Radiation Oncology* Biology* Physics*, 38(2):319–325, 1997. [Cited on page 4.]

[9] Julian G Rosenman, Elizabeth P Miller, and Tim J Cullip. Image registration: an essential part of radiation therapy treatment planning. *International Journal of Radiation Oncology* Biology* Physics*, 40(1):197–205, 1998. [Cited on page 4.]

[10] Annette Fransson, Pedro Andreo, and Richard Pötter. Aspects of mr image distortions in radiotherapy treatment planning. *Strahlentherapie und Onkologie : Organ der Deutschen Röntgengesellschaft ... [et al]*, 177:59–73, 03 2001. [Cited on pages 4, 5, 22, 30, 31, 33, 34, 35, 40, 41, 50, 58, 59, and 60.]

[11] Vincent S Khoo, David P Dearnaley, David J Finnigan, Anwar Padhani, Steven F Tanner, and Martin O Leach. Magnetic resonance imaging (mri): considerations and applications in radiotherapy treatment planning. *Radiotherapy and Oncology*, 42(1):1–15, 1997. [Cited on page 4.]

[12] Quentin Gibaru, Christophe Inguimbert, Pablo Caron, Mohamed Belhaj, Mélanie Raine, and Damien Lambert. Surface ionizing dose deposited by low energy electrons (10 ev–10 kev) in eleven monoatomic materials: Monte carlo calculations and analytical expressions. *Applied Surface Science*, 576:151813, 2022. [Cited on page 5.]

[13] John Ambrose Fleming. *The principles of electric wave telegraphy and telephony*. Longmans, Green, 1919. [Cited on page 5.]

[14] R.W. Brown, Y.C.N. Cheng, E.M. Haacke, M.R. Thompson, and R. Venkatesan. *Magnetic Resonance Imaging: Physical Principles and Sequence Design*. Wiley, 2014. [Cited on pages xiii, 5, 9, 10, 11, 12, 13, 17, 23, 32, and 51.]

[15] Cláudio Pereira. Mri (1.5 and 3 tesla) sequence optimization for use in orthopaedics. 2016. [Cited on pages 5 and 6.]

[16] Claude Cohen-Tannoudji, Bernard Diu, and Frank Laloe. Quantum mechanics, volume 1. *Quantum Mechanics*, 1:898, 1986. [Cited on page 6.]

[17] V. Kuperman. *Magnetic Resonance Imaging: Physical Principles and Applications*. Elsevier Science, 2000. [Cited on pages 6, 11, 17, 19, 22, and 36.]

[18] Kenneth S Krane. *Introductory nuclear physics*. John Wiley & Sons, 1991. [Cited on page 6.]

[19] David J Griffiths and Darrell F Schroeter. *Introduction to quantum mechanics*. Cambridge university press, 2018. [Cited on page 6.]

[20] George E Uhlenbeck and Samuel Goudsmit. Ersetzung der hypothese vom unmechanischen zwang durch eine forderung bezüglich des inneren verhaltens jedes einzelnen elektrons. *Die Naturwissenschaften*, 13(47):953–954, 1925. [Cited on page 6.]

[21] Donald W McRobbie, Elizabeth A Moore, Martin J Graves, and Martin R Prince. *MRI from Picture to Proton*. Cambridge university press, 2017. [Cited on pages xiii, 7, 9, 19, 23, and 45.]

[22] Zhi-Pei Liang and Paul Lauterbur. *Principles of Magnetic Resonance Imaging - A Signal Processing Perspective*. 2000. [Cited on pages 7, 8, 9, 11, 13, 15, 18, 21, 23, and 31.]

[23] Rui Filipe David Lavrador. *Correction of image distortions in magnetic resonance imaging: intensity inhomogeneities correction and evaluation*. PhD thesis, Universidade de Coimbra (Portugal), 2010. [Cited on pages xiii, 8, and 57.]

[24] Allen D Elster, Arnold M Goldman, and Stanley F Handel. *Magnetic resonance imaging: a reference guide and atlas*. Lippincott Williams & Wilkins, 1986. [Cited on page 11.]

[25] Dominik Weishaupt, Victor Köchli, and Borut Marincek. *How Does MRI Work?: An Introduction to the Physics and Function of Magnetic Resonance Imaging*. 01 2006. [Cited on pages xiii, 11, 12, 15, 16, 17, 18, 19, and 22.]

[26] J. Cohen-Adad. What can we learn from t2* maps of the cortex? *NeuroImage*, 93:189–200, 2014. In-vivo Brodmann Mapping of the Human Brain. [Cited on pages xiii and 12.]

[27] Gustav J Strijkers, Willem J M Mulder, Geralda A F van Tilborg, and Klaas Nicolay. Mri contrast agents: current status and future perspectives. *Anti-Cancer Agents in Medicinal Chemistry (Formerly Current Medicinal Chemistry-Anti-Cancer Agents)*, 7(3):291–305, 2007. [Cited on pages 12 and 13.]

[28] Yu-Dong Xiao, Ramchandra Paudel, Jun Liu, Cong Ma, Zi-Shu Zhang, and Shun-Ke Zhou. Mri contrast agents: Classification and application. *International journal of molecular medicine*, 38(5):1319–1326, 2016. [Cited on page 13.]

[29] Jacob Beutel, Harold L Kundel, Yongmin Kim, Richard L Van Metter, and Steven C Horii. *Handbook of medical imaging*, volume 3. Spie Press, 2000. [Cited on pages 13, 17, 19, and 20.]

[30] Vincent Jacques and Jean François Desreux. New classes of mri contrast agents. *Contrast agents I: magnetic resonance imaging*, pages 123–164, 2002. [Cited on page 13.]

[31] Sofia Caspani, Ricardo Magalhães, Joao Araujo, and Celia Sousa. Magnetic nanomaterials as contrast agents for mri. 04 2020. [Cited on pages 13 and 14.]

[32] RB Clarkson. Blood-pool mri contrast agents: properties and characterization. *Contrast agents I: magnetic resonance imaging*, pages 201–235, 2002. [Cited on pages 13 and 15.]

[33] INFARMED. Boletim de farmacovigilância gd, volume 22, nº2, fevereiro de 2018. 2018. [Cited on page 14.]

[34] Camille Verry, Sandrine Dufort, Benjamin Lemasson, Sylvie Grand, Johan Pietras, Irène Troprès, Yannick Crémillieux, François Lux, Sébastien Mériaux, Benoit Larrat, et al. Targeting brain metastases with ultrasmall theranostic nanoparticles, a first-in-human trial from an mri perspective. *Science Advances*, 6(29):eaay5279, 2020. [Cited on page 14.]

[35] Camille Verry, Sandrine Dufort, Julie Villa, Marylaure Gavard, Carole Iriart, Sylvie Grand, Julie Charles, Benoit Chovelon, Jean-Luc Cracowski, Jean-Louis Quesada, et al. Theranostic aguix nanoparticles as radiosensitizer: A phase i, dose-escalation study in patients with multiple brain metastases (nano-rad trial). *Radiotherapy and Oncology*, 160:159–165, 2021. [Cited on page 14.]

[36] Katie A Davis and Bruce Lazar. Manganese-based contrast agents as a replacement for gadolinium. *Radiologic Technology*, 93(1):36–45, 2021. [Cited on page 14.]

[37] Rouqiao Zheng, Junru Guo, Xinyi Cai, Lianjie Bin, Chengyu Lu, Amita Singh, Manoj Trivedi, Abhinav Kumar, and Jianqiang Liu. Manganese complexes and manganese-based metal-organic frameworks as contrast agents in mri and chemotherapeutics agents: Applications and prospects. *Colloids and Surfaces B: Biointerfaces*, 213:112432, 2022. [Cited on page 14.]

[38] Can Chen, Jianxian Ge, Yun Gao, Lei Chen, Jiabin Cui, Jianfeng Zeng, and Mingyuan Gao. Ultrasmall superparamagnetic iron oxide nanoparticles: A next generation contrast agent for magnetic resonance imaging. *Wiley Interdisciplinary Reviews: Nanomedicine and Nanobiotechnology*, 14(1):e1740, 2022. [Cited on page 14.]

[39] C Preibisch and R Deichmann. T1 mapping using spoiled flash-epi hybrid sequences and varying flip angles. *Magnetic Resonance in Medicine: An Official Journal of the International Society for Magnetic Resonance in Medicine*, 62(1):240–246, 2009. [Cited on page 17.]

[40] Hélène Clique, Hai-Ling Margaret Cheng, Pierre-Yves Marie, Jacques Felblinger, and Marine Beaumont. 3d myocardial t1 mapping at 3t using variable flip angle method: pilot study. *Magnetic resonance in medicine*, 71(2):823–829, 2014. [Cited on page 17.]

[41] Fiona M Fennessy, Andriy Fedorov, Sandeep N Gupta, Ehud J Schmidt, Clare M Tempany, and Robert V Mulkern. Practical considerations in t1 mapping of prostate for dynamic contrast enhancement pharmacokinetic analyses. *Magnetic resonance imaging*, 30(9):1224–1233, 2012. [Cited on page 17.]

[42] RS Samson, O Ciccarelli, C Kachramanoglou, L Brightman, Antoine Lutti, David L Thomas, Nikolaus Weiskopf, and CAM Wheeler-Kingshott. Tissue-and column-specific measurements from multiparameter mapping of the human cervical spinal cord at 3 t. *NMR in Biomedicine*, 26(12):1823–1830, 2013. [Cited on page 17.]

[43] Yong Chen, Yun Jiang, Shivani Pahwa, Dan Ma, Lan Lu, Michael D Twieg, Katherine L Wright, Nicole Seiberlich, Mark A Griswold, and Vikas Gulani. Mr fingerprinting for rapid quantitative abdominal imaging. *Radiology*, 279(1):278–286, 2016. [Cited on page 17.]

[44] Felix W Wehrli. Fast-scan magnetic resonance: principles and applications. *Magnetic resonance quarterly*, 6(3):165–236, 1990. [Cited on page 18.]

[45] Bernd L Schmitz, Andrik J Aschoff, Martin HK Hoffmann, and Georg Grön. Advantages and pitfalls in 3t mr brain imaging: a pictorial review. *American Journal of Neuroradiology*, 26(9):2229–2237, 2005. [Cited on pages 19, 20, and 25.]

[46] David B Siepmann, Jeff McGovern, Jean H Brittain, and Scott B Reeder. High-resolution 3d cartilage imaging with ideal–spgr at 3 t. *American Journal of Roentgenology*, 189(6):1510–1515, 2007. [Cited on page 20.]

[47] Jehan A Mazroa, Sabry A Elmogy, and Mohamed M Elgendy. Value of contrast enhanced spoiled gradient (spgr) mr and mip mr imaging in diagnosis of peri-anal fistula. *The Egyptian Journal of Radiology and Nuclear Medicine*, 43(2):119–128, 2012. [Cited on page 20.]

[48] Kaori Furutani, Masafumi Harada, Mahmut Mawlan, and Hiromu Nishitani. Difference in enhancement between spin echo and 3-dimensional fast spoiled gradient recalled acquisition in steady state magnetic resonance imaging of brain metastasis at 3-t magnetic resonance imaging. *Journal of computer assisted tomography*, 32(2):313–319, 2008. [Cited on page 20.]

[49] Maddy Artunduaga, C Amber Liu, Cara E Morin, Suraj D Serai, Unni Udayasankar, Mary-Louise C Greer, and Michael S Gee. Safety challenges related to the use of sedation and general anesthesia in pediatric patients undergoing magnetic resonance imaging examinations. *Pediatric radiology*, 51:724–735, 2021. [Cited on page 20.]

[50] Rizwan Ahmad, Houchun Harry Hu, Ramkumar Krishnamurthy, and Rajesh Krishnamurthy. Reducing sedation for pediatric body mri using accelerated and abbreviated imaging protocols. *Pediatric radiology*, 48:37–49, 2018. [Cited on page 20.]

[51] Adam C Zelinski, Vivek K Goyal, Elfar Adalsteinsson, and Lawrence L Wald. Sparsity in mri rf excitation pulse design. In *2008 42nd Annual Conference on Information Sciences and Systems*, pages 252–257. IEEE, 2008. [Cited on pages xiii and 21.]

[52] Philip Keller and Metrolab Instruments. Technologies for precision magnetic field mapping. *Geneva: Metrolab Instruments*, 2007. [Cited on page 22.]

[53] Natalia Gudino and Sebastian Littin. Advancements in gradient system performance for clinical and research mri. *Journal of Magnetic Resonance Imaging*, 57(1):57–70, 2023. [Cited on page 22.]

[54] Silvia S Hidalgo-Tobon. Theory of gradient coil design methods for magnetic resonance imaging. *Concepts in Magnetic Resonance Part A*, 36(4):223–242, 2010. [Cited on page 22.]

[55] H Siebold. Gradient field coils for mr imaging with high spectral purity. *IEEE transactions on magnetics*, 26(2):897–900, 1990. [Cited on pages 23 and 44.]

[56] TA Frenkiel, A Jasinski, and PG Morris. Apparatus for generation of magnetic field gradient waveforms for nmr imaging. *Journal of Physics E: Scientific Instruments*, 21(4):374, 1988. [Cited on pages 23 and 44.]

[57] Carri Glide-Hurst, Eric Paulson, Kiaran McGee, Neelam Tyagi, Yanle Hu, James Balter, and John Bayouth. Task group 284 report: Magnetic resonance imaging simulation in radiotherapy: Considerations for clinical implementation, optimization, and quality assurance. *Medical Physics*, 48, 07 2021. [Cited on pages xiii, 24, 26, 44, 50, 60, 61, 64, and 82.]

[58] Michael Lamba, John C Breneman, and Ronald E Warnick. Evaluation of image-guided positioning for frameless intracranial radiosurgery. *International Journal of Radiation Oncology* Biology* Physics*, 74(3):913–919, 2009. [Cited on page 24.]

[59] Steven Babic, Young Lee, Mark Ruschin, Fiona Lochray, Alex Lightstone, Eshetu Atenafu, Nic Phan, Todd Mainprize, May Tsao, Hany Soliman, et al. To frame or not to frame? cone-beam ct-based analysis of head immobilization devices specific to linac-based stereotactic radiosurgery and radiotherapy. *Journal of Applied Clinical Medical Physics*, 19(2):111–120, 2018. [Cited on page 24.]

[60] Aaron Bush, Laura Vallow, Henry Ruiz-Garcia, Steven Herchko, Ronald Reimer, Stephen Ko, Byron May, Daniel M Trifiletti, and Jennifer Peterson. Mask-based immobilization in gamma knife stereotactic radiosurgery. *Journal of Clinical Neuroscience*, 83:37–42, 2021. [Cited on page 24.]

[61] Veit Mengling, Christoph Bert, Rosalind Perrin, Siti Masitho, Thomas Weissmann, Sina Mansoorian, Hadi Siavooshhaghighi, Rolf Janka, Sylvain Doussin, Melanie Habatsch, et al. Implementation of a dedicated 1.5 t mr scanner for radiotherapy treatment planning featuring a novel high-channel coil setup for brain imaging in treatment position. *Strahlentherapie und Onkologie*, 197:246–256, 2021. [Cited on page 24.]

[62] Petrice M Cogswell, Joshua D Trzasko, Erin M Gray, Norbert G Campeau, Phillip J Rossman, Daehun Kang, Fraser Robb, Robert S Stormont, Scott A Lindsay, Matt A Bernstein, et al. Application of adaptive image receive coil technology for whole-brain imaging. *AJR. American journal of roentgenology*, 216(2):552, 2021. [Cited on page 24.]

[63] Cédric Buttin, Nicolas Dechâtre, Mauris Corentin, and Thuret Allan. Revisiting 3t: Pearls and pitfalls compared with 1.5t. 2020. [Cited on pages 24, 25, 27, 47, 48, and 50.]

[64] Francesca Granata, Rosa Morabito, Enricomaria Mormina, Concetta Alafaci, Silvia Marino, Angela Laganà, Sergio Lucio Vinci, Marilena Briguglio, Alessandro Calamuneri, Michele Gaeta, et al. 3t double inversion recovery magnetic resonance imaging: diagnostic advantages in the evaluation of cortical development anomalies. *European Journal of Radiology*, 85(5):906–914, 2016. [Cited on page 25.]

[65] Jennifer Elizabeth Dixon, Ashley Simpson, Niraj Mistry, Nikos Evangelou, and Peter Gordon Morris. Optimisation of t2*-weighted mri for the detection of small veins in multiple sclerosis at 3 t and 7 t. *European Journal of Radiology*, 82(5):719–727, 2013. [Cited on page 25.]

[66] Di Cao, Yuanqi Sun, Yinghao Li, Pan Su, Jay J Pillai, Ye Qiao, Hanzhang Lu, Peter CM Van Zijl, Linda Knutsson, and Jun Hua. Concurrent measurement of perfusion parameters related to small blood vessels and cerebrospinal fluid circulation in the human brain using dynamic dual-spin-echo perfusion mri. *NMR in Biomedicine*, page e4984, 2023. [Cited on page 25.]

[67] TE Sjøbakk, S Lundgren, A Kristoffersen, T Singstad, AJ Svarliaunet, U Sonnewald, and IS Gribbestad. Clinical 1h magnetic resonance spectroscopy of brain metastases at 1.5 t and 3t. *Acta Radiologica*, 47(5):501–508, 2006. [Cited on page 25.]

[68] Brian J Soher, Brian M Dale, and Elmar M Merkle. A review of mr physics: 3t versus 1.5 t. *Magnetic resonance imaging clinics of North America*, 15(3):277–290, 2007. [Cited on pages 25 and 26.]

[69] Giovanna Stefania Colafati, Enrica Rossi, Chiara Carducci, Simone Piga, Ioan Paul Voicu, Angela Mastronuzzi, and Paolo Tomà. Half-dose versus full-dose macrocyclic gadolinium at 3-t magnetic resonance imaging in paediatric bone and soft-tissue disease. *Pediatric Radiology*, 48(12):1724–1735, 2018. [Cited on page 25.]

[70] Xuan V Nguyen, Sana Tahir, Brian W Bresnahan, Jalal B Andre, Elvira V Lang, Mahmud Mossa-Basha, Nina A Mayr, and Eric C Bourekas. Prevalence and financial impact of claustrophobia, anxiety, patient motion, and other patient events in magnetic resonance imaging. *Topics in Magnetic Resonance Imaging*, 29(3):125–130, 2020. [Cited on page 26.]

[71] Edson Amaro Jr, Steve CR Williams, Sukhi S Shergill, Cynthia HY Fu, Mairead MacSweeney, Marco M Picchioni, Michael J Brammer, and Philip K McGuire. Acoustic noise and functional magnetic resonance imaging: current strategies and future prospects. *Journal of Magnetic Resonance Imaging: An Official Journal of the International Society for Magnetic Resonance in Medicine*, 16(5):497–510, 2002. [Cited on page 26.]

[72] Nicolae Bolog, Daniel Nanz, and Dominik Weishaupt. Muskuloskeletal mr imaging at 3.0 t: current status and future perspectives. *European radiology*, 16:1298–1307, 2006. [Cited on page 26.]

[73] B Zhang, Derek Macfadden, Andrei Damyanovich, Marcus Rieker, J Stainsby, M Bernstein, D Jaffray, David Mikulis, and Cynthia Ménard. Development of a geometrically accurate imaging protocol at 3 tesla mri for stereotactic radiosurgery treatment planning. *Physics in medicine and biology*, 55:6601–15, 10 2010. [Cited on pages 27 and 31.]

[74] Florian Putz, Veit Mengling, Rosalind Perrin, Siti Masitho, Thomas Weissmann, Johannes Rösch, Tobias Bäuerle, Rolf Janka, Alexander Cavallaro, Prof Uder, Patrick Amarteifio, Sylvain Doussin, Dr Schmidt, Arndt Dörfler, Sabine Semrau, Sebastian Lettmaier, Rainer Fietkau, and Christoph Bert. Magnetic resonance imaging for brain stereotactic radiotherapy: A review of requirements and pitfalls. *Strahlentherapie und Onkologie*, 03 2020. [Cited on pages 27, 37, 51, and 60.]

[75] Katarzyna Krupa and Monika Bekiesińska-Figatowska. Artifacts in magnetic resonance imaging. *Polish journal of radiology*, 80:93, 2015. [Cited on pages 28, 35, and 44.]

[76] E Bellon, Mark Haacke, P Coleman, D Sacco, DA Steiger, and Raymond Gangarosa. Mr artifacts: A review. *AJR. American journal of roentgenology*, 147:1271–81, 12 1986. [Cited on pages 28 and 31.]

[77] Stanislav Motyka, Paul Weiser, Beata Bachrata, Lukas Hingerl, Bernhard Strasser, Gilbert Hangel, Eva Niess, Dario Goranovic, Fabian Niess, Maxim Zaitsev, et al. Predicting dynamic, motion-related changes in b0 field in the brain at a 7 t mri using a subject-specific fine-tuned u-net. *arXiv preprint arXiv:2304.08307*, 2023. [Cited on pages 28 and 59.]

[78] Emiel Por, Maaike van Kooten, and Vanja Sarkovic. Nyquist–shannon sampling theorem. *Leiden University*, 1(1), 2019. [Cited on page 28.]

[79] Kirin Escher and Frank G Shellock. Evaluation of mri artifacts at 3 tesla for 38 commonly used cosmetics. *Magnetic Resonance Imaging*, 31(5):778–782, 2013. [Cited on page 29.]

[80] Yue Yan, Jinzhong Yang, Sam Beddar, Geoffrey Ibbott, Zhifei Wen, Laurence E Court, Ken-Pin Hwang, Mo Kadbi, Sunil Krishnan, Clifton D Fuller, Steven J Frank, James Yang, Peter Balter, Rajat J Kudchadker, and Jihong Wang. A methodology to investigate the impact of image distortions on the radiation dose when using magnetic resonance images for planning. *Physics in Medicine & Biology*, 63(8):085005, apr 2018. [Cited on page 30.]

[81] Xuechun Liu, Zhenjiang Li, Yi Rong, Minsong Cao, Hongyu Li, Chuntao Jia, Liting Shi, Weizhao Lu, Guanzhong Gong, Yong Yin, and Jianfeng Qiu. A comparison of the distortion in the same field mri and mr-linac system with a 3d printed phantom. *Frontiers in Oncology*, 11, 06 2021. [Cited on pages 30, 58, and 61.]

[82] Hae Yu Kim, Sun-il Lee, Seong Jin Jin, Sung-Chul Jin, Jung Soo Kim, and Kyoung Dong Jeon. Reliability of stereotactic coordinates of 1.5-tesla and 3-tesla mri in radiosurgery and functional neurosurgery. *Journal of Korean Neurosurgical Society*, 55(3):136–141, 2014. [Cited on page 30.]

[83] Eleftherios Pappas, Mukhtar Alshanqity, Argyris Moutsatsos, Hani Lababidi, Khalid Alsafi, Konstantinos Georgiou, Pantelis Karaiskos, and Evangelos Georgiou. Mri-related geometric distortions in stereotactic radiotherapy treatment planning: Evaluation and dosimetric impact. *Technology in Cancer Research & Treatment*, 16:153303461773545, 10 2017. [Cited on page 30.]

[84] Weygand J, CD Fuller, GS Ibbott, AS Mohamed, Y Ding, J Yang, KP Hwang, and J. Wang. Spatial precision in magnetic resonance imaging-guided radiation therapy: The role of geometric distortion. *International Journal of Radiation Oncology Biology Physics*, 95(4):1304–1316, July 2016. [Cited on pages 31 and 54.]

[85] Daisy Wang and David Doddrell. Geometric distortion in structural magnetic resonance imaging. *Current Medical Imaging Reviews*, 1, 01 2005. [Cited on pages 32, 35, 36, 37, 54, 58, and 59.]

[86] Bruno Pinho Meneses, Jason P Stockmann, Nicolas Arango, Paul-François Gapais, Eric Giacomini, Franck Mauconduit, Vincent Gras, Nicolas Boulant, Alexandre Vignaud, Michel Luong, et al. Shim coils tailored for correcting b0 inhomogeneity in the human brain (scotch): Design methodology and 48-channel prototype assessment in 7-tesla mri. *NeuroImage*, 261:119498, 2022. [Cited on page 32.]

[87] Bruno Pinho Meneses and Alexis Amadon. A fieldmap-driven few-channel shim coil design for mri of the human brain. *Physics in Medicine & Biology*, 66(1):015001, 2021. [Cited on page 32.]

[88] Jason P Stockmann and Lawrence L Wald. In vivo b0 field shimming methods for mri at 7 t. *Neuroimage*, 168:71–87, 2018. [Cited on page 32.]

[89] Jorge Jovicich, Silvester Czanner, Douglas Greve, Elizabeth Haley, Andre Kouwe, Randy Gollub, David Kennedy, Franz Schmitt, Gregory Brown, James Macfall, Bruce Fischl, and Anders Dale. Reliability in multi-site structural mri studies: Effects of gradient non-linearity correction on phantom and human data. *NeuroImage*, 30:436–43, 05 2006. [Cited on page 32.]

[90] Umesh Rudrapatna, Greg D Parker, Jamie Roberts, and Derek K Jones. A comparative study of gradient nonlinearity correction strategies for processing diffusion data obtained with ultra-strong gradient mri scanners. *Magnetic Resonance in Medicine*, 85(2):1104–1113, 2021. [Cited on page 32.]

[91] Somayeh Taghizadeh, Cecille Labuda, Claus Yang, Bart Morris, Madhava Kanakamedala, Srinivasan Vijayakumar, Roberto Rey-Dios, William Duggar, Edward Florez, and Ali Fatemi. Optimizing mri sequences and images for mri-based stereotactic radiosurgery treatment planning. *Reports of Practical Oncology and Radiotherapy*, 24:12–19, 09 2018. [Cited on pages 32, 34, 36, 51, 61, and 83.]

[92] Richard Speight, Michael Dubec, Cynthia L Eccles, Ben George, Ann Henry, Trina Herbert, Robert I Johnstone, Gary P Liney, Hazel McCallum, and Maria A Schmidt. Ipem topical report: guidance on the use of mri for external beam radiotherapy treatment planning. *Physics in Medicine & Biology*, 66(5):055025, 2021. [Cited on page 32.]

[93] Mary Adjeiwaah, Mikael Bylund, Josef A Lundman, Karin Söderström, Björn Zackrisson, Joakim H Jonsson, Anders Garpebring, and Tufve Nyholm. Dosimetric impact of mri distortions: a study on head and neck cancers. *International Journal of Radiation Oncology* Biology* Physics*, 103(4):994–1003, 2019. [Cited on page 33.]

[94] Paul Retif, Abdourahamane Djibo Sidikou, Christian Mathis, Romain Letellier, Emilie Verrecchia-Ramos, Rémi Dupres, and Xavier Michel. Evaluation of the ability of the brainlab elements cranial distortion correction algorithm to correct clinically relevant mri distortions for cranial srt. *Strahlentherapie und Onkologie*, 198(10):907–918, 2022. [Cited on page 33.]

[95] John F Schenck. The role of magnetic susceptibility in magnetic resonance imaging: Mri magnetic compatibility of the first and second kinds. *Medical physics*, 23(6):815–850, 1996. [Cited on page 34.]

[96] Clarissa Kroll, Matthias Opel, Chiara Paganelli, Florian Kamp, Sebastian Neppl, Guido Baroni, Olaf Dietrich, Claus Belka, Katia Parodi, and Marco Riboldi. Simulation of tissue dependent magnetic field susceptibility effects in mri guided radiotherapy. *Radiother. Oncol.*, 133:S554–S555, 2019. [Cited on page 34.]

[97] Tianle Cao, Sen Ma, Nan Wang, Sara Gharabaghi, Yibin Xie, Zhaoyang Fan, Elliot Hogg, Chaowei Wu, Fei Han, Michele Tagliati, et al. Three-dimensional simultaneous brain mapping of t1, t2, and magnetic susceptibility with mr multitasking. *Magnetic resonance in medicine*, 87(3):1375–1389, 2022. [Cited on page 34.]

[98] Frank G Shellock. Magnetic resonance: bioeffects, safety, and patient management. *New York: Raven*, 10:101–121, 1994. [Cited on page 35.]

[99] Andre Costa, Simone Appenzeller, Clarissa Yasuda, Fabricio Pereira, Verônica Zanardi, and Fernando Cendes. Artifacts in brain magnetic resonance imaging due to metallic dental objects. *Medicina oral, patología oral y cirugía bucal*, 14:E278–82, 04 2009. [Cited on page 35.]

[100] Stereotactic Radiosurgery SRS. Stereotactic radiosurgery (srs) and stereotactic body radiation therapy (sbrt). [Cited on page 35.]

[101] A Fogliata, R Cayez, R Garcia, C Khamphan, G Reggiori, M Scorsetti, and L Cozzi. Flattening filter free beam from halcyon linac: Evaluation of the profile parameters for quality assurance. *Medical physics*, 47(8):3669–3674, 2020. [Cited on page 35.]

[102] Alemeh Sadrollahi, Frank Nuesken, Norbert Licht, Christian Rübe, and Yvonne Dzierma. Monte-carlo simulation of the siemens artiste linear accelerator flat 6 mv and flattening-filter-free 7 mv beam line. *PLoS One*, 14(1):e0210069, 2019. [Cited on page 35.]

[103] Daphna Y Gelblum, Henry Lee, Mark Bilsky, Carol Pinola, Sally Longford, and Kent Wallner. Radiographic findings and morbidity in patients treated with stereotactic radiosurgery. *International Journal of Radiation Oncology* Biology* Physics*, 42(2):391–395, 1998. [Cited on page 36.]

[104] M. A. Schmidt and G. S. Payne. Radiotherapy planning using mri. *Physics in Medicine and Biology*, 60(22):R323–R361, 2015. [Cited on page 36.]

[105] Ahmad Waleed Salehi, Preety Baglat, Brij Bhushan Sharma, Gaurav Gupta, and Ankita Upadhya. A cnn model: earlier diagnosis and classification of alzheimer disease using mri. In *2020 International Conference on Smart Electronics and Communication (ICOSEC)*, pages 156–161. IEEE, 2020. [Cited on page 36.]

[106] Cristina Granziera, Jens Wuerfel, Frederik Barkhof, Massimiliano Calabrese, Nicola De Stefano, Christian Enzinger, Nikos Evangelou, Massimo Filippi, Jeroen JG Geurts, Daniel S Reich, et al. Quantitative magnetic resonance imaging towards clinical application in multiple sclerosis. *Brain*, 144(5):1296–1311, 2021. [Cited on page 36.]

[107] Kunal Gupta, Brian Cabaniss, Ammar Kheder, Satyanarayana Gedela, Paul Koch, Kelsey C Hewitt, Abdulrahman Alwaki, Christopher Rich, Supriya Ramesha, Ranliang Hu, et al. Stereotactic mri-guided laser interstitial thermal therapy for extratemporal lobe epilepsy. *Epilepsia*, 61(8):1723–1734, 2020. [Cited on page 36.]

[108] Eric Paulson, Sjoerd Crijns, Brian Keller, Jihong Wang, Maria Schmidt, Glyn Coutts, and Uulke Heide. Consensus opinion on mri simulation for external beam radiation treatment planning. *Radiotherapy and Oncology*, 121, 11 2016. [Cited on pages 37, 39, and 59.]

[109] Wagner Malagó Tavares, Francisco Tustumi, Claudia da Costa Leite, Lionel Fernel Gamarra, Edson Amaro Junior, Manoel Jacobsen Texeira, Sabrina Araujo de França, and Erich Talamoni Fonoff. Distortion correction protocol for 3t stereotactic magnetic resonance imaging: A clinical study. *World neurosurgery*, 122:e690–e699, 2019. [Cited on page 37.]

[110] Iiro Ranta, Reko Kemppainen, Jani Keyriläinen, Sami Suilamo, Samuli Heikkinen, Mika Kapanen, and Jani Saunavaara. Quality assurance measurements of geometric accuracy for magnetic resonance imaging-based radiotherapy treatment planning. *Physica Medica*, 62:47–52, 2019. [Cited on page 37.]

[111] Christian P Karger, Angelika Höss, Rolf Bendl, Valer Canda, and Lothar Schad. Accuracy of device-specific 2d and 3d image distortion correction algorithms for magnetic resonance imaging of the head provided by a manufacturer. *Physics in Medicine & Biology*, 51(12):N253, 2006. [Cited on page 37.]

[112] Amy Walker, Gary Liney, Peter Metcalfe, and Lois Holloway. Mri distortion: Considerations for mri based radiotherapy treatment planning. *Australasian physical & engineering sciences in medicine / supported by the Australasian College of Physical Scientists in Medicine and the Australasian Association of Physical Sciences in Medicine*, 37, 02 2014. [Cited on pages 37 and 59.]

[113] NEMA Standards Publication MS 12-2016. Quantification and mapping of geometric distortion for special applications. 2016. [Cited on pages 38, 39, 55, and 56.]

[114] Wolfgang R Nitz and P Reimer. Contrast mechanisms in mr imaging. *European radiology*, 9:1032–1046, 1999. [Cited on page 38.]

[115] Richard R Ernst and Weston A Anderson. Application of fourier transform spectroscopy to magnetic resonance. *Review of Scientific Instruments*, 37(1):93–102, 1966. [Cited on page 39.]

[116] Jinghua Wang, Lili He, Hairong Zheng, and Zhong-Lin Lu. Optimizing the magnetization-prepared rapid gradient-echo (mp-rage) sequence. *PloS one*, 9(5):e96899, 2014. [Cited on page 39.]

[117] John W Snell, Jason Sheehan, Matei Stroila, and Ladislau Steiner. Assessment of imaging studies used with radiosurgery: a volumetric algorithm and an estimation of its error. *Journal of neurosurgery*, 104(1):157–162, 2006. [Cited on page 39.]

[118] Mohammed AQ Al-Saleh, Noura A Alsufyani, Humam Saltaji, Jacob L Jaremko, and Paul W Major. Mri and cbct image registration of temporomandibular joint: a systematic review. *Journal of Otolaryngology-Head & Neck Surgery*, 45(1):1–7, 2016. [Cited on page 39.]

[119] Gary E Christensen and Hans J Johnson. Consistent image registration. *IEEE transactions on medical imaging*, 20(7):568–582, 2001. [Cited on page 40.]

[120] Amir Pasha Mahmoudzadeh and Nasser H Kashou. Evaluation of interpolation effects on upsampling and accuracy of cost functions-based optimized automatic image registration. *Journal of Biomedical Imaging*, 2013:16–16, 2013. [Cited on page 40.]

[121] Medha V Wyawahare, Pradeep M Patil, Hemant K Abhyankar, et al. Image registration techniques: an overview. *International Journal of Signal Processing, Image Processing and Pattern Recognition*, 2(3):11–28, 2009. [Cited on page 40.]

[122] Francisco PM Oliveira and Joao Manuel RS Tavares. Medical image registration: a review. *Computer methods in biomechanics and biomedical engineering*, 17(2):73–93, 2014. [Cited on page 40.]

[123] Koen AJ Eppenhof, Maxime W Lafarge, Pim Moeskops, Mitko Veta, and Josien PW Pluim. Deformable image registration using convolutional neural networks. In *Medical Imaging 2018: Image Processing*, volume 10574, pages 192–197. SPIE, 2018. [Cited on page 41.]

[124] Bob D De Vos, Floris F Berendsen, Max A Viergever, Marius Staring, and Ivana Išgum. End-to-end unsupervised deformable image registration with a convolutional neural network. In *Deep Learning in Medical Image Analysis and Multimodal Learning for Clinical Decision Support: Third International Workshop, DLMIA 2017, and 7th International Workshop, ML-CDS 2017, Held in Conjunction with MICCAI 2017, Québec City, QC, Canada, September 14, Proceedings 3*, pages 204–212. Springer, 2017. [Cited on page 41.]

[125] Lisa M Tartaglino, Adam E Flanders, Simon Vinitski, and David P Friedman. Metallic artifacts on mr images of the postoperative spine: reduction with fast spin-echo techniques. *Radiology*, 190(2):565–569, 1994. [Cited on page 44.]

[126] Claude Pierre-Jerome, Arzu Arslan, and Svein Ivar Bekkelund. Mri of the spine and spinal cord: imaging techniques, normal anatomy, artifacts, and pitfalls. *Journal of manipulative and physiological therapeutics*, 23(7):470–475, 2000. [Cited on page 44.]

[127] Jang Gyu Cha, Hyun Sook Hong, Jai Soung Park, Sang Hyun Paik, and Hae Kyung Lee. Practical application of iterative decomposition of water and fat with echo asymmetry and least-squares estimation (ideal) imaging in minimizing metallic artifacts. *Korean Journal of Radiology*, 13(3):332–341, 2012. [Cited on page 44.]

[128] Martin J Graves and Donald G Mitchell. Body mri artifacts in clinical practice: a physicist's and radiologist's perspective. *Journal of Magnetic Resonance Imaging*, 38(2):269–287, 2013. [Cited on page 44.]

[129] Lauren Shapiro, Monica Harish, Brian Hargreaves, Ernesto Staroswiecki, and Garry Gold. Advances in musculoskeletal mri: technical considerations. *Journal of Magnetic Resonance Imaging*, 36(4):775–787, 2012. [Cited on page 44.]

[130] Maryam Bahaloo, Mohammad Hossein Davari, Mohammad Sobhan, Seyyed Jalil Mirmohammadi, Mohammad Taghi Jalalian, Mohammad Javad Zare Sakhvidi, Farimah Shamsi, Sam Mirfendereski, Abolfazl Mollasadeghi, and Amir Houshang Mehrparvar. Hearing thresholds changes after mri 1.5 t of head and neck. *Radiology research and practice*, 2019, 2019. [Cited on page 44.]

[131] Mark J McJury. Acoustic noise and magnetic resonance imaging: a narrative/descriptive review. *Journal of Magnetic Resonance Imaging*, 55(2):337–346, 2022. [Cited on page 45.]

[132] Marcel Segbers, Carlos V Rizzo Sierra, Hendrikus Duifhuis, and Johannes M Hoogduin. Shaping and timing gradient pulses to reduce mri acoustic noise. *Magnetic resonance in medicine*, 64(2):546–553, 2010. [Cited on page 45.]

[133] Björn Heismann, Martin Ott, and David Grodzki. Sequence-based acoustic noise reduction of clinical mri scans. *Magnetic resonance in medicine*, 73(3):1104–1109, 2015. [Cited on page 45.]

[134] Brent W Rudd, Teik C Lim, Jing-Huei Lee, and Mingfeng Li. Evaluation of mri compatible headphones for active noise control. *Noise Control Engineering Journal*, 61(1):41–49, 2013. [Cited on page 46.]

[135] A Moelker, MW Vogel, M Ouhlous, F Lethimonnier, and PMT Pattyanama. Operator exposure to acoustic noise in interventional mri. In *Proceedings of the 9th Annual Meeting of ISMRM, Glasgow, Scotland*, page 2180, 2001. [Cited on page 46.]

[136] Samantha J Holdsworth, Sarah J Macpherson, Kristen W Yeom, Max Wintermark, and Greg Zaharchuk. Clinical evaluation of silent t1-weighted mri and silent mr angiography of the brain. *American Journal of Roentgenology*, 210(2):404–411, 2018. [Cited on page 46.]

[137] David S Wack and Jon Furuyama. Improved auditory fmri imaging using toshiba scanner with pianissimo. [Cited on page 46.]

[138] A Katsunuma, H Takamori, Y Sakakura, Y Hamamura, Y Ogo, and R Katayama. Quiet mri with novel acoustic noise reduction. *Magnetic Resonance Materials in Physics, Biology and Medicine*, 13:139–144, 2001. [Cited on page 46.]

[139] Robert I Grossman, John M Gomori, Karen N Ramer, Frank J Lexa, and Mitchell D Schnall. Magnetization transfer: theory and clinical applications in neuroradiology. *Radiographics*, 14(2):279–290, 1994. [Cited on page 46.]

[140] Guanshu Liu, Xiaolei Song, Kannie WY Chan, and Michael T McMahon. Nuts and bolts of chemical exchange saturation transfer mri. *NMR in Biomedicine*, 26(7):810–828, 2013. [Cited on page 46.]

[141] Sandesh Gupta, Phalguni Gupta, and Vivek S. Verma. Study on anatomical and functional medical image registration methods. *Neurocomputing*, 452:534–548, 2021. [Cited on page 47.]

[142] Baogui Zhang, Kun Wang, and Tianzi Jiang. Rf power design optimization in mri system. *Magnetic Resonance Letters*, 1(1):89–98, 2021. [Cited on page 47.]

[143] Bob Van Den Bergen, Cornelis AT Van den Berg, Lambertus W Bartels, and Jan JW Lagendijk. 7 t body mri: B1 shimming with simultaneous sar reduction. *Physics in Medicine & Biology*, 52(17):5429, 2007. [Cited on page 47.]

[144] Jamie E Hecker Prost, Felix W Wehrli, Burton Drayer, Jerry Froelich, David Hearshen, and Donald Plewes. Sar reduced pulse sequences. *Magnetic resonance imaging*, 6(2):125–130, 1988. [Cited on page 48.]

[145] Andrew J Wheaton, Arijitt Borthakur, Matthew Corbo, Sridhar R Charagundla, and Ravinder Reddy. Method for reduced sar t1ρ-weighted mri. *Magnetic Resonance in Medicine: An Official Journal of the International Society for Magnetic Resonance in Medicine*, 51(6):1096–1102, 2004. [Cited on page 48.]

[146] Bob van den Bergen, Christiaan C Stolk, Jan Bouwe van den Berg, Jan JW Lagendijk, and Cornelis AT Van den Berg. Ultra fast electromagnetic field computations for rf multi-transmit techniques in high field mri. *Physics in Medicine & Biology*, 54(5):1253, 2009. [Cited on page 48.]

[147] Esra Neufeld, Marie-Christine Gosselin, Manuel Murbach, Andreas Christ, Eugenia Cabot, and Niels Kuster. Analysis of the local worst-case sar exposure caused by an mri multi-transmit body coil in anatomical models of the human body. *Physics in Medicine & Biology*, 56(15):4649, 2011. [Cited on page 48.]

[148] Ajit Shankaranarayanan, Jeffrey L Duerk, and Jonathan S Lewin. Developing a multichannel temperature probe for interventional mri. *Journal of Magnetic Resonance Imaging*, 8(1):197–202, 1998. [Cited on page 48.]

[149] Emiliano Schena, Daniele Tosi, Paola Saccomandi, Elfed Lewis, and Taesung Kim. Fiber optic sensors for temperature monitoring during thermal treatments: An overview. *Sensors*, 16(7):1144, 2016. [Cited on page 48.]

[150] Michael Garwood, Kâmil Uĉurbil, Alan R Rath, M Robin Bendall, Brian D Ross, Steven L Mitchell, and Hellmut Merkle. Magnetic resonance imaging with adiabatic pulses using a single surface coil for rf transmission and signal detection. *Magnetic resonance in medicine*, 9(1):25–34, 1989. [Cited on page 49.]

[151] Shams Rashid, Stanislas Rapacchi, Marmar Vaseghi, Roderick Tung, Kalyanam Shivkumar, J Paul Finn, and Peng Hu. Improved late gadolinium enhancement mr imaging for patients with implanted cardiac devices. *Radiology*, 270(1):269–274, 2014. [Cited on page 49.]

[152] JT Vaughan, G Adriany, CJ Snyder, J Tian, T Thiel, L Bolinger, H Liu, L DelaBarre, and K Ugurbil. Efficient high-frequency body coil for high-field mri. *Magnetic Resonance in Medicine: An Official Journal of the International Society for Magnetic Resonance in Medicine*, 52(4):851–859, 2004. [Cited on page 49.]

[153] Sung-Min Sohn, Lance DelaBarre, John Thomas Vaughan, and Anand Gopinath. Rf multi-channel head coil design with improved b 1+ fields uniformity for high field mri systems. In *2012 IEEE/MTT-S International Microwave Symposium Digest*, pages 1–3. IEEE, 2012. [Cited on page 49.]

[154] Marcello Alecci, Christopher M Collins, Michael B Smith, and Peter Jezzard. Radio frequency magnetic field mapping of a 3 tesla birdcage coil: experimental and theoretical dependence on sample properties. *Magnetic Resonance in Medicine: An Official Journal of the International Society for Magnetic Resonance in Medicine*, 46(2):379–385, 2001. [Cited on page 49.]

[155] Joseph P Hornak, Jerzy Szumowski, and Robert G Bryant. Magnetic field mapping. *Magnetic resonance in medicine*, 6(2):158–163, 1988. [Cited on page 49.]

[156] Ioannis Panagiotelis and Mathias Blasche. Trueform technology. *Magnetom Flash*, 40:114–119, 2009. [Cited on page 49.]

[157] Che A Azlan, Pierluigi Di Giovanni, Trevor S Ahearn, Scott IK Semple, Fiona J Gilbert, and Thomas W Redpath. B1 transmission-field inhomogeneity and enhancement ratio errors in dynamic contrast-enhanced mri (dce-mri) of the breast at 3t. *Journal of Magnetic Resonance Imaging*, 31(1):234–239, 2010. [Cited on page 50.]

[158] Jeffrey H. Simpson. Chapter 2 - instrumental considerations. In Jeffrey H. Simpson, editor, *Organic Structure Determination Using 2-D NMR Spectroscopy (Second Edition)*, pages 21–57. Academic Press, Boston, second edition edition, 2012. [Cited on page 50.]

[159] Christoph Juchem and Robin A de Graaf. B0 magnetic field homogeneity and shimming for in vivo magnetic resonance spectroscopy. *Analytical biochemistry*, 529:17–29, 2017. [Cited on page 50.]

[160] Klaas P Pruessmann, Markus Weiger, Markus B Scheidegger, and Peter Boesiger. Sense: sensitivity encoding for fast mri. *Magnetic Resonance in Medicine: An Official Journal of the International Society for Magnetic Resonance in Medicine*, 42(5):952–962, 1999. [Cited on page 50.]

[161] L Danieli, GC Riccitelli, D Distefano, E Prodi, E Ventura, A Cianfoni, A Kaelin-Lang, M Reinert, and E Pravatà. Brain tumor-enhancement visualization and morphometric assessment: a comparison of mprage, space, and vibe mri techniques. *American Journal of Neuroradiology*, 40(7):1140–1148, 2019. [Cited on page 51.]

[162] Benjamin M Ellingson, Martin Bendszus, Jerrold Boxerman, Daniel Barboriak, Bradley J Erickson, Marion Smits, Sarah J Nelson, Elizabeth Gerstner, Brian Alexander, Gregory Goldmacher, et al. Consensus

recommendations for a standardized brain tumor imaging protocol in clinical trials. *Neuro-oncology*, 17(9):1188–1198, 2015. [Cited on page 51.]

[163] Tomohiro Komada, Shinji Naganawa, Hiroshi Ogawa, Masaya Matsushima, Seiji Kubota, Hisashi Kawai, Hiroshi Fukatsu, Mitsuru Ikeda, Minako Kawamura, Yasuo Sakurai, et al. Contrast-enhanced mr imaging of metastatic brain tumor at 3 tesla: utility of t1-weighted space compared with 2d spin echo and 3d gradient echo sequence. *Magnetic Resonance in Medical Sciences*, 7(1):13–21, 2008. [Cited on page 51.]

[164] Phylliss M Chappell, Norbert J Pelc, TK Foo, Gary H Glover, S Patricia Haros, and Dieter R Enzmann. Comparison of lesion enhancement on spin-echo and gradient-echo images. *American journal of neuroradiology*, 15(1):37–44, 1994. [Cited on page 51.]

[165] Guang Li, Huchen Xie, Holly Ning, Deborah Citrin, Aradhana Kaushal, Kevin Camphausen, and Robert W Miller. Correction of motion-induced misalignment in co-registered pet/ct and mri (t1/t2/flair) head images for stereotactic radiosurgery. *Journal of Applied Clinical Medical Physics*, 12(1):58–67, 2011. [Cited on page 51.]

[166] Zhiqiang Li, Shiv P Srivastava, and John P Karis. A spiral fluid-attenuated inversion recovery magnetic resonance imaging technique for stereotactic radiosurgery treatment planning for trigeminal neuralgia. *Medical Physics*, 48(11):6881–6888, 2021. [Cited on page 51.]

[167] BJ Daou, G Palmateer, DA Wilkinson, BG Thompson, CO Maher, N Chaudhary, JJ Gemmete, JA Hayman, K Lam, DR Wahl, et al. Radiation-induced imaging changes and cerebral edema following stereotactic radiosurgery for brain avms. *American Journal of Neuroradiology*, 42(1):82–87, 2021. [Cited on page 51.]

[168] R Ashikaga, Y Araki, and O Ishida. Mri of head injury using flair. *Neuroradiology*, 39:239–242, 1997. [Cited on page 51.]

[169] Joseph V Hajnal, David J Bryant, Larry Kasuboski, Pradip M Pattany, Beatrice De Coene, Paul D Lewis, Jacqueline M Pennock, Angela Oatridge, Ian R Young, and Graeme M Bydder. Use of fluid attenuated inversion recovery (flair) pulse sequences in mri of the brain. *Journal of computer assisted tomography*, 16(6):841–844, 1992. [Cited on page 51.]

[170] K Miyata, M Hasegawa, Y Abe, T Tabuchi, T Namiki, and T Ishigami. Radiofrequency heating and magnetically induced displacement of dental magnetic attachments during 3.0 t mri. *Dentomaxillofacial Radiology*, 41(8):668–674, 2012. [Cited on page 52.]

[171] Akihiro Takemura, Kouhei Sasamoto, Kaori Nakamura, Tatsunori Kuroda, Saori Shoji, Yukihiro Matsuura, and Tatsuhiko Matsushita. Comparison of image distortion between three magnetic resonance imaging systems of different magnetic field strengths for use in stereotactic irradiation of brain. *Nihon Hoshasen Gijutsu Gakkai Zasshi*, 69(6):641–647, 2013. [Cited on page 53.]

[172] Agah Karakuzu, Labonny Biswas, Julien Cohen-Adad, and Nikola Stikov. Vendor-neutral sequences and fully transparent workflows improve inter-vendor reproducibility of quantitative mri. *Magnetic Resonance in Medicine*, 88(3):1212–1228, 2022. [Cited on page 54.]

[173] Franklin Feingold, Ali R Khan, Alberto Lazari, Chris Markiewicz, Martijn Mulder, Christophe Phillips, Taylor Salo, Nikola Stikov, Kirstie Whitaker, and Gilles de Hollander13. qmri-bids: an extension to the brain imaging data structure for quantitative magnetic resonance imaging data. [Cited on page 54.]

[174] Maysam Jafar, Yassir M Jafar, Christopher Dean, and Marc E Miquel. Assessment of geometric distortion in six clinical scanners using a 3d-printed grid phantom. *Journal of Imaging*, 3(3):28, 2017. [Cited on page 54.]

[175] Caroline Le Ster, Andrea Grant, Pierre-François Van de Moortele, Alejandro Monreal-Madrigal, Gregor Adriany, Alexandre Vignaud, Franck Mauconduit, Cécile Rabrait-Lerman, Benedikt A Poser, Kâmil Uğurbil, et al. Magnetic field strength dependent snr gain at the center of a spherical phantom and up to 11. 7t. *Magnetic resonance in medicine*, 88(5):2131–2138, 2022. [Cited on page 54.]

[176] J Semkova, R Koleva, N Bankov, V Benghin, I Chernykh, V Shurshakov, V Petrov, et al. Radiation characteristics in the spherical tissue-equivalent phantom on the iss during solar activity minimum according to the data from liulin-5 experiment. *Journal of Atmospheric and Solar-Terrestrial Physics*, 99:157–163, 2013. [Cited on page 55.]

[177] I Jadrníčková, K Brabcová, Z Mrázová, F Spurnỳ, VA Shurshakov, IS Kartsev, and RV Tolochek. Dose characteristics and let spectra on and inside the spherical phantom onboard of iss. *Radiation measurements*, 45(10):1536–1540, 2010. [Cited on page 55.]

[178] James F Winslow, Daniel E Hyer, Ryan F Fisher, Christopher J Tien, and David E Hintenlang. Construction of anthropomorphic phantoms for use in dosimetry studies. *Journal of Applied Clinical Medical Physics*, 10(3):195–204, 2009. [Cited on page 55.]

[179] Noelle Crasto, Abirami Kirubarajan, and Dafna Sussman. Anthropomorphic brain phantoms for use in mri systems: a systematic review. *Magnetic Resonance Materials in Physics, Biology and Medicine*, 35(2):277–289, 2022. [Cited on page 55.]

[180] Marco Lai, Simon Skyrman, Flip Kor, Robert Homan, Victor Gabriel El-Hajj, Drazenko Babic, Erik Edström, Adrian Elmi-Terander, Benno HW Hendriks, and Peter HN de With. Development of a ct-compatible, anthropomorphic skull and brain phantom for neurosurgical planning, training, and simulation. *Bioengineering*, 9(10):537, 2022. [Cited on page 55.]

[181] Kristina Bliznakova. The advent of anthropomorphic three-dimensional breast phantoms for x-ray imaging. *Physica Medica*, 79:145–161, 2020. [Cited on page 55.]

[182] Melanie Freed, Jacco A de Zwart, Jennifer T Loud, Riham H El Khouli, Kyle J Myers, Mark H Greene, Jeff H Duyn, and Aldo Badano. An anthropomorphic phantom for quantitative evaluation of breast mri. *Medical physics*, 38(2):743–753, 2011. [Cited on page 55.]

[183] Stephen J Glick and Lynda C Ikejimba. Advances in digital and physical anthropomorphic breast phantoms for x-ray imaging. *Medical physics*, 45(10):e870–e885, 2018. [Cited on page 55.]

[184] NEMA Standards Publication MS 2-2008 (R2014). Determination of two-dimensional geometric distortion in diagnostic magnetic resonance images. 2008. [Cited on page 55.]

[185] Ville Isokoski. *Methods for evaluating geometric distortion in magnetic resonance imaging*. PhD thesis, University of Oulu, 2021. [Cited on page 55.]

[186] Seyed Bagherimofidi, Claus Yang, Roberto Rey-Dios, Madhava Kanakamedala, and Ali Fatemi. Evaluating the accuracy of geometrical distortion correction of magnetic resonance images for use in intracranial brain tumor radiotherapy. *Reports of practical oncology and radiotherapy : journal of Greatpoland Cancer Center in Poznan and Polish Society of Radiation Oncology*, 24:606–613, 11 2019. [Cited on pages 56 and 59.]

[187] Eshwar Pawar. A review article on acrylic pmma. *IOSR J. Mech. Civ. Eng*, 13(2):1–4, 2016. [Cited on page 56.]

[188] Pablo Irarrazabal, Craig H Meyer, Dwight G Nishimura, and Albert Macovski. Inhomogeneity correction using an estimated linear field map. *Magnetic resonance in medicine*, 35(2):278–282, 1996. [Cited on pages 57 and 59.]

[189] Deming Wang, Wendy Strugnell, Gary Cowin, David M Doddrell, and Richard Slaughter. Geometric distortion in clinical mri systems: Part i: evaluation using a 3d phantom. *Magnetic resonance imaging*, 22(9):1211–1221, 2004. [Cited on page 59.]

[190] Lesley N Baldwin, Keith Wachowicz, and B Gino Fallone. A two-step scheme for distortion rectification of magnetic resonance images. *Medical physics*, 36(9Part1):3917–3926, 2009. [Cited on page 59.]

[191] ES Paulson, RW Prost, and XA Li. Tu-e-brc-05:"step and shoot mri:" a simple acquisition method to reduce gradient nonlinearity-induced geometric distortions for radiation treatment planning. *Medical Physics*, 38(6Part29):3770–3770, 2011. [Cited on page 59.]

[192] Amy Walker, Gary Liney, Lois Holloway, Jason Dowling, David Rivest-Henault, and Peter Metcalfe. Continuous table acquisition mri for radiotherapy treatment planning: distortion assessment with a new extended 3d volumetric phantom. *Medical physics*, 42(4):1982–1991, 2015. [Cited on page 59.]

[193] Mao Li, Shanshan Shan, Shekhar S Chandra, Feng Liu, and Stuart Crozier. Fast geometric distortion correction using a deep neural network: Implementation for the 1 tesla mri-linac system. *Medical Physics*, 47(9):4303–4315, 2020. [Cited on page 59.]

[194] Tarraf Torfeh, Rabih Hammoud, Maeve McGarry, Noora Al-Hammadi, and Gregory Perkins. Development and validation of a novel large field of view phantom and a software module for the quality assurance of geometric distortion in magnetic resonance imaging. *Magnetic resonance imaging*, 33(7):939–949, 2015. [Cited on page 59.]

[195] Johannes CA Dimopoulos, Gerdi Schard, Daniel Berger, Stefan Lang, Gregor Goldner, Thomas Helbich, and Richard Pötter. Systematic evaluation of mri findings in different stages of treatment of cervical cancer: potential of mri on delineation of target, pathoanatomic structures, and organs at risk. *International Journal of Radiation Oncology* Biology* Physics*, 64(5):1380–1388, 2006. [Cited on page 60.]

[196] Thomas Benner, André JW van der Kouwe, John E Kirsch, and A Gregory Sorensen. Real-time rf pulse adjustment for b0 drift correction. *Magnetic Resonance in Medicine: An Official Journal of the International Society for Magnetic Resonance in Medicine*, 56(1):204–209, 2006. [Cited on page 60.]

[197] Yu Gao, Fei Han, Ziwu Zhou, Minsong Cao, Tania Kaprealian, Mitchell Kamrava, Chenyang Wang, John Neylon, Daniel A Low, Yingli Yang, et al. Distortion-free diffusion mri using an mri-guided tri-cobalt 60 radiotherapy system: sequence verification and preliminary clinical experience. *Medical physics*, 44(10):5357–5366, 2017. [Cited on page 61.]

[198] Pantelis Karaiskos, Argyris Moutsatsos, Eleftherios Pappas, Evangelos Georgiou, Arkadios Roussakis, Michael Torrens, and Ioannis Seimenis. A simple and efficient methodology to improve geometric accuracy in gamma knife radiation surgery: implementation in multiple brain metastases. *International Journal of Radiation Oncology* Biology* Physics*, 90(5):1234–1241, 2014. [Cited on page 61.]

[199] Lothar R Schad, Stefan Blüml, Hans Hawighorst, Frederik Wenz, and Walter J Lorenz. Radiosurgical treatment planning of brain metastases based on a fast, three-dimensional mr imaging technique. *Magnetic resonance imaging*, 12(5):811–819, 1994. [Cited on page 61.]

[200] Sophie Laurent, Luce Vander Elst, and Robert N Muller. Comparative study of the physicochemical properties of six clinical low molecular weight gadolinium contrast agents. *Contrast media & molecular imaging*, 1(3):128–137, 2006. [Cited on page 63.]

[201] Matthijs Oudkerk, Paul E Sijens, EDWIN JR VAN BEEK, and Theodorus JA Kuijpers. Safety and efficacy of dotarem (gd-dota) versus magnevist (gd-dtpa) in magnetic resonance imaging of the central nervous system. *Investigative radiology*, 30(2):75–78, 1995. [Cited on page 63.]

[202] Sandra Weber, Karola Schrag, Gerd Mildau, Thomas Kuballa, Stephan G Walch, and Dirk W Lachenmeier. Analytical methods for the determination of mineral oil saturated hydrocarbons (mosh) and mineral oil aromatic hydrocarbons (moah)—a short review. *Analytical chemistry insights*, 13:1177390118777757, 2018. [Cited on page 63.]

[203] M Bettiol, D Aragno, and A Bencivenghi. Rm phantom preparation with cuso4 and nicl2 water solutions. In *Congresso Nazionale AIFM*, 2013. [Cited on page 64.]

[204] Kathryn E Keenan, Maureen Ainslie, Alex J Barker, Michael A Boss, Kim M Cecil, Cecil Charles, Thomas L Chenevert, Larry Clarke, Jeffrey L Evelhoch, Paul Finn, et al. Quantitative magnetic resonance imaging phantoms: a review and the need for a system phantom. *Magnetic resonance in medicine*, 79(1):48–61, 2018. [Cited on page 64.]

[205] Kalaivani Thangavel and EMİNE ÜLKÜ SARITAŞ. Aqueous paramagnetic solutions for mri phantoms at 3 t: A detailed study on relaxivities. *Turkish Journal of Electrical Engineering and Computer Sciences*, 25(3):2108–2121, 2017. [Cited on page 64.]

[206] S Keevil. Safety in magnetic resonance imaging. *Med Phys*, 4(1), 2016. [Cited on page 64.]

[207] Michael J Bronskill, Paul L Carson, Steve Einstein, Michael Koshine, Margit Lassen, William Pavlicek Seong Ki Mun, Ronald R Price, and Ann Wrightn. Site planning for magnetic resonance imaging systems. *AAPM report*, (20), 1986. [Cited on page 64.]

[208] Jeffrey H Kleck, James B Smathers, F Eugene Holly, and Lee T Myers. Anthropomorphic radiation therapy phantoms: a quantitative assessment of tissue substitutes. *Medical physics*, 17(5):800–806, 1990. [Cited on page 64.]

[209] Larry A DeWerd and Michael Kissick. *The phantoms of medical and health physics*. Springer, 2014. [Cited on page 64.]

[210] S. Silva, S. Pinto, P. Conde, J. Lencart, E. Machado, and J.A.M. Santos. Optimization of the 3t mri acquisition for radiosurgery patients using a customized head phantom. In *FÍSICA 2022 – 23ª Conferência Nacional de Física e 32º Encontro Ibérico para o Ensino da Física*, 2022. [Cited on pages 64 and 80.]

[211] Hyun Jin Kim, Hye Young Choi, Sun Wha Lee, and Ji Young Hwang. Gadolinium as a ct contrast agent: an experimental study for the effects of injection parameters in the rabbit brain model. *Journal of the Korean Radiological Society*, 52(1):61–67, 2005. [Cited on page 67.]

[212] Tiago Ferreira and Wayne Rasband. Imagej user guide. *ImageJ/Fiji*, 1:155–161, 2012. [Cited on page 67.]

[213] Albert Hirtl, Helmar Bergmann, Barbara Knäusl, Thomas Beyer, Michael Figl, and Johann Hummel. fully-automated analysis of jaszczak phantom measurements as part of routine spect quality control. *Medical Physics*, 44(5):1638–1645, 2017. [Cited on page 69.]

[214] Ronald J Jaszczak, R Edward Coleman, and Chun Bin Lim. Spect: Single photon emission computed tomography. *IEEE Transactions on Nuclear Science*, 27(3):1137–1153, 1980. [Cited on page 69.]

[215] MODUS. Measuring geometric distortion with sub-millimeter accuracy in mrgrt qa. 2021. [Cited on page 70.]

[216] Gerald Kutcher, Lawrence Coia, Michael Gillin, William Hanson, Steven Leibel, Robert Morton, Jatinder Palta, James Purdy, Lawrence Reinstein, and Goran Svensson. Comprehensive QA for radiation oncology: Report of AAPM task group 40. *Medical physics*, 21:581–618, 05 1994. [Cited on page 71.]

[217] The Phantom Laboratory. Magphan® rt phantom product guide. 2022. [Cited on page 71.]

[218] Paul A Yushkevich, Yang Gao, and Guido Gerig. Itk-snap: An interactive tool for semi-automatic segmentation of multi-modality biomedical images. In *2016 38th annual international conference of the IEEE engineering in medicine and biology society (EMBC)*, pages 3342–3345. IEEE, 2016. [Cited on page 73.]

[219] Steve Pieper, Michael Halle, and Ron Kikinis. 3d slicer. In *2004 2nd IEEE international symposium on biomedical imaging: nano to macro (IEEE Cat No. 04EX821)*, pages 632–635. IEEE, 2004. [Cited on page 73.]

[220] Roger Bourne and Roger Bourne. Imagej. *Fundamentals of digital imaging in medicine*, pages 185–188, 2010. [Cited on page 73.]

[221] Xiangyang Xu, Shengzhou Xu, Lianghai Jin, and Enmin Song. Characteristic analysis of otsu threshold and its applications. *Pattern recognition letters*, 32(7):956–961, 2011. [Cited on page 74.]

[222] Denis Le Bihan, Cyril Poupon, Alexis Amadon, and Franck Lethimonnier. Artifacts and pitfalls in diffusion mri. *Journal of Magnetic Resonance Imaging: An Official Journal of the International Society for Magnetic Resonance in Medicine*, 24(3):478–488, 2006. [Cited on page 80.]

[223] Karl V Embleton, Hamied A Haroon, David M Morris, Matthew A Lambon Ralph, and Geoff JM Parker. Distortion correction for diffusion-weighted mri tractography and fmri in the temporal lobes. *Human brain mapping*, 31(10):1570–1587, 2010. [Cited on page 83.]

[224] M Kennis, SJH Van Rooij, RS Kahn, E Geuze, and A Leemans. Choosing the polarity of the phase-encoding direction in diffusion mri: Does it matter for group analysis? *NeuroImage: Clinical*, 11:539–547, 2016. [Cited on page 83.]

[225] M Okan Irfanoglu, Joelle Sarlls, Amritha Nayak, and Carlo Pierpaoli. Evaluating corrections for eddy-currents and other epi distortions in diffusion mri: methodology and a dataset for benchmarking. *Magnetic resonance in medicine*, 81(4):2774–2787, 2019. [Cited on page 83.]

[226] American College of Radiology. Large and medium phantom test guidance for the american college of radiology mri accreditation program. 2022. [Cited on page 83.]

[227] Olaf Dietrich, José G Raya, Scott B Reeder, Maximilian F Reiser, and Stefan O Schoenberg. Measurement of signal-to-noise ratios in mr images: influence of multichannel coils, parallel imaging, and reconstruction filters. *Journal of Magnetic Resonance Imaging: An Official Journal of the International Society for Magnetic Resonance in Medicine*, 26(2):375–385, 2007. [Cited on page 83.]

[228] Jonmenjoy Biswas, C Brett Nelson, Val M Runge, Bernd J Wintersperger, Shannon S Baumann, Carney B Jackson, and Tushar Patel. Brain tumor enhancement in magnetic resonance imaging: comparison of signal-to-noise ratio (snr) and contrast-to-noise ratio (cnr) at 1.5 versus 3 tesla. *Investigative radiology*, 40(12):792–797, 2005. [Cited on page 84.]

[229] K Wachowicz, N De Zanche, E Yip, V Volotovskyy, and BG Fallone. Cnr considerations for rapid real-time mri tumor tracking in radiotherapy hybrid devices: Effects of b0 field strength. *Medical Physics*, 43(8Part1):4903–4914, 2016. [Cited on page 84.]

[230] Hou Jiang, Ning Lu, and Ling Yao. A high-fidelity haze removal method based on hot for visible remote sensing images. *Remote Sensing*, 8(10):844, 2016. [Cited on page 84.]

[231] Youngseob Seo and Zhiyue J Wang. Measurement and evaluation of specific absorption rate and temperature elevation caused by an artificial hip joint during mri scanning. *Scientific reports*, 11(1):1134, 2021. [Cited on page 85.]

[232] Hongrui Guo, Hengmin Cui, Jing Fang, Zhicai Zuo, Junliang Deng, Xun Wang, Ling Zhao, Kejie Chen, and Jie Deng. Nickel chloride (nicl2) in hepatic toxicity: apoptosis, g2/m cell cycle arrest and inflammatory response. *Aging (Albany NY)*, 8(11):3009, 2016. [Cited on page 88.]

[233] Domenico Trombetta, Maria Rita Mondello, Francesco Cimino, Mariateresa Cristani, Simona Pergolizzi, and Antonella Saija. Toxic effect of nickel in an in vitro model of human oral epithelium. *Toxicology letters*, 159(3):219–225, 2005. [Cited on page 88.]

[234] FDA. Dotarem® (gadoterate meglumine) injection for intravenous use. 2013. [Cited on page 89.]

[235] European Committee Executive Agency for Competitiveness and Innovation. Anexo i - lista de medicamentos autorizados a nível nacional. 2019. [Cited on page 89.]

[236] AEJM Cavelaars, Anton E Kunst, JJM Geurts, Roberta Crialesi, L Grötvedt, Uwe Helmert, Eero Lahelma, Olle Lundberg, Andreas Mielck, N Kr Rasmussen, et al. Persistent variations in average height between countries and between socio-economic groups: an overview of 10 european countries. *Annals of human biology*, 27(4):407–421, 2000. [Cited on page 89.]

[237] Boyd A Swinburn, Vivica I Kraak, Steven Allender, Vincent J Atkins, Phillip I Baker, Jessica R Bogard, Hannah Brinsden, Alejandro Calvillo, Olivier De Schutter, Raji Devarajan, et al. The global syndemic of obesity, undernutrition, and climate change: the lancet commission report. *The lancet*, 393(10173):791–846, 2019. [Cited on page 89.]

[238] Sinead Donnelly, Declan Walsh, and Lisa Rybicki. The symptoms of advanced cancer: identification of clinical and research priorities by assessment of prevalence and severity. *Journal of palliative care*, 11(1):27–32, 1995. [Cited on page 89.]

[239] Ragav Sharma and Sandeep Sharma. Physiology, blood volume. 2018. [Cited on page 89.]

[240] Mark A Horsfield, John S Thornton, Andrew Gill, H Rolf Jager, Andrew N Priest, and Bruno Morgan. A functional form for injected mri gd-chelate contrast agent concentration incorporating recirculation, extravasation and excretion. *Physics in Medicine & Biology*, 54(9):2933, 2009. [Cited on page 89.]

[241] Yingmin Li, Feifei Qi, and Yi Wan. Improvements on bicubic image interpolation. In *2019 IEEE 4th Advanced Information Technology, Electronic and Automation Control Conference (IAEAC)*, volume 1, pages 1316–1320. IEEE, 2019. [Cited on page 93.]

[242] Dianyuan Han. Comparison of commonly used image interpolation methods. In *Conference of the 2nd International Conference on Computer Science and Electronics Engineering (ICCSEE 2013)*, pages 1556–1559. Atlantis Press, 2013. [Cited on page 93.]

[243] Kurt G Schilling, Justin Blaber, Colin Hansen, Leon Cai, Baxter Rogers, Adam W Anderson, Seth Smith, Praitayini Kanakaraj, Tonia Rex, Susan M Resnick, et al. Distortion correction of diffusion weighted mri without reverse phase-encoding scans or field-maps. *PLoS One*, 15(7):e0236418, 2020. [Cited on page 101.]

[244] Brian Hargreaves, Pauline W Worters, Kim Butts Pauly, John M Pauly, Kevin M Koch, and Garry E Gold. Metal induced artifacts in mri. *AJR. American journal of roentgenology*, 197(3):547, 2011. [Cited on page 101.]

[245] Martin Bland. *An introduction to medical statistics*. Oxford university press, 2015. [Cited on page 102.]